AD-A032 730 ALASKA UNIV COLLEGE GEOPHYSICAL INST F/G 4/1
A CORRELATION OF DISCRETE AND DIFFUSE AURORA WITH PARTICLE PREC--ETC(U)
AUG 75 R S CAVERLY, G J ROMICK F19628-74-C-0188
UNCLASSIFIED SCIENTIFIC-4 AFCRL-TR-75-0508 NL

1 OF 2
ADA032730

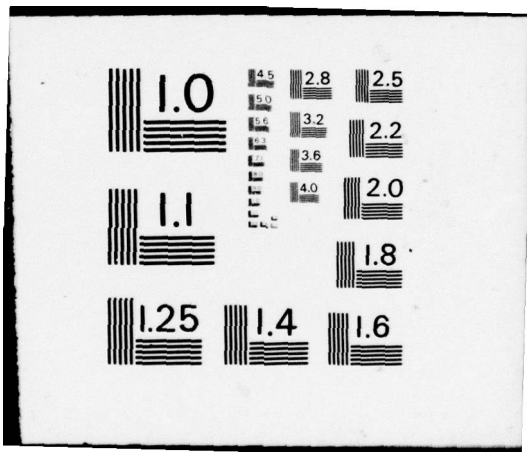
1.0
1.1
1.25
1.4
1.6
1.8
2.0
2.2
2.5
2.8
3.2
3.6
4.0
4.5
5.0
5.6

AD A032730

AFCRL-TR-75-0508

A CORRELATION OF DISCRETE AND DIFFUSE AURORA WITH PARTICLE PRECIPITATION

Richard S. Caverly
and
Gerald J. Romick
Richard D. Sharp*

Geophysical Institute
University of Alaska
Fairbanks, Alaska 99701
*Lockheed Palo Alto Research Laboratory
Palo Alto, California 94340

DDC
RECEIVED
DEC 2 1976
A

August 1975

Scientific Report No. 4

HAES Report No. 35

Approved for public release; distribution unlimited.

This research was sponsored by the Defense Nuclear Agency under Subtask L25AAXYX966, Work Unit 16, entitled "Analysis and Feasibility Assessment", and Subtask .

AIR FORCE CAMBRIDGE RESEARCH LABORATORIES
AIR FORCE SYSTEMS COMMMAND
UNITED STATES AIR FORCE
HANSCOM AFB, MASSACHUSETTS 01731

74-18
AD 781 184

Qualified requestors may obtain additional copies from the Defense Documentation Center. All others should apply to the National Technical Information Service.

UNCLASSIFIED
SECURITY CLASSIFICATION OF THIS PAGE (When Data Entered)

(19) REPORT DOCUMENTATION PAGE	READ INSTRUCTIONS BEFORE COMPLETING FORM
1. REPORT NUMBER: AFCRL-TR-75-0508, HAES-35 — 2. GOVT ACCESSION NO. (18) AFCRL, DNA	3. RECIPIENT'S CATALOG NUMBER
(6) 4. TITLE (and Subtitle): A CORRELATION OF DISCRETE AND DIFFUSE AURORA WITH PARTICLE PRECIPITATION.	5. TYPE OF REPORT & PERIOD COVERED: (9) Scientific Interim rept.
	6. PERFORMING ORG. REPORT NUMBER: (14) Scientific [redacted] 4,
(10) 7. AUTHOR(s): Richard S. Caverly, Gerald J. Romick	8. CONTRACT OR GRANT NUMBER(s): HAES Report No. 35, (15) F19628-74-C-0188, NSF-GA-31876X
9. PERFORMING ORGANIZATION NAME AND ADDRESS: Geophysical Institute, University of Alaska, Fairbanks, Alaska 99701 (12) 124 p.	10. PROGRAM ELEMENT, PROJECT, TASK AREA & WORK UNIT NUMBERS: CDNA-00-18
11. CONTROLLING OFFICE NAME AND ADDRESS: Air Force Cambridge Research Laboratories, Hanscom AFB, Massachusetts 01731, Contract Monitor: Richard M. Nadile/OPR	(11) 12. REPORT DATE: August 1975; 13. NUMBER OF PAGES: 125
14. MONITORING AGENCY NAME & ADDRESS (if different from Controlling Office)	15. SECURITY CLASS. (of this report): UNCLASSIFIED; 15a. DECLASSIFICATION/DOWNGRADING SCHEDULE

16. DISTRIBUTION STATEMENT (of this Report)

Approved for public release; distribution unlimited.

17. DISTRIBUTION STATEMENT (of the abstract entered in Block 20, if different from Report)

18. SUPPLEMENTARY NOTES

This research was sponsored by the Defense Nuclear Agency under Subtask L25AAXYX966, Work Unit 16, entitled "Analysis and Feasibility Assessment."

19. KEY WORDS (Continue on reverse side if necessary and identify by block number)

Alaskan All-Sky Camera Chain,
Magnetic and auroral observations,
Particle detectors, Auroral forms, and
particle precipitation.

20. ABSTRACT (Continue on reverse side if necessary and identify by block number)

Five polar orbiting satellite passes crossing the late evening auroral zone in the spring of 1972 were selected for correlation with all-sky camera data obtained from Alaskan All-sky camera chain of stations. Latitudinal profiles of the 0.6 to 40 kev electron total number flux, total energy flux and average energy are presented together with electron energy spectral displays which afford a →

next page

DD FORM 1 JAN 73 1473 EDITION OF 1 NOV 65 IS OBSOLETE

UNCLASSIFIED
SECURITY CLASSIFICATION OF THIS PAGE (When Data Entered)

152 650

cont →

detailed spectral analysis across the entire latitudinal extent of the electron precipitation region. The electron total number and energy flux profiles are morphologically interpreted as composed of background precipitation on which sit prominent peaks caused by one of three basic spectral changes in the otherwise Maxwellian or expontial-like background spectra. The prominent peaks and a large portion of the background precipitation correlate well with discrete auroral forms and broad regions of visible diffuse aurora respectively. A total particle energy flux threshold of 1 erg/cm^2 sec is established for the production of auroral luminosity just visible to the 35mm all-sky cameras used along the Alaskan all-sky camera chain.

sq cm ↑

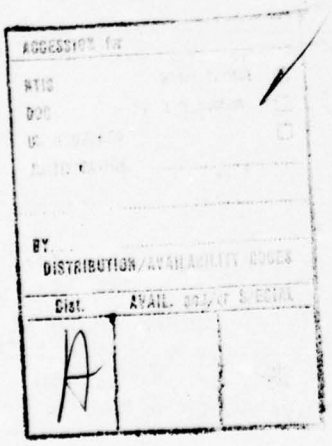

Summary

Five Lockheed instrumented polar orbiting satellite passes which crossed the late evening auroral zone in the spring of 1972 were selected for correlation with all-sky camera data obtained from Alaskan all-sky camera chain of stations. Latitudinal profiles of the 0.6 to 40 kev electron total number flux, total energy flux and average energy are presented together with electron energy spectral displays which afford a detailed spectral analysis across the entire latitudinal extent of the electron precipitation region. The 1 to 40 kev proton total number flux and total energy flux profiles are also included but only to establish where the proton precipitation is located in relation to the electron precipitation, and to what extent the protons contribute to the total auroral luminosity. The electron total number and energy flux profiles are morphologically interpreted as composed of a background precipitation on which sit prominent peaks caused by one of three basic spectral changes in the otherwise maxwellian or exponential-like background spectra. The prominent peaks and a large portion of the background precipitation correlate well with discrete auroral forms and broad regions of visible diffuse aurora respectively. The data presented in this study and by Frank and Ackerson compare favorably in all morphological aspects and in total number and energy flux and average energy. A total particle energy flux threshold of 1 erg/cm^2-sec is established for the production of auroral luminosity just visible to the 35mm all-sky cameras used along the Alaskan all-sky camera chain. A substorm dependent particle precipitation morphology, and an electron precipitation oval are proposed. Winningham's precipitation morphology is discussed and amended.

PREFACE

The High Altitude Effects Simulation (HAES) Program sponsored by the Defense Nuclear Agency since the early 1970 time period, comprises several groupings of separate, but interrelated technical activities, e.g., ICECAP (Infrared *Chemistry Experiments*--Coordinated Auroral Program). Each of the latter have the common objective of providing information ascertained as essential for the development and validation of predictive computer codes designed for use with high priority DoD radar, communications, and optical defensive systems.

Since the inception of the HAES Program, significant achievements and results have been described in reports published by DNA, participating service laboratories, and supportive organizations. In order to provide greater visibility for such information and enhance its timely applications, significant reports published since early calendar 1974 shall be identified with an assigned HAES serial number and the appropriate activity acronym (e.g., ICECAP) as part of the report title. A complete and current bibliography of all HAES reports issued prior to and subsequent to HAES Report No. 1 dated 5 February 1974 entitled, "Rocket Launch of An SWIR Spectrometer into an Aurora (ICECAP 72)." AFCRL Environmental Research Paper No. 466, is maintained and available on request from DASIAC, DoD Nuclear Information and Analysis Center, 816 State Street, Santa Barbara, California 93102, Telephone: (805) 965-0551.

PRECEDING PAGE BLANK-NOT FILMED

This report, which is the fourth report under DNA Contract F19628-74C-0188 is the 35th report in the HAES series and covers technical activities performed during the period May through August 1975. The purpose of the work reported herein was to investigate auroral particle precipitation morphology as it relates to the visible aurora; to assist in ICECAP data interpretation; and to assist in planning and execution of the ICECAP program.

TABLE OF CONTENTS

	Page
Summary	iii
List of Illustrations	ix
List of Tables	xv
Section I - Instrumentation and Data Reduction	1
1.1 Introduction	1
1.2 Particle	2
1.3 The Alaskan All-Sky Camera Chain	3
1.4 The Procedure Used to Correlate Auroral Forms and Particle Precipitation	7
Section II - Data Presentation	14
2.1 Introduction	14
2.2 The March 16 Pass	17
2.2.1 General magnetic and auroral observations	17
2.2.2 Precipitation	19
2.2.3 Correlation	27
2.2.4 Summary	31
2.3 The April 7 Pass	31
2.3.1. General magnetic and auroral observations	31
2.3.2 Precipitation	34
2.3.3 Correlation	38
2.3.4 Summary	42
2.4 The March 14 Pass	43
2.4.1 General magnetic and auroral observations	43
2.4.2 Precipitation	47
2.4.3 Correlation	55
2.4.4 Summary	56

	Page
2.5 The March 9 Pass	58
2.5.1 General magnetic and auroral observations	58
2.5.2 Precipitation	60
2.5.3 Correlation	65
2.5.4 Summary	69
2.6 The March 7 Pass	69
2.6.1 General magnetic and auroral observations	69
2.6.2 Precipitation	72
2.6.3 Correlation	78
2.6.4 Summary	81
2.7 Chapter Summary	82
SECTION III	
3.1 Introduction	88
3.2 Precipitation Morphology	88
3.2.1 A comparison with Frank and Ackerson's Injun 5 Data	88
3.2.2 A proposed substorm related precipitation morphology	91
3.2.3 Comments on the substorm related electronic precipitation morphology proposed by Winningham	93
3.3 Total Energy Flux Threshold	105
3.4 Diffuse and Discrete Aurora	107
REFERENCES	110

LIST OF ILLUSTRATIONS

		Page
Figure 1	The coverage of the Alaskan All-Sky Camera Chain for 1972. The five 1971-089a satellite passes considered in this study are also indicated.	6
Figure 2	March 16 H-component magnetic records from stations located at various local magnetic times around the night side auroral zone. The M's mark local magnetic midnight at each station, and the vertical line (pass) indicates the time at which the satellite crossed Alaska. These records show that the pass occurred during an active but stable magnetic period about one hour before a magnetic substorm.	18
Figure 3	March 16 precipitation profiles showing peaks 1 through 6 and the subjectively drawn background precipitation. The letters A through D refer to the auroral arcs shown in Figure 9, and the arrows indicate the actual positions of these auroral arcs as determined from the Fort Yukon all-sky camera.	20
Figure 4	Seven point electron energy spectra associated with each of the one second data points in Figure 3. Time progresses horizontally from left to right in columns of 10 second intervals; each column progresses in time vertically from top to bottom in one second intervals. Spectra associated with the numbered peaks in the flux profiles in Figure 3 are indicated by the appropriate number. Note the well-defined extremum associated with peaks 1, 2, and 3 which seem to grow out of maxwellian and exponential-like "background" spectra.	22
Figure 5	March 16 selected peak 2 and adjacent background spectra. These spectra illustrate the development of a spectral extremum with an increase in the differential number flux over the entire energy spectrum. A moderate to large increase in the total energy flux, and a small increase in the average energy are attributed to this type of spectral change.	24
Figure 6	March 16 selected peak 3 and adjacent background spectra. These spectra illustrate the development of a spectral extremum with an increase in the differential number flux over the entire energy spectrum. A moderate to large increase in the total energy flux and a small increase in the average energy are attributed to this type of spectral change.	25

		Page
Figure 7	March 16 selected peak 1 and adjacent background spectra. These spectra illustrate the development of a spectral extremum with an increase in the differential number flux on the high energy side of the extremum as the extremum shifts towards higher energies. A large increase in both the total energy flux and average energy is attributed to this type of spectral change.	26
Figure 8	March 16 peak 5 and adjacent background spectra. These spectra illustrate the large increase in the <1 kev differential number flux while the higher energy differential number flux changes little. Usually a small increase in the total energy flux and a moderate to large decrease in the average energy are attributed to this type of spectral change.	28
Figure 9	Fort Yukon all-sky camera coverage of the March 16 pass. Auroral arcs A, B, C, and D were traversed by the satellite whose 110 km trajectory is represented by the sequence of dots. The trajectory point which corresponds closest in time to the all-sky photographs is indicated.	29
Figure 10	April 7 H-component magnetic records from stations located at various local magnetic times around the night side auroral zone. The M's mark local magnetic midnight at each station, and the vertical line (pass) indicates the time at which the satellite crossed Alaska. These records show that the pass occurred just at the beginning of a magnetic substorm prior to an auroral breakup in Alaska.	33
Figure 11	April 7 particle precipitation profiles showing peaks 1 through 3 and the subjectively drawn background precipitation. The letters A and B refer to the auroral arcs in Figure 15 and the arrows indicate the actual positions of these arcs as determined from the indicated all-sky camera stations.	36
Figure 12	Seven point electron energy spectra associated with each of the one second data points of Figure 11. Time progresses horizontally from left to right in columns of 10 second intervals; each column progresses in time vertically from top to bottom in one second intervals. Spectra associated with the numbered peaks in the flux profiles in Figure 11 are indicated by the appropriate number. Note the well-defined extremum associated with peaks 2 and 3 which seem to grow out of maxwellian and exponential like "background" spectra.	37

Page

Figure 13 April 7 selected peak 3 and adjacent background spectra. These spectra illustrate the development of a spectral extremum with an increase in the differential number flux on the high energy side of the extremum as the extremum shifts towards higher energies. A large increase in both the total energy flux and average energy profiles is attributed to this type of spectral change. 39

Figure 14 April 7 selected peak 1 and adjacent background spectra. These spectra illustrate the development of a spectral extremum with an increase in the differential number flux over most of the energy spectrum. A moderate to large increase in the total energy flux and a small increase in the average energy are attributed to this type of spectral change. 40

Figure 15 Inuvik and Fort Yukon all-sky camera coverage of the April 7 pass. Auroral arcs A and B were traversed by the satellite whose 110 km trajectory is represented by the sequence of dots. The trajectory point which corresponds closest in time to the all-sky photographs is indicated. 41

Figure 16 March 14 H-component magnetic records from stations located at various local magnetic times around the night side auroral zone. The M's mark local magnetic midnight at each station, and the vertical line (pass) indicates the time at which the satellite crossed Alaska. These records show that the pass occurred during the expansive phase of a magnetic substorm. 45

Figure 17 March 14 particle precipitation profiles showing peaks 1 through 3 and subjectively drawn background precipitation. The letters A, B, C, and P refer to the auroral arc, the edges of the diffuse aurora and the one patch shown in Figure 23. The arrows indicate the actual position of these auroral forms as determined from the indicated all-sky camera stations. 48

Figure 18 Seven point electron energy spectra associated with each of the one second data points in Figure 17. Time progresses horizontally from left to right in columns of 10 seconds; each column progresses in time vertically from top to bottom in one second intervals. Spectra associated with the numbered peaks in the flux profiles in Figure 17 are indicated by the appropriate number. Note the well-defined extremum associated with peak 2 which seem to grow out of maxwellian and exponential-like "background" spectra. 50

Page

Figure 19 March 14 selected peak 2 and adjacent background spectra. These spectra illustrate the development of a spectral extremum with an increase in the differential number flux on the high energy side of the extremum as the extremum shifts towards higher energies. A large increase in both the total energy flux and average energy is attributed to this type of spectral change. 51

Figure 20 March 14 selected peak 1 and adjacent background spectra. These spectra illustrate the increase in the differential number flux over the entire energy spectrum. A moderate to large increase in the total energy flux and a small increase in the average energy are attributed to this type of spectral change. 52

Figure 21 March 14 peak 3 and adjacent background spectra. These spectra show the large increase in the <1 kev differential number flux while the higher energy differential number flux changes little. A small to moderate increase in the total energy flux and moderate to large decrease in the average energy are attributed to this type of spectral change. 53

Figure 22 Inuvik, Fort Yukon, and Ester Dome all-sky camera coverage of the March 14 pass. Auroral arc A and the edges of the broad region of diffuse aurora B and C were traversed by the satellite whose 110 km trajectory is represented by the sequence of dots. The trajectory point which corresponds closest in time to the all-sky photograph is indicated. 54

Figure 23 March 9 H-component magnetic records from stations located at various magnetic local times around the night side auroral zone. The M's mark local magnetic midnight at each station, and the vertical line (pass) indicates the time at which the satellite crossed Alaska. The broad negative bay at Churchill and the very narrow and weak negative bay at college show that the satellite pass occurred just at the end of the expansive phase and the beginning of more intense magnetic substorm. 59

Figure 24 March 9 particle precipitation profiles showing peaks 1 and 2 and the subjectively drawn background precipitation. The letters A and B refer to the auroral arc and edge of the diffuse aurora shown in Figure 29. The arrows indicate the actual positions of these auroral forms as determined from indicated all-sky camera stations. 61

Page

Figure 25 Seven point electron energy spectra associated with each of the one second data points in Figure 25. Time progresses horizontally from left to right in columns of 10 seconds intervals; each column progresses in time vertically from top to bottom in one second intervals. Spectra associated with the numbered peaks in the flux profiles in Figure 26 are indicated by the appropriate number. Note the well-defined extremum associated with peak 2 and even some of the spectra in the uniform precipitation region equatorward. 63

Figure 26 March 9 selected peak 2 and adjacent background spectra. These spectra illustrate the development of a spectral extremum with an increase in the differential number flux on the high energy side of the extremum as the extremum shifts toward higher energies. A large increase in both the total energy flux and average energy profiles is attributed to this type of spectral change. 64

Figure 27 March 9 selected peak 1 and adjacent background spectra. These spectra illustrate the increase in the differential number flux over most of the energy spectrum. A moderate to large increase in the total energy flux and a small to moderate increase in the average energy are attributed to this type of spectral change. 66

Figure 28 Inuvik, Fort Yukon, and Ester Dome all-sky camera coverage of the March 9 pass. Auroral arc A and equatorward edge of broad region of diffuse aurora B were traversed by the satellite whose 110 km trajectory is represented by the sequence of dots. The poleward edge of diffuse aurora not visible due to clouds. The trajectory point which corresponds closest in time to the all-sky photographs is indicated. 67

Figure 29 March 7 H-component magnetic records from stations located at various local magnetic times around the night side auroral zone. The M's mark local magnetic midnight at each station, and the vertical line (pass) indicates the time at which the satellite crossed Alaska. These records show that the pass occurred after a magnetic substorm during a complicated magnetic period. 70

Figure 30 March 7 particle precipitation profiles showing peaks 1 through 9 and the subjectively drawn background precipitation. The letters A through F refer to the auroral arcs in Figure 34 and the arrows indicate the actual positions of these auroral arcs as determined form the indicated all-sky camera stations. 73

		Page
Figure 31	Seven point electron energy spectra associated with each of the one second data points in Figure 30. Time progresses horizontally from left to right in columns of 10 seconds intervals; each column progresses in time vertically from top to bottom in one second intervals. Spectra associated with the number peaks in the flux profiles in Figure 30 are indicated by the appropriate number. Note that there does not exist any spectra exhibiting a well-defined extremum as has been seen in previous four passes.	75
Figure 32	March 7 selected peak 2 and adjacent background spectra. These spectra illustrate the increase in the differential number flux over the entire energy spectrum. A moderate to large increase in the total energy flux and a small to moderate increase in the average energy are attributed to this type of spectral change.	76
Figure 33	March 7 peak 7, 8, and adjacent background spectra. These spectra illustrate the large increase in the low energy differential number flux while the higher energy differential number flux increased only slightly.	77
Figure 34	Inuvik, Fort Yukon, and Ester Dome all-sky camera coverage of the March 7 pass. Auroral arcs A, B, C, D, E, and F were traversed by the satellite whose 110 km trajectory is represented by the sequence of dots on the photographs. The trajectory point which corresponds closest in time to the all-sky photograph is indicated.	79
Figure 35a	March 16 electron precipitation profiles showing the CPL and BPL regions according to Winningham et al. (1975).	96
Figure 35b	April 7 electron precipitation profiles showing the CPL and BPL regions according to Winningham et al. (1975).	97
Figure 35c	March 14 electron precipitation profiles showing the CPL and BPL regions according to Winningham et al. (1975).	98
Figure 35d	March 9 electron precipitation profiles showing the CPL and BPL regions according to Winningham et al. (1975).	99
Figure 35e	March 7 electron precipitation profiles showing the CPL and BPL regions according to Winningham et al. (1975).	100
Figure 36a	March 14 electron precipitation profiles showing the TPL region proposed in the text.	102

Page

Figure 36b March 9 electron precipitation profiles showing the TPL region proposed in the text. 103

Figure 36c March 7 electron precipitation profiles showing the TPL region proposed in the text. 104

LIST OF TABLES

Table 1 Bandwith and average energy of Lockheed electron particle detectors of USAF satellite 1971-089a. 3

Table 2 Geographic and geomagnetic coordinates of all-sky camera stations along the 1972 Alaskan all-sky camera meridian chain and the type of cameras in operation at each station. 5

Table 3 Simple estimates of three major all-sky camera sources of errors. 10

Table 4 UT data and time, local magnetic time, K_p, Dst, and substorm phase of each pass. 15

Table 5 Summary of the electron energy spectral changes and associated auroral luminosity for March 16. 32

Table 6 Summary of electron energy spectral changes and associated auroral luminosity for April 7. 44

Table 7 Summary of the energy spectral changes and associated auroral luminosity for March 14. 57

Table 8 Summary of the energy spectral changes and associated auroral luminosity for March 9. 68

Table 9 Summary of electron energy spectral changes and associated auroral luminosity for March 7. 83

Table 10 A summary of the latitudinal extent and significant features of the electron precipitation observed by the Lockheed instrumented satellite. 86

SECTION 1. INSTRUMENTATION AND DATA REDUCTION

1.1 INTRODUCTION

There have been several correlation studies of auroral particle precipitation and all-sky camera observations of auroral forms. More recently Ackerson and Frank (1972) correlated one "band of precipitation" with an early evening discrete auroral form, Winningham, et al. (1973) correlated two midday auroral arcs with Isis particle data nd Pazich (1972) correlated rocket particle data with one early evening auroral arc. However, there has been no correlation of the full latitudinal extent of the auroral precipitation zone and all-sky camera observations of the aurora along a meridian chain of stations. This study is such a correlation, and has been partially funded by National Science Foundation Grants GA-31876X and GA-38795 with the satellite experiment supported by the Defense Nuclear Agency and the Office of Naval Research.

Five Lockheed instrumented polar orbiting satellite passes across Alaska in the late evening sector were selected for correlation with all-sky data obtained from the Alaska all-sky camera chain of stations. The Lockheed particle detectors provide seven point electron spectra over a 60 ev to 40 kev spectral energy range. The one second (8 km) resolution capability of these detectors then provide a detailed spectral energy analysis of the entire latitudinal extent of the late evening auroral zone electron precipitation. This spectral analysis together with all-sky camera observations of the complete latitudinal extent of the auroral zone luminosity will help to unify particle and auroral morphology, which for the most part has been discussed in separate terms.

1.2 PARTICLE DETECTORS

The Lockheed instrumented USAF satellite 1971-089A was launched in October 1971 into a near circular polar orbit at an approximate altitude of 800 km. The low energy (E<50 kev) particle precipitation data to be presented were obtained from an array of particle analyzers which make use of channel multiplier tubes as the detecting element with particle identification and energy analysis performed either magnetically or by a foil threshold in the case of some of the proton detectors. The nominal orientation to zenith and the field of view of the particle detector, were 15^{o} and $\pm$ 5 respectively. The accuracy and reliability of any satellite particle data depends not only on the pre-flight calibration procedures, but also on the changes in both detector and electronic performance during the flight. In an effort to reduce overall post-launch uncertainties in gain and energy threshold and in electronic calibration curves to a minimum, a novel and elaborate in-flight calibration scheme is employed by the Lockheed group. The in-flight calibration together with the pre-flight calibration quarantees a 30% accuracy in the count rates in all detectors. The satellite payload description and calibration techniques are described by R. G. Johnson et al. (1969).

The array of Lockheed electron analyzers produced once each second (8 km horizontal travel) differential number flux quantities for the energy ranges and mean energies listed in Table 1. From these differential energy spectra, electron total number flux, total energy flux, and average energy latitudinal profiles, with an 8 km resolution across the auroral zone, can be produced. Also from the >16 and >38 kev proton detectors, 1 to 40 kev proton total number and energy flux latitudinal profiles can be obtained.

TABLE 1

Bandwith and average energy of Lockheed electron particle detectors on USAF satellite 1971-89a.

electron	
ΔE (kev)	$\bar{E}$ (kev)
0.064-0.26	0.16
0.29-0.92	0.60
0.98-1.8	1.4
1.8-3.4	2.6
3.3-6.1	4.71
6.2-11.0	8.8
11.0-37.0	24

1.3 THE ALASKAN ALL-SKY CAMERA CHAIN.

In the spring of 1972, the Alaskan meridian all-sky camera chain was composed of the following five stations: Ester Dome, Fort Yukon, Inuvik, Sachs Harbor, and Mould Bay. The geographic and geomagnetic coordinates of these stations are listed in Table 2. In Figure 1, the location of the five all-sky camera stations and the radial extent of the effective 110 km intercept field of view of each station are shown together with the trajectories of the five satellite passes studied in this paper. The fields of view overlap in such a way that a narrow region of the auroral zone extending approximately 62° to 76° latitude can be monitored by the chain. Under most magnetic conditions, this region easily encompasses the latitudinal extent of the instantaneous late evening auroral oval; thus making possible a coordinated study of complete particle precipitation profiles and types of auroral forms observed along the Alaskan meridian all-sky camera chain.

Two basic types of all-sky cameras were in operation along the Alaskan all-sky camera chain during the spring of 1972 and are indicated in Table 2. At each station a 180° field of view f/1.9 Kodak K-100 16mm all-sky camera using Kodak 4X film was routinely operated. In support of the Poker Flat Rocket Range launch schedule, 160° field of view f/1.5 Automax 35mm cameras using Kodak 2485 film were run on a selected time basis at Ester Dome and Fort Yukon. The 35mm cameras operated for the better part of each night associated with the five satellite passes to be presented, and as a result, the 16mm data from these two stations were only used to establish the auroral conditions an hour or two after dusk and before dawn. The 16mm cameras framed one a minute with an exposure of 8 seconds. The 35mm cameras framed at 8, 4, 2, and 1 seconds in a 20-second cycle. The 8-second exposure was chosen for this study. This exposure effectively produces twice the exposure of the 16mm cameras for the same exposure length. On a single frame basis, the 35mm all-sky camera film reveals by far more auroral detail than does the 16mm film because of the larger film format and exposure. However, considerable auroral detail can be obtained from the 16mm all-sky data if the 16mm film is projected in cine mode. The weaker exposures whose contrast with the background is too weak to be seen on a single frame basis become apparent to the eye during movie projection because of the relative motions which exist between the randomly moving grains and the deliberate movement of the luminous auroral forms. The movie projector then acts as a device which optically recovers signal from noise. Unfortunately, movie projection cannot be shown in a written report;

Station name	Station Abbreviation	Geographic Lat. N.	Geographic Long. W.	Geomagnetic Lat. N.	Geomagnetic Long. E.	Camera type
Ester Dome	EDO	64°52.8'	148°3.2'	64°46.8'	257°18.2'	16mm and 35*mm
Fort Yukon	FTY	66°33.6'	145°13.1'	66°48.6'	257°53.9'	16mm and 35*mm
Inuvik	INU	68°15.0'	133°18.0'	70°35.2'	266°24.4'	16mm
Sachs Harbor	SAH	72°00.0'	125°00.0'	75°16.2'	266°45.9'	16mm
Mould Bay†	MOB	76°12.0'	119°24.0'	79°16.8'	257°42.8'	16mm

*used only in the correlation

†not used at any time due to poor weather and extreme northern location

TABLE 2

Geographic and geomagnetic coordinates of all-sky camera stations along the 1972 Alaskan all-sky camera meridian chain and the type of cameras in operation at each station.

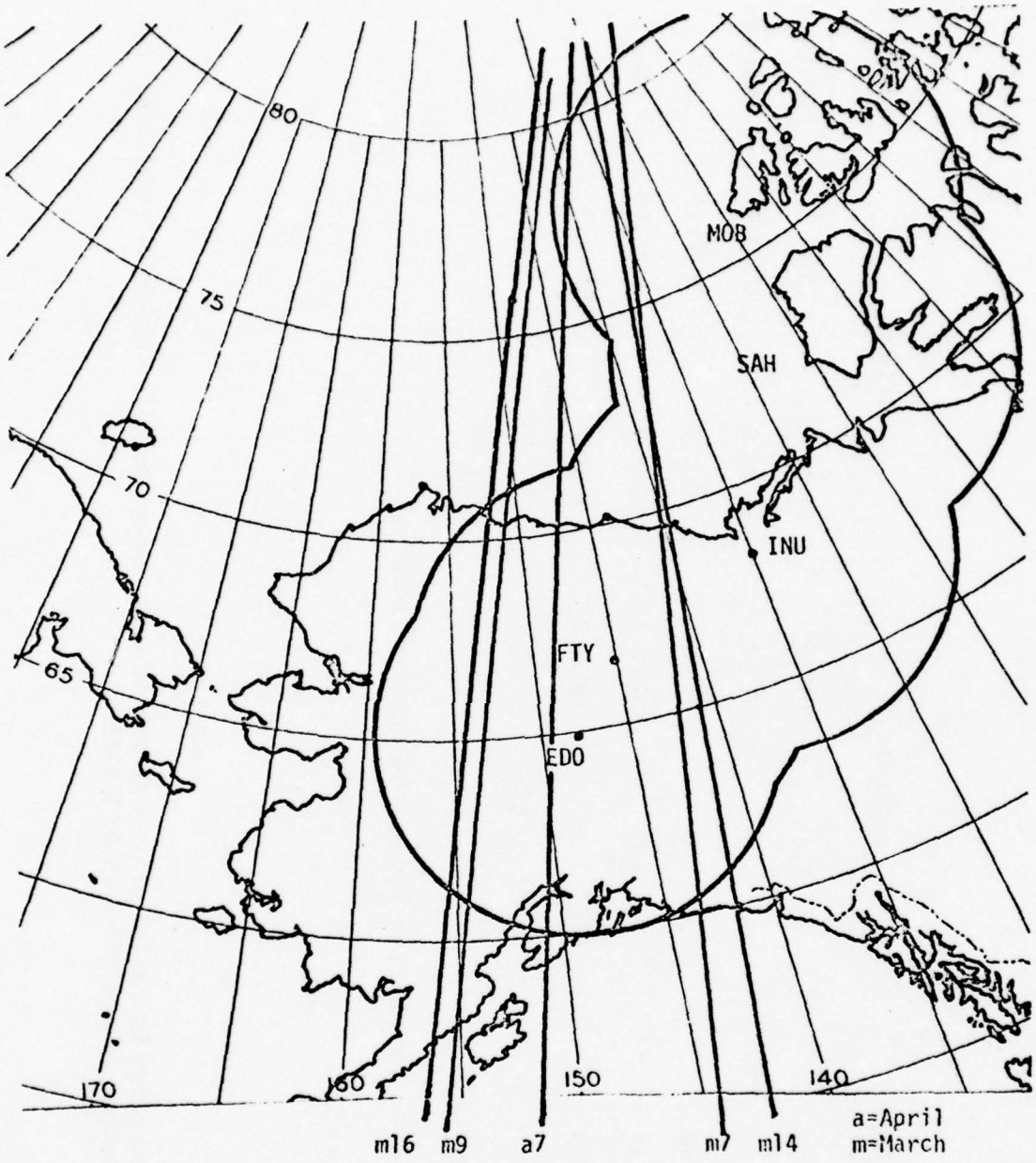

Figure 1

The coverage of the Alaskan All-Sky Camera Chain for 1972. The five 1971-089a satellite passes considered in this study are also indicated.

however, at times it will be necessary to indicate the location of those auroral forms visible only by movie projection on some of the 16mm reproductions.

1.4 THE PROCEDURE USED TO CORRELATE AURORAL FORMS AND PARTICLE PRECIPITATION

When correlating visible auroral forms and the particle precipitation observed by a satellite, it is convenient to place selected satellite ephemeris points or time positions on the all-sky camera photograph. In this way, the intersection of any auroral form and the satellite trajectory can be determined relative to the satellite ephemeris and can then be easily located on the precipitation profiles for comparison. It should be pointed out that there usually exists a large height difference between the altitudes of the satellite and the lower border of an auroral form. If this height difference is not accounted for, the satellite will be observed on the all-sky photograph to cross an auroral form several seconds before or after it actually encounters those field lines which guide the associated particle flux. To correct for this height difference, the satellite ephemeris points are traced down the geomagnetic field lines to the lower border of the auroral form. These new ephemeris points are then placed on the all-sky photograph. Stormer (1955) has shown that the lower border of most auroral forms occurs at altitudes between 80 and 150 km but most frequently at 100 km. Since the peak luminosity occurs approximately 10 km above the lower border, the satellite ephemeris in this study was relocated at the 110 km level before being placed on the all-sky photographs. This relocated trajectory is called "the 110 km field line intercept trajectory" or simply "the 110 km trajectory." The geomagnetic field line computer model Pogo

10-68 (Goddard Space Fight Center Report, 1972) was used to obtain the 110 km trajectory from the satellite 10 second ephemeris coordinates. Errors which result due to small height discrepancies between 110 km and the actual height of the peak luminosity will be discussed later in this section, but first a description of the procedure used to place the 110 km trajectory points on the all-sky camera photographs will be given.

The all-sky camera photograph is a two dimensional polar projection of most or all of the sky. The superwide angle optical system of the all-sky camera causes radial distortion which becomes extreme near the edge of the field of view, that is, for large zenith angles. The procedure used to position the 110 km trajectory points onto the all-sky photograph is as follows:

(1) Convert the geographic coordinates of each 110 km trajectory positions into an azimuth and zenith angle relative to the known geographic position of the all-sky camera station.

(2) Convert the computed zenith angles into all-sky camera radii. The all-sky camera radius is the ratio of the distance from the center of the all-sky photograph to the point of interest and the radius of the all-sky photograph. The conversion of the zenith angles to all-sky radii is accomplished through the use of the all-sky calibration curve which accounts for radial distortion by expressing the functional relation between the zenith angle and the all-sky radius.

(3) Plot the all-sky radius vectors on the all-sky photograph. The all-sky camera radii together with the azimuth angles define radius vectors the end points of which can be easily plotted on the circular all-sky photograph.

In this study a computer program was used to convert the 110 km trajectory points into all-sky radius vectors which were computer plotted on five inch diameter simulated all-sky camera polar plots. These plots were then overlaid on the five inch diameter all-sky photographs so that the 110 km trajectory points could be easily marked on the all-sky photographs.

As will be shown in Chapter 2, there is a difference of some satellite seconds between the location of an auroral form determined from the 110 km ephemeris points and the obvious region of particle flux responsible for producing the auroral form. This is due to several sources of error. The sources of error which contribute most to the total error are:

(1) all-sky camera tilt

(2) height difference between auroral form and the 110 km trajectory altitude

(3) one-minute time resolution of the all-sky camera frame sequence

These errors are a function of the orientation of the satellite's trajectory relative to the auroral forms encountered, and therefore, cannot be expressed in a simple quantitative way. However, if we consider the particular simple situation of the tilt axis aligned along the east-west meridian and the satellite's trajectory and motion of the auroral form aligned along the magnetic north-south meridian, then estimates of the error can be determined at various zenith angles. It is assumed that these estimates are not likely to be greatly exceeded by the errors resulting under more general situations. The validity of

Zenith Angle	Tilt 1° km	Tilt 1° sec	Height difference 40 km km	Height difference 40 km sec	Time resolution km	Time resolution sec	Total worst possible error km	Total worst possible error sec
30°	2	.3	13	1.5	15	1.9	±30	3.7
40°	3	.4	18	2.2	15	1.9	±36	4.5
50°	5	.6	20	2.5	15	1.9	±40	5.0
60°	7	.9	35	4.4	15	1.9	±57	7.1
70°	10	1.3	50	6.3	15	1.9	±75	9.4

TABLE 3

Simple Estimates of Three Major All-Sky Camera Sources of Errors.

this assumption will become evident in the actual correlations presented in Chapter 2. The estimated errors (expressed in seconds and kilometers) at various zenith angles for each of the three sources mentioned above are listed in Table 3. The table does not list errors for zenith angles larger than 70° since these errors are so large that a correlation in most cases is not practical. The three sources of error and their estimates will now be discussed.

Ideally the geographic zenith of an all-sky camera station and the center of the all-sky photograph should coincide. Because it is impossible to level the all-sky camera perfectly, there is always a tilt which causes a displacement of the geographic zenith from the center of the circular all-sky photograph. The displacement is then a measure of the tilt. Tilt is usually small on ground-based all-sky cameras provided the cameras are leveled properly when installed. The amount of tilt can be measured by first determining the geographic zenith on the all-sky photograph from the star field and then measuring the displacement which when converted to a zenith angle is the tilt. This procedure was followed to obtain the tilt for the Ester Dome and Fort Yukon 35mm all-sky cameras. These two tilts were found to be 1/2° and 3/4° respectively. Unfortunately, no star field could be seen on the 16mm all-sky frames except when run through a movie projector which was not amenable to a star field study. It can be assumed that the tilt for these cameras did not exceed 1°. Table 3 lists the error caused by a 1° tilt at various zenith angles.

As explained earlier in this section, any height difference between the altitudes of an auroral form and a satellite will result in the

satellite being observed to cross an auroral form several kilometers or seconds before it actually encounters the geomagnetic fields attached to the auroral form. Most of this error can be eliminated by tracing the satellite's trajectory down the magnetic field lines to the altitude of the auroral form in our case at an altitude of 110 km. But the altitudes of auroral forms were observed in Stormer (1955) to vary between 80 and 150 km. Thus a 40 km height difference is possible. Table 3 lists for various zenith angles, the number of seconds (kilometers) the satellite is from an auroral form when it is observed to cross it on the all-sky camera photograph due to a 40 km height difference.

The last major source of error stems from the 1 minute time resolution of the all-sky camera. If the satellite's 100 km trajectory crosses an auroral form between frames, the time of the crossing is uncertain since the aurora could and is likely to be moving. The time at which the auroral form is crossed by the satellite is determined from the frame closest to the crossing, but this time and the time when the auroral form was actually crossed could vary considerable. Bhattacharya (1960) measured horizontal motions in the magnetic east, west, north, and south direction of several auroral forms. From resulting auroral speed histograms, it is obvious that speeds seldom exceed 500 meters/sec in any of the four magnetic directions. For the worst possible situation of the satellite crossing an auroral form half way between one minute frames, the auroral form would be moving for 30 seconds or a distance of 15 km. This error is not a function of zenith angle and is listed in Table 3.

The last column in Table 3 is the total of these errors. Since the individual errors could actually compensate one another when combined,

the total error is to be taken as the worst possible error under the simple conditions considered in this discussion. The worst error is 80 km at 70° zenith angle. Of all the correlations made in Chapter 2, only once does the matching of an auroral form and the associated precipitation differ by more than 80 km. As will become evident in Chapter 2, 80 km is small compared to the separation of prominent luminosity producing precipitation regions.

SECTION 2. DATA PRESENTATION

2.1 INTRODUCTION

This chapter deals with the presentation and discussion of the magnetic, particle precipitation, and all-sky camera data associated with each of the five satellite passes. These five passes were selected on the basis of substorm phase, availability of 35mm all-sky camera data, and nearness of the satellite's trajectory to the chain of all-sky cameras. Table 4 lists the UT date and time, magnetic local time, K_p, Dst, and substorm phase associated with each pass.

H-component magnetic records from stations located at various local magnetic times around the night side auroral zone for the day associated with each of the five passes are shown. On the records are marked local magnetic midnight for each station and the time at which the satellite crossed Alaska. To indicate the general state of the magnetosphere, the three hourly K_p, and the hourly Dst values are listed below each set of magnetic records. The polar geomagnetic disturbance and the associated auroral activity leading up to and beyond the satellite pass are described in order to establish substorm phase during the time of each pass.

Latitudinal precipitation profiles of the 0.6 to 40 kev electron total number flux, total energy flux, and average energy and the 1 to 40 kev proton total number and energy flux are presented. The proton data are not discussed in the same detail as the electron data. The proton data are included only to establish where the proton precipitation is located in relation to the electron precipitation and to what extent the protons contribute to the total auroral luminosity. Electron energy spectra associated with each of the one second data points in the

Date 1972	UT	∿MLT	K_p	Dst	Substorm phase
March 7	9:04	22:18	5^+	-50	after recovery
March 9	9:41	22:00	3^+	-12	end of expansive phase
March 14	8:47	21:42	2^-	-4	expansive phase
March 16	9:27	22:00	3^-	-38	1 hr. before breakup
April 7	8:08	20:36	3^+	-16	1/2 hr. before breakup

TABLE 4

UT Date and Time, Local Magnetic Time, K_p, Dst, and Substorm Phase of Each Pass.

electron latitudinal profiles are presented in time sequence. Because of the large number of spectra, convenient presentation is difficult. Small log-log scales are used and as a result only gross spectral features are evident. The differential number flux and energy scales usually range from 10^5 to 10^9 electrons/(cm^2-sec-st-kev) and from 0.1 to 100 kev respectively. At times differential number fluxes may exceed 10^9/(cm^2-sec-st-kev), in which case, a regrettable but necessary one decade scale change occurs without indication. As a result of these difficulties, it is necessary to plot selected spectra on larger scales for better comparisons. The spectral terms, "hard" and "soft," are not used to describe the spectral variations across the auroral zone because these terms do not convey precisely the manner in which the spectral variations occur. For example, a hardening in the energy spectra can mean either an increase in the differential number flux at the high end of the energy spectrum or a decrease in the differential number flux at the low energy end of the energy spectrum or some combination of the two. The term "hardening" does not convey which of these processes actually takes place. Thus, the pictorial method has been chosen to indicate energy spectrum variations with latitude.

In order to correlate particle precipitation with auroral luminosity, a set of all-sky camera photographs which gives the best coverage of the auroral oval at the time of each pass were chosen. By comparing the same aurora from two different stations, it becomes obvious that the camera clocks are not synchronized; a minute difference is not uncommon. Because of the uncertainly in time, the satellite's ten second 110 km field line intercept time positions are displayed on the three photographs

nearest the time at which the satellite passed over each station. Of these three photographs, the one which gives the best correlation is used. For reference, the ten second time position which corresponds closest to the photograph's time is indicated on each of these photographs.

2.2 THE MARCH 16 PASS.

2.2.1 General magnetic and auroral observations.

Figure 2 shows the March 16 H-component magnetic records from stations located at various local magnetic times around the night side auroral zone. The M's mark local magnetic midnight at each station, and the vertical line marks the time at which the Lockheed instrumented satellite crossed Alaska. Listed are the three-hourly K_p values and the hourly Dst values. The three negative bays observed in the early evening sector by the Canadian stations between 1:00 and 4:00 UT as well as the positive bays observed in the afternoon sector by the Alaskan stations between 1:30 and 7:00 UT were the polar geomagnetic responses to successive magnetospheric substorms. The Dst values indicate that a moderately intense geomagnetic storm was in progress during the time of this pass. The geomagnetic storm began its main phase decrease by about 1:30 UT, reached its peak intensity at 5:00 UT, and then it began to recover by 6:00 UT. At 6:30 UT, the magnetic activity at the four Alaskan stations also began to recover and remained stable between 7:00 to 10:00 UT. However, during this period, both Dst and the polar magnetic activity never reached quiet time levels; that is, there always remained a substantial ring current and an east-west electrojet. This interpretation is also in agreement with Greenwald's radar observations of the auroral electrojet, Greenwald, et al. (1973).

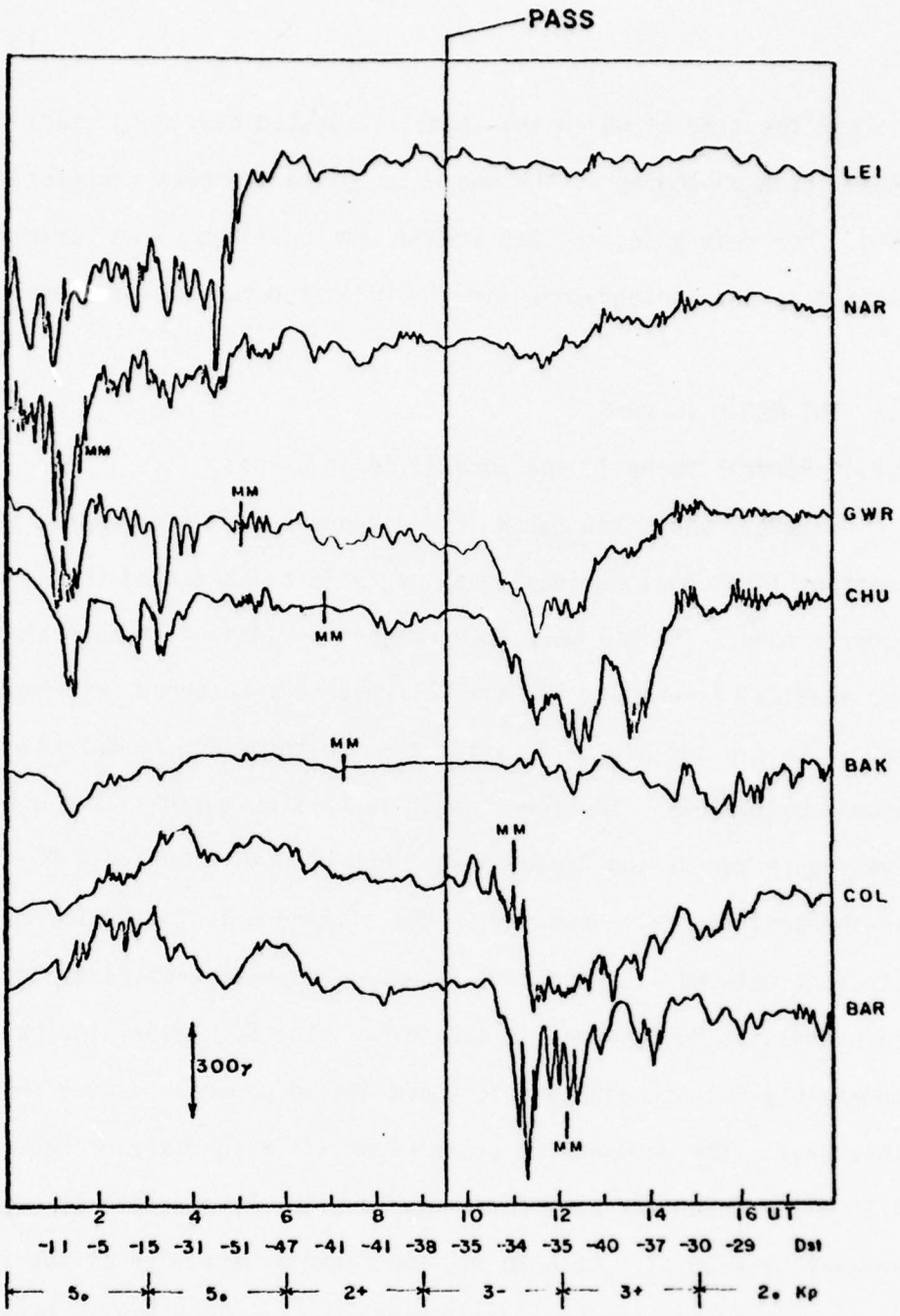

Figure 2

March 16 H-component magnetic records from stations located at various local magnetic times around the night side auroral zone. The M's mark local magnetic midnight at each station, and the vertical line (pass) indicates the time at which the satellite crossed Alaska. These records show that the pass occurred during an active but stable magnetic period about one hour before a magnetic substorm.

Just after dusk (5:30 UT), multiple auroral arcs were observed to span the entire latitudinal field of view of the Inuvik all-sky camera. All of these arcs showed considerable motions and distortions except for the most equatorward arc which was located near the Fort Yukon zenith. By 7:00 UT, the arc system had moved to between Ester Dome and Fort Yukon. At different periods between 7:00 and 10:00 UT, one to several auroral arcs were observed. These arcs repeatedly intensified and became distorted, but in spite of this active nature, the arc system confined itself to the field of view of the Fort Yukon all-sky camera. Thus, during the time between 7:00 and 10:00 UT, both the auroral and magnetic activity remained stable. In the latter part of this period (9:37 UT), the satellite crossed the stable multiple arc system, and shortly after, the magnetic activity at College began to increase presumably due to the development of several spirals between Fort Yukon and Ester Dome. By 10:30 UT, a moderate intense polar magnetic substorm began; the Fort Yukon sky suddenly became filled with very intense and active poleward advancing aurora which reached well beyond the zenith at Inuvik and lasted until 12:00 UT. From then until dawn occasional patches of aurora were observed overhead at Fort Yukon.

In summary, the satellite crossed the Alaskan auroral zone during an active but stable auroral and magnetic period about an hour before an auroral substorm. The entire region of visible auroral luminosity was confined to the Fort Yukon vicinity and several auroral arcs were traversed by the satellite.

2.2.2 Precipitation.

Figure 3 shows the particle precipitation profiles observed by the

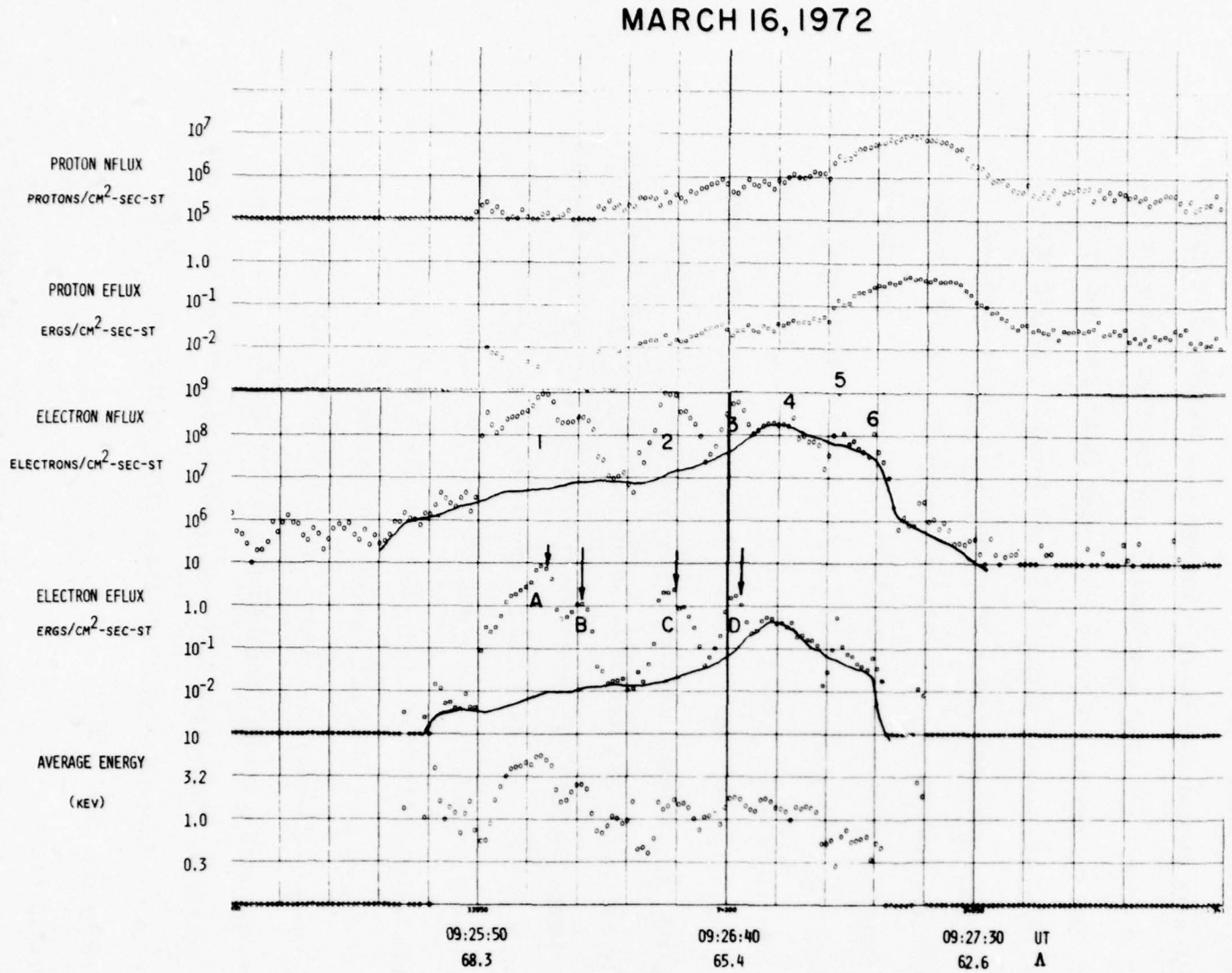

Figure 3

March 16 precipitation profiles showing peaks 1 through 6 and the subjectively drawn background precipitation. The letters A through D refer to the auroral arcs shown in Figure 9, and the arrows indicate the actual positions of these auroral arcs as determined from the Fort Yukon all-sky camera.

satellite on March 16. In both the total number flux and total energy flux profiles, three prominent peaks are discernible on a background precipitation whose latitudinal extent is 5.2°Λ and has sharp boundaries at 68.9°Λ and 63.7°Λ. The three peaks are labeled 1, 2, and 3 and a subjectively drawn background precipitation are indicated in Figure 3. The total energy flux, average energy and latitudinal extent of peak 1 is particularly larger than that of peaks 2 and 3. The total number and energy flux of the background precipitation is shown to increase with decreasing latitude to a maximum value of 10^8 el/(cm^2-sec-st) and 0.4 ergs/(cm^2-sec-st) respectively just equatorward of peak 3 and then decrease to threshold about 1.2° farther equatorward. Three narrow peaks one second in extent are evident on the equatorward end of the background precipitation and are labeled 4, 5, and 6 in Figure 3. Note that unlike the three poleward peaks, the average energy associated with peaks 4, 5, and 6 exhibit a decrease which signifies an enhanced low energy (<1 kev) differential number flux.

The proton precipitation is comprised of a single broad peak located just equatorward of the electron precipitation region and extends approximately 1.2° equatorward. The total energy flux of both the proton and equatorward end of the background electron precipitation are comparable in magnitude.

Figure 4 shows in time sequence, the seven point electron energy spectra associated with each of the one second data points in Figure 3. Time progresses horizontally from left to right in columns of 10 second intervals; each column progresses in time vertically from top to bottom in one second intervals. Spectra associated with the numbered peaks in

MARCH 16, 1972

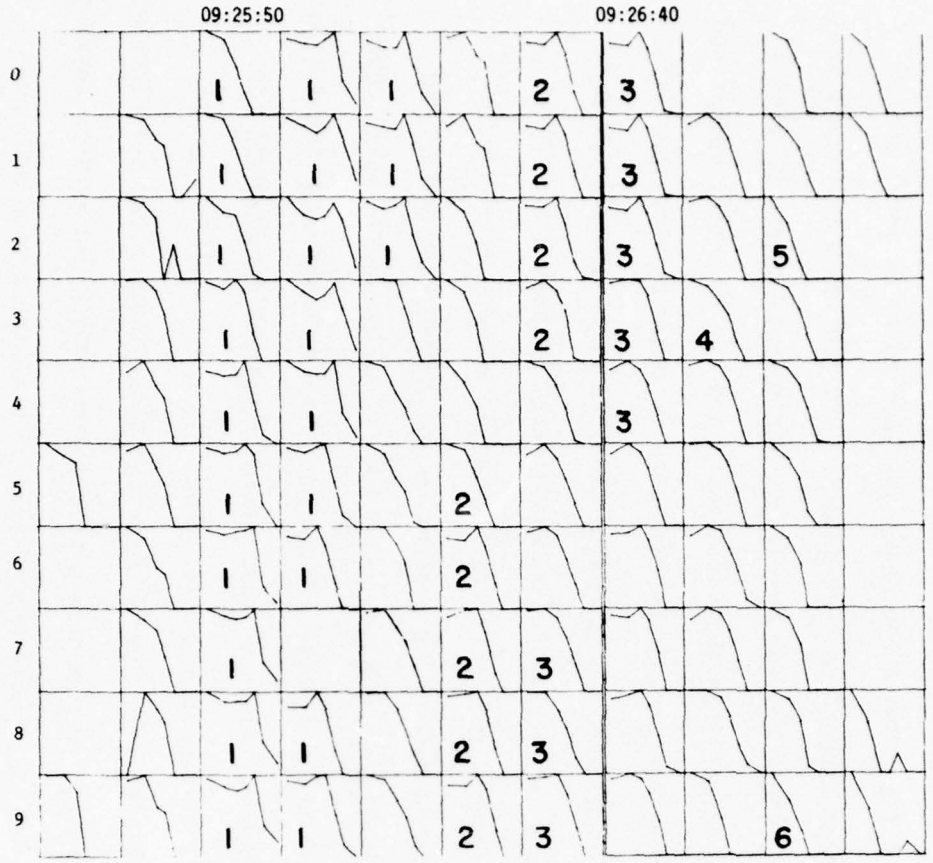

Figure 4

Seven point electron energy spectra associated with each of the one second data points in Figure 3. Time progresses horizontally from left to right in columns of 10 second intervals; each column progresses in time vertically from top to bottom in one second intervals. Spectra associated with the numbered peaks in the flux profiles in Figure 3 are indicated by the appropriate number. Note the well-defined extremum associated with peaks 1, 2, and 3 which seem to grow out of maxwellian and exponential-like "background" spectra.

the flux profiles in Figure 3 are indicated by the appropriate numbers in Figure 4. The most obvious spectral feature is the single well-defined extremum associated with peaks 1, 2, and 3. The extrema seem to grow out of maxwellian and exponential-like background spectra. Figures 5, 6, and 7 show selected energy spectrum from peaks 2, 3, and 1 respectively. Their adjacent background spectra are also plotted to illustrate the subtle spectral changes not apparent in Figure 4. Compared to the background spectra, differential number flux associated with peaks 2 and 3 (Figures 5 and 6) are greatly increased over the entire energy range. Of course, the increase in the differential number flux at the low end of the energy spectrum aided by the development of the extrema accounts for the two prominent peaks in the total number flux profile. The overall increase in the differential number flux is not symmetric but is somewhat biased towards the higher energy end of the spectrum as the increase in the average energy in Figure 3 indicates. However, this increase in the average energy associated with peaks 2 and 3 is small compared to the increase associated with peak 1, and from Figure 7, the reason is immediately obvious. With the development of the extremum, the differential number flux for energies at or greater than the extremum energy substantially increases as the extremum shifts towards higher energies. Subsequently, the extremum decreases in intensity and moves back to lower energies. This kind of spectral behavior which will reoccur in all but the March 7 precipitation not only greatly favors a large increase in the total energy flux, but also in the average energy, such as the factor of 5 increase associated with peak 1 in Figure 3. As will be discussed in Chapter 3, this latter spectral change is the

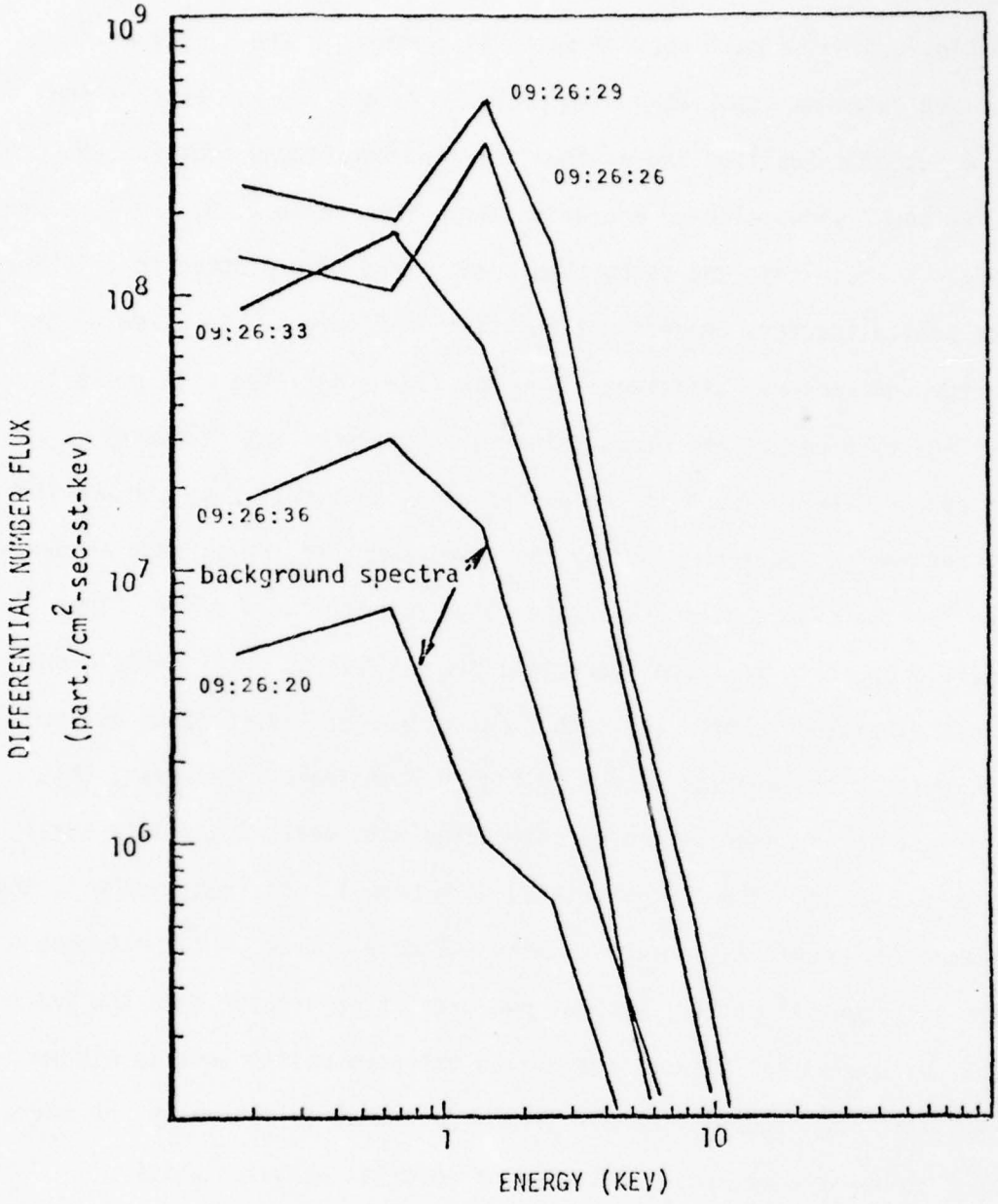

Figure 5

March 16 selected peak 2 and adjacent background spectra. These spectra illustrate the development of a spectral extremum with an increase in the differential number flux over the entire energy spectrum. A moderate to large increase in the total energy flux, and a small increase in the average energy are attributed to this type of spectral change.

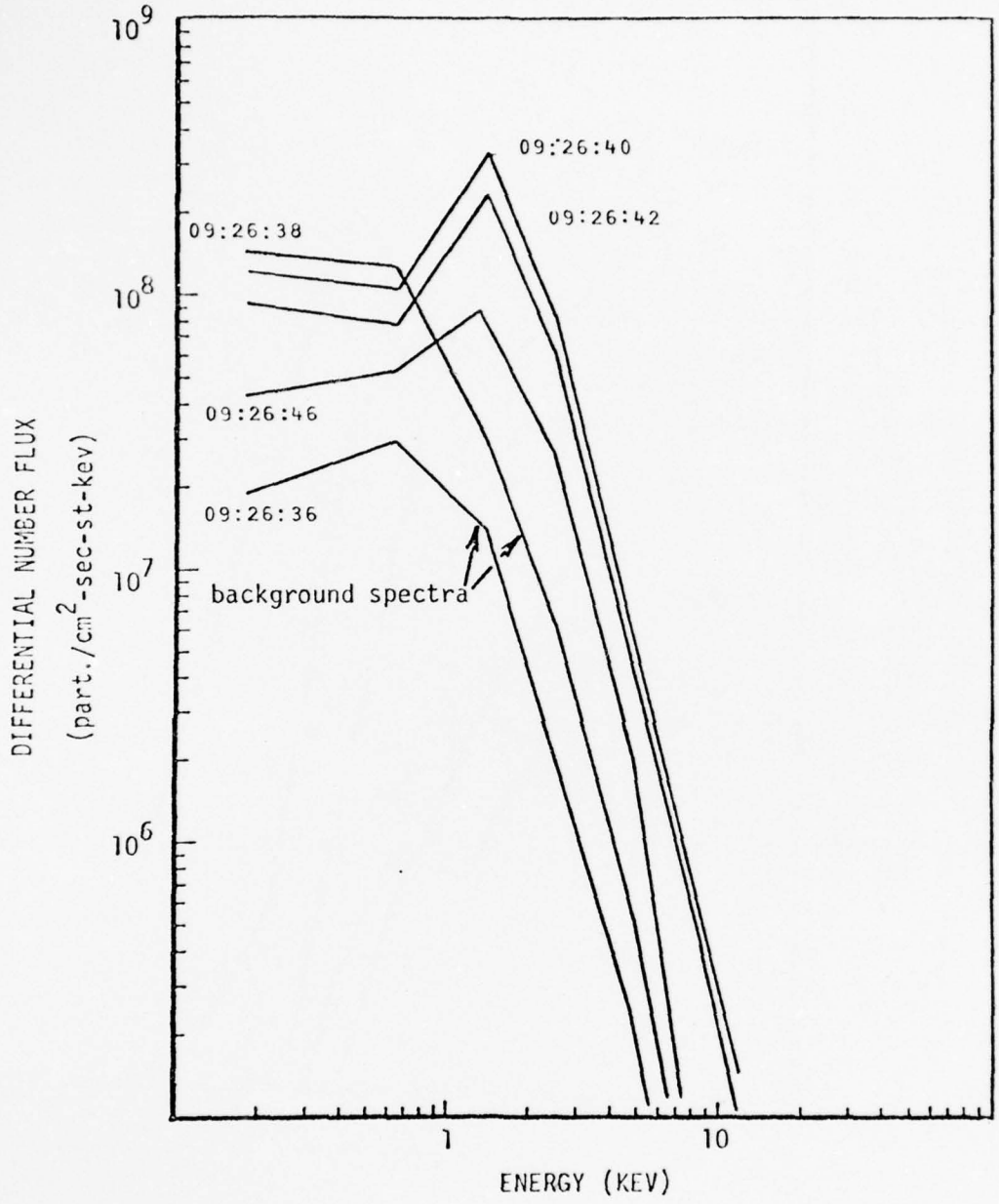

Figure 6

March 16 selected peak 3 and adjacent background spectra. These spectra illustrate the development of a spectral extremum with an increase in the differential number flux over the entire energy spectrum. A moderate to large increase in the total energy flux and a small increase in the average energy are attributed to this type of spectral change.

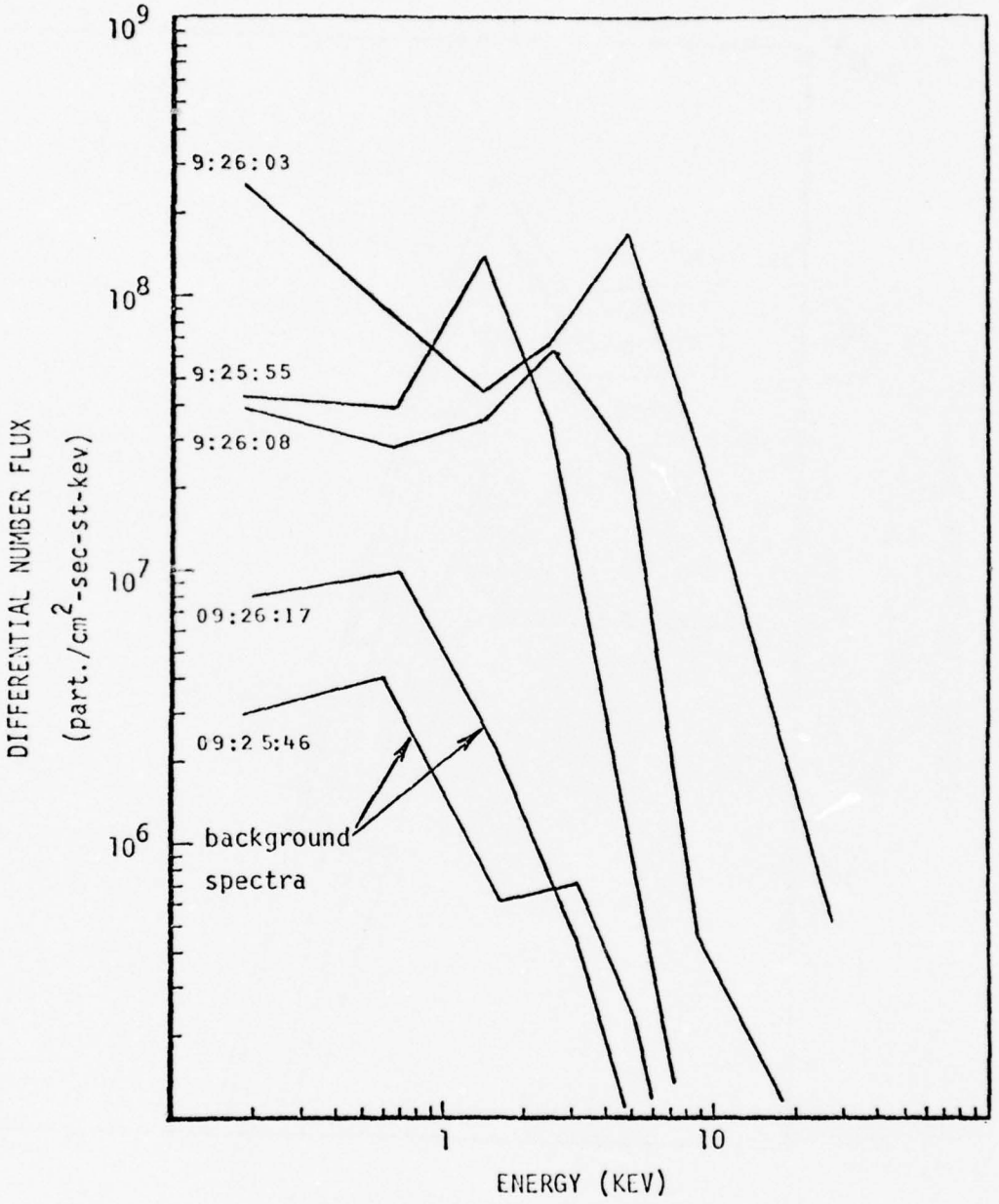

Figure 7

March 16 selected peak 1 and adjacent background spectra. These spectra illustrate the development of a spectral extremum with an increase in the differential number flux on the high energy side of the extremum as the extremum shifts towards higher energies. A large increase in both the total energy flux and average energy is attributed to this type of spectral change.

necessary, but not sufficient, spectral change which produces the so-called inverted 'V' event in a color-coded, energy-time spectrogram reported by Frank and Ackerson (1971).

The spectral change associated with the three narrow peaks, 4, 5, and 6, in Figure 3 is not apparent in Figure 4. This change, typical of peak 5, is illustrated in Figure 8 where peak 5 and adjacent background spectra are plotted. As shown, large variations in the differential number flux occur at the extreme low end (<1 kev) of the energy spectrum. This type of spectral change contributes much to the total number flux, little to the total energy flux and significantly decreases the average energy as is apparent in Figure 3. It will become evident from the passes to be discussed that this type of spectral change is a common feature observed equatorward of the prominent energetic electron peaks.

2.2.3 Correlation.

On March 16, 1972, the satellite passed west of the Alaska all-sky camera chain between the times 9:25 and 9:28 UT (∿21:55 MLT). Figure 1 shows the satellite's 110 km field line intercept trajectory relative to the field of view of the all-sky camera chain. Figure 9 is a set of all-sky camera photographs taken at one-minute intervals by the Fort Yukon 35mm camera. By 9:24:37 UT, three weak but clearly defined arcs became visible equatorward of the more active arcs. These three arcs remained stable during the period when the satellite passed through the region of precipitation. On the 9:25:37 and 9:26:37 photographs, six auroral arcs and a bright patch of luminosity can be seen and are labeled in these photographs. The positions of arcs C and D relative to the satellite's 10-second time positions can be read off the 9:26:37 photograph. The crossing of arcs A and B in time occurred about half way between

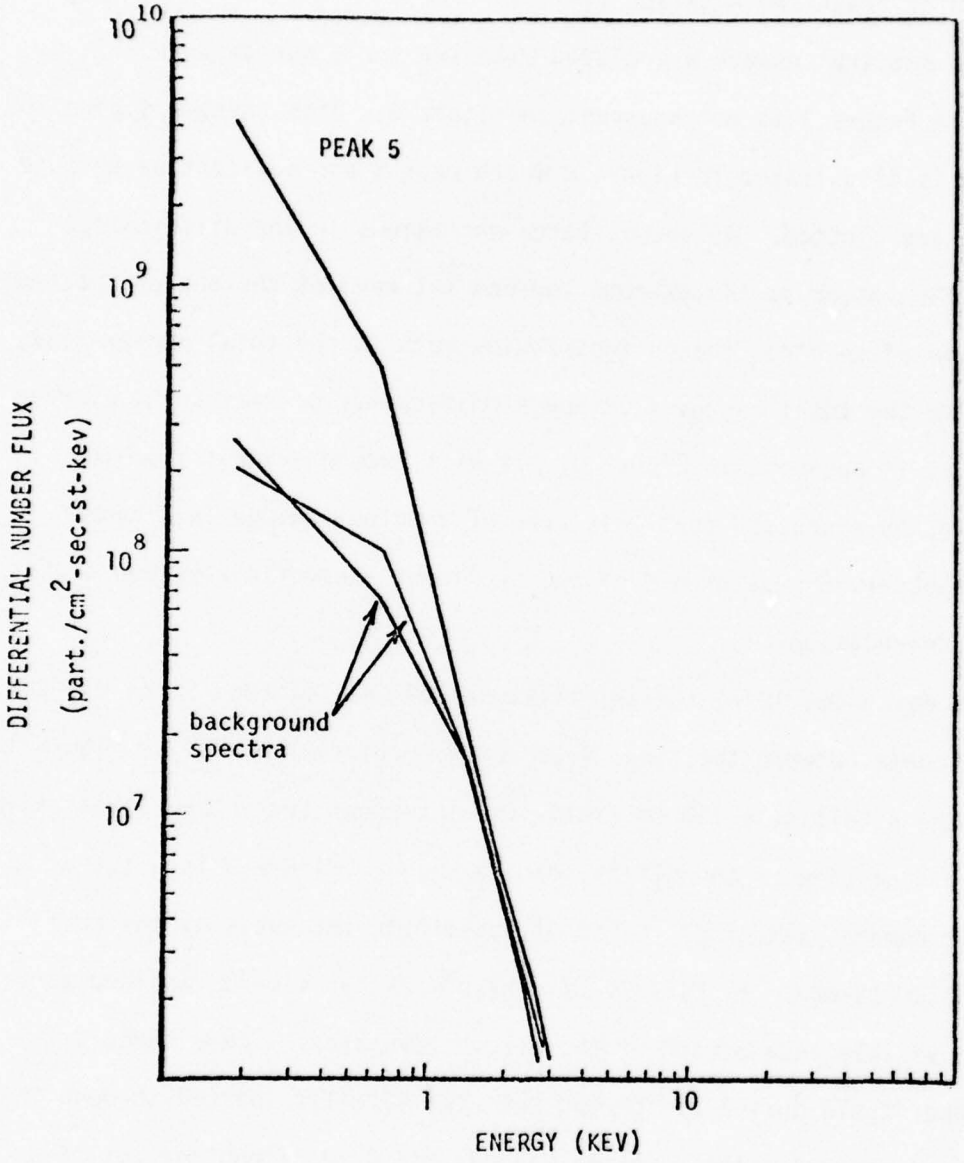

Figure 8

March 16 peak 5 and adjacent background spectra. These spectra illustrate the large increase in the <1 kev differential number flux while the higher energy differential number flux changes little. Usually a small increase in the total energy flux and a moderate to large decrease in the average energy are attributed to this type of spectral change.

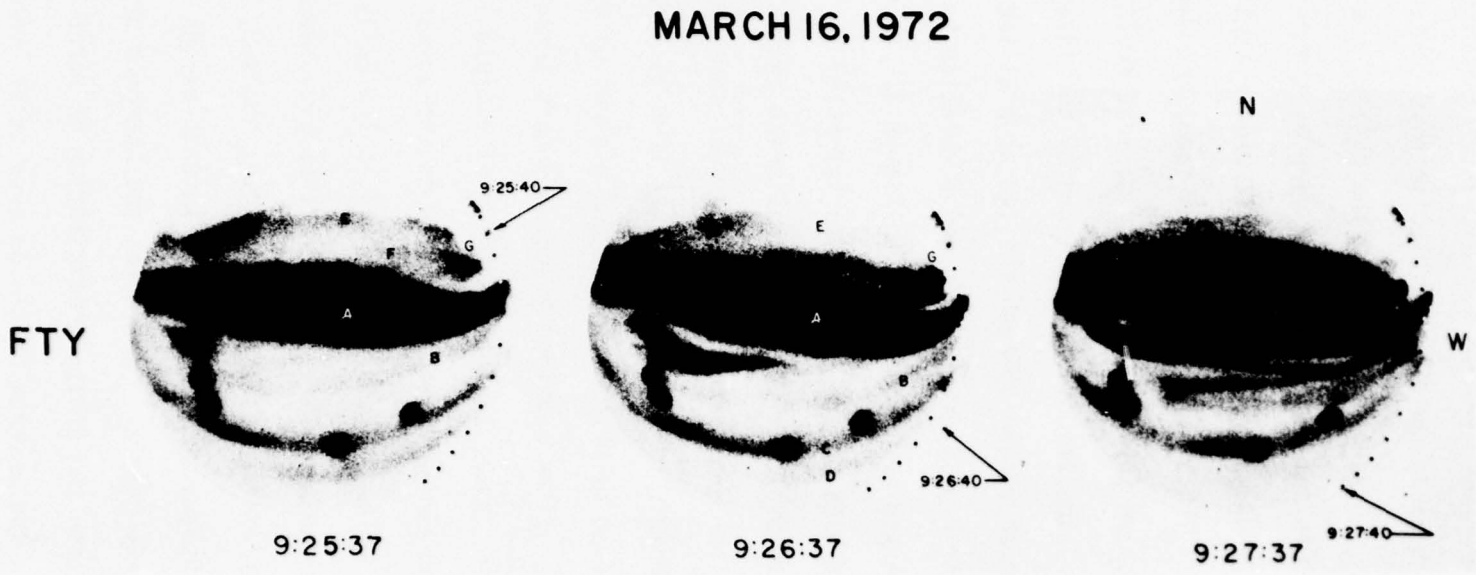

Figure 9

Fort Yukon all-sky camera coverage of the March 16 pass. Auroral arcs A, B, C, and D were traversed by the satellite whose 110 km trajectory is represented by the sequence of dots. The trajectory point which corresponds closest in time to the all-sky photographs is indicated.

all-sky camera frames so either the 9:25:37 or the 9:26:37 frames can be used choosing which ever gives the best result; in this case, the 9:25:37 frame is chosen. Since arc A lies in the zenith, the center of its luminosity rather than the lower border is used as the position of this arc. The satellite did not pass through the precipitation responsible for arcs E and F. These two arcs formed a loop, the end of which terminated near the western horizon (luminosity G) just short of the satellite's trajectory. The brightness is caused by the integration effect of the camera which viewed through the two arcs at the folded end of the loop. The position of arcs A, B, C, and D relative to the satellite's time are marked by small arrows in Figure 3. As shown, the auroral arcs correspond nicely even in relative intensity to the three peaks in the energy flux profile, clearly establishing that these peaks are indeed responsible for producing the auroral arcs observed by the all-sky camera. Equatorward of peak 3 over Ester Dome the particle precipitation was composed of both electrons and protons of comparable total energy flux. Due to the combined effects of both these particle fluxes, it is likely that there existed a region of visible luminosity in the vicinity of Ester Dome. This luminosity is the so-called proton aurora or hydrogen arc which is usually observed in the early evening at or equatorward of discrete auroral arcs. Unfortunately, clouds at Ester Dome prevented the confirmation of this luminosity; however, the luminosity associated with the hydrogen arc is not often intense enough to always be observed by an all-sky camera. Therefore, the hydrogen arc associated with the observed electron and proton precipitation on March 16 may have gone undetected even in the absence of clouds over Ester Dome.

2.2.4 Summary

The March 16 satellite pass crossed the late evening Alaskan auroral zone during a stable but active auroral and magnetic period about one hour prior to an auroral substorm. In both the electron total number and energy flux profiles, three prominent peaks, each of which correlated with an auroral arc, were observed on a background precipitation 5.2°Λ in latitudinal extent with well-defined boundaries at 68.9°Λ and 63.7°Λ. Three significant and different spectral changes associated with the three peaks and some one-second variations in the equatorward background precipitation were observed. These spectral changes, their relative effects on the total number flux, total energy flux, and average energy profiles, and the type of auroral luminosity produced are listed in Table 5. The proton precipitation was comprised of a broad uniform peak which was centered just equatorward of the electron precipitation region and extended 1.2°Λ farther equatorward. The total energy flux of both the proton precipitation and the equatorward end of the electron background precipitation were comparable in magnitude.

2.3 THE APRIL 7 PASS

2.3.1 General magnetic and auroral observations.

Figure 10 shows the April 7 H component magnetic records from stations located at various local magnetic times around the nightside auroral zone. Several hours prior to the satellite pass, there occurred one polar geomagnetic substorm. Both the Fort Churchill and Grate Whale River stations indicate that the onset time of this substorm began no later than 3:50 UT. In response to this substorm, very weak positive bays were recorded in the early evening sector by the two Alaskan

Change in Energy Spectrum	Index No. of Peak	Effects on the Precipitation Latitudinal Profiles						Observed Auroral Form	Comment
		Total no. flux el./(cm^2-sec-st)		Total eng. flux ergs/(cm^2-sec-st)		Average eng. (kev)			
		rel.* change	greatest. value	rel.* change	greatest value	rel.* change	greatest value		
development of a pronounced spectral extremum and a substantial increase in the differential number flux on the high energy side extremum shifts towards higher energies	1	+2.4	9.5E8	+3.3	8.6	+0.8	5.6	bright, active arc	this type of spectral change is observed in all but the March 7 precipitation; the latitudinal extent and the changes in the total energy flux and average energy are larger than for other types of changes in the energy spectrum
with the development of a pronounced spectral extremum, the differential number flux over the entire energy spectrum increases	2	+2.0	9.7E8	+2.4	2.4	+0.2	1.7	homogeneous arc	spectral changes similar to this type observed in all the precipitation data; associated with moderate to large increases in the total energy flux and small to moderate increases in the average energy
	3	+1.3	5.8E8	+1.5	1.7	+0.3	1.8	homogeneous arc	
differential number flux at the low end of the spectral energy range (<1 kev) greatly increases while for higher energies, the diff. no. flux changes little	4	+0.2	2.6E8	+0.1	0.4	-0.1	1.0	no visible auroral luminosity	found equatorward of the prominent electron peaks; associated with decreases in the average energy and small to moderate increases in the total energy flux
	5	+1.0	1.2E9	+0.8	0.5	-0.3	0.3		
	6	+0.5	1.1E8	+0.3	0.06	-0.3	0.3		

*relative change is given as the orders of magnitude difference between the background and the peak value, e.g. rel. change 1.5 implies $x=10^{1.5}y$

†values given in computer exponential notation, e.g. 8.0E9 implies 8.0×10^9

TABLE 5

Summary of the Electron Energy Spectral Changes and Associated Auroral Luminosity for March 16.

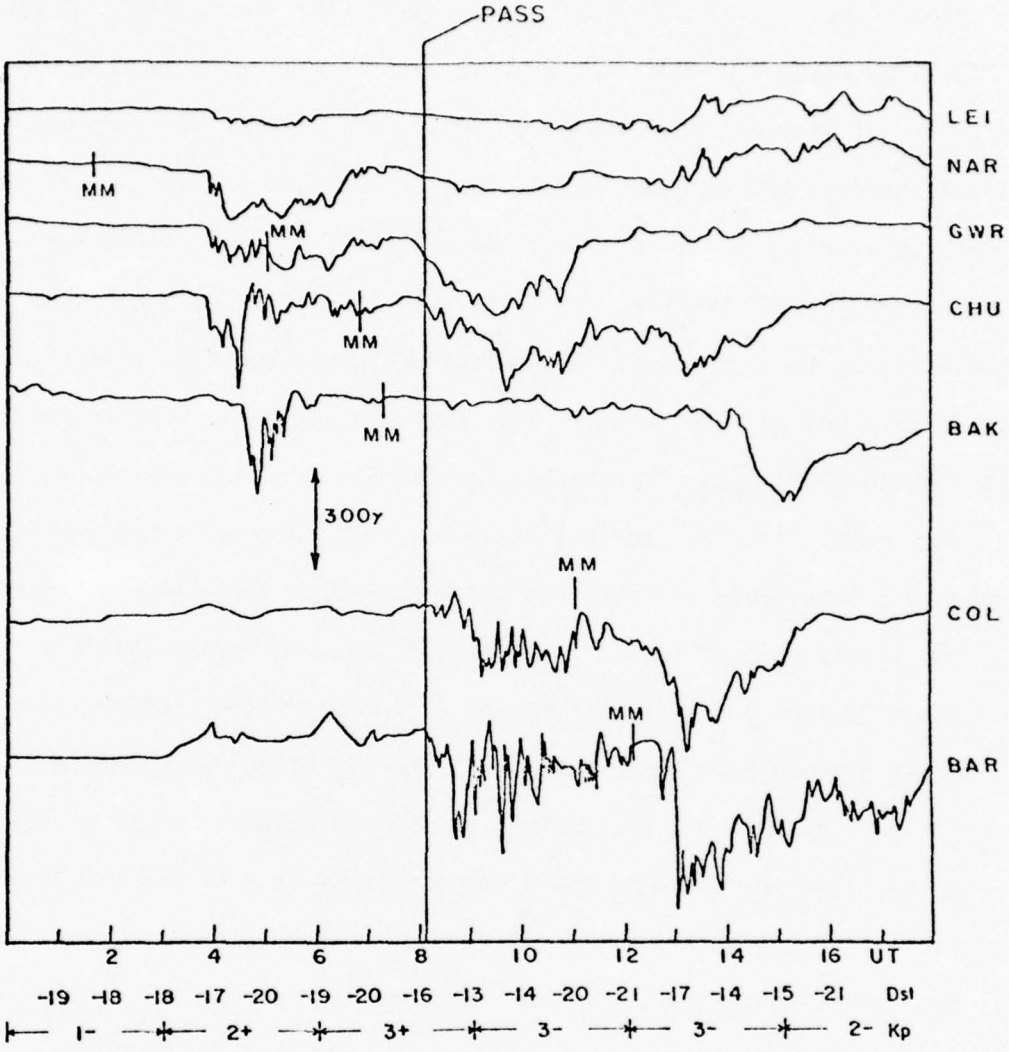

Figure 10

April 7 H-component magnetic records from stations located at various local magnetic times around the night side auroral zone. The M's mark local magnetic midnight at each station, and the vertical line (pass) indicates the time at which the satellite crossed Alaska. These records show that the pass occurred just at the beginning of a magnetic substorm prior to an auroral breakup in Alaska.

stations. By 6:00 UT this substorm was well into its recovery stage. After dusk (7:00 UT) weak intermittent auroral arcs were seen in the vicinity of Inuvik. Equatorward of these arcs at 7:50 UT, a bright stable auroral arc appeared between Inuvik and Fort Yukon. By the time the satellite began its pass (8:07 to 8:08 UT), the intermittent arcs disappeared except for one, and thus, only two visible auroral arcs were traversed by the satellite. As indicated by the Churchill station, the onset of a second more intense polar magnetic substorm in Canada began at about 8:00 UT just prior to the satellite's crossing of the Alaskan auroral zone. However, the stable auroral arc observed between Fort Yukon and Inuvik did not break up until 8:34 UT. The poleward expansion of the second auroral substorm of April 7, reached beyond Inuvik's northern horizon. Diffuse aurora and westward drifting patches were observed between Fort Yukon and Inuvik shortly after the poleward expansion. By 9:15 UT, the diffuse aurora was observed south of College. From this time on, repeated and often extremely intense auroral activations were observed until dawn (12:00 UT). These activations resulted in the several negative bays observed at college during this period. At about 13:00 UT, a third substorm began and recovered by 18:00 UT.

In summary, the satellite crossed two auroral arcs just at the beginning of a magnetic substorm in Canada. The auroral breakup did not reach Alaska until thirty minutes after the satellite pass.

2.3.2 Precipitation.

Figure 11 shows particle precipitation profiles observed by the satellite on April 7. The precipitation extends from a well defined equatorward boundary located at 66.3Λ all the way up to and beyond 78.7Λ. However, the precipitation poleward of 73.8Λ is of such low

energy that for the most part the energy flux and average energy profiles are below the detector thresholds. Therefore, we shall concern ourselves with the region equatorward of 73.8Λ. It is clear from Figure 11 that in both the total number and energy flux profiles three prominent and well separated peaks are evident on a relatively flat background precipitation whose total number flux and total energy flux vary by less than an order of magnitude between 10^7 and 10^8 el/(cm^2-sec-st) and 10^{-2} and 10^{-1} ergs/(cm^2-sec-st) respectively. Note that the total energy flux, latitudinal extent, and average energy of peak 3 is particularly larger than the other two peaks. The background precipitation extends approximately 1.2° equatorward of peak 3 where, like March 16, there exists a broad uniform peak in the proton precipitation which comprises the entire proton precipitation profile and extends approximately 1.2° equatorward of the electron precipitation. The proton peak is broader than the March 16 proton peak but slightly less energetic. The total energy flux of both the proton precipitation and the equatorward end of the background electron precipitation are comparable in magnitude.

The spectral changes across the region of precipitation are illustrated in Figure 12, which shows in time sequence, the spectra that correspond to the one-second data points in Figure 11. Spectra associated with peaks 1, 2, and 3 are labeled. The spectral sequence associated with the two most energetic peaks (2 and 3) exhibit similar spectral changes as observed for the peak 1 spectra in the March 16 precipitation. The development of an extremum with a substantial increase in the differential number flux for energies at or greater than the extremum energy as the

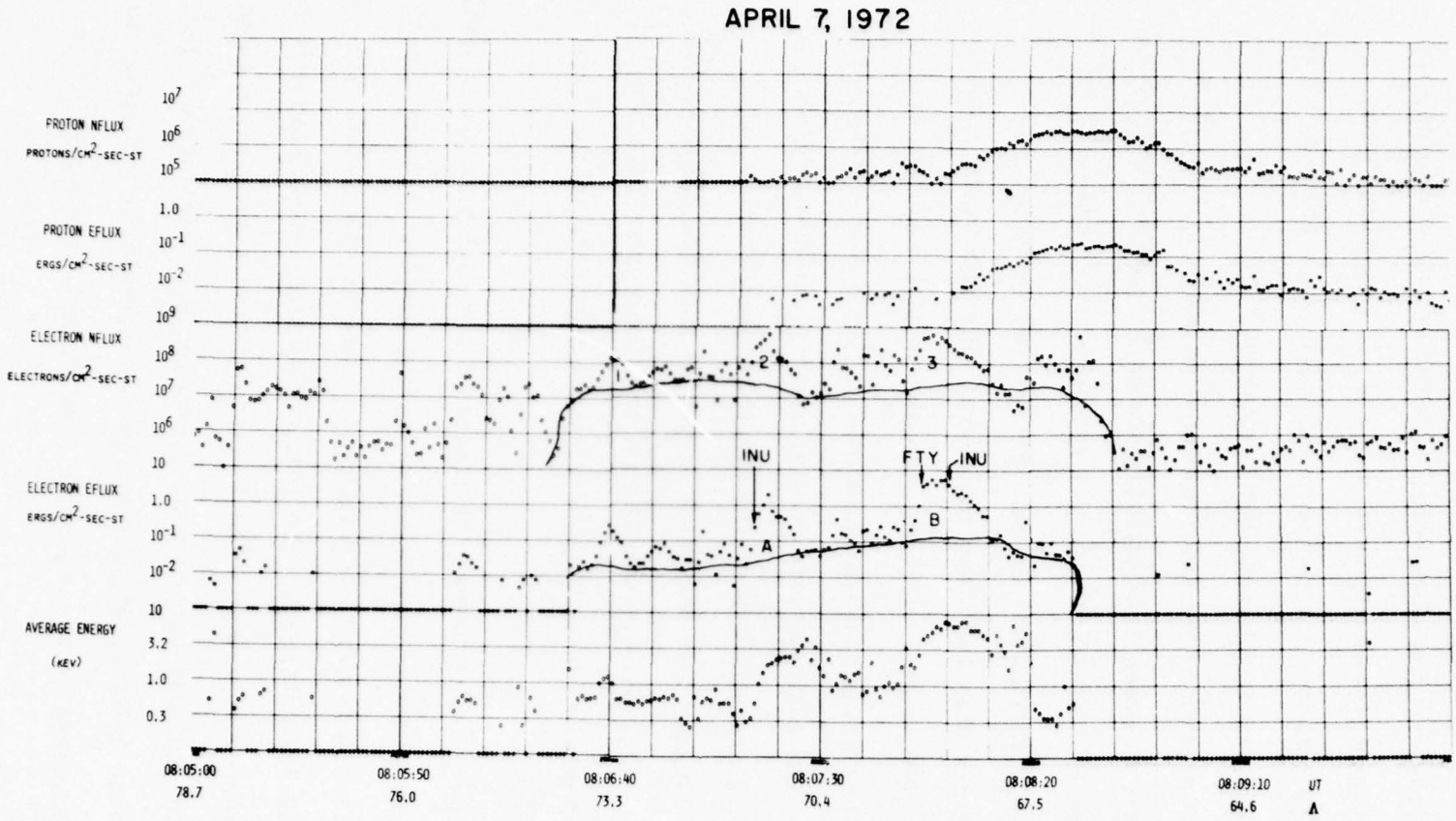

Figure 11

April 7 particle precipitation profiles showing peaks 1 through 3 and the subjectively drawn background precipitation. The letters A and B refer to the auroral arcs in Figure 15 and the arrows indicate the actual positions of these arcs as determined from the indicated all-sky camera stations.

APRIL 7, 1972

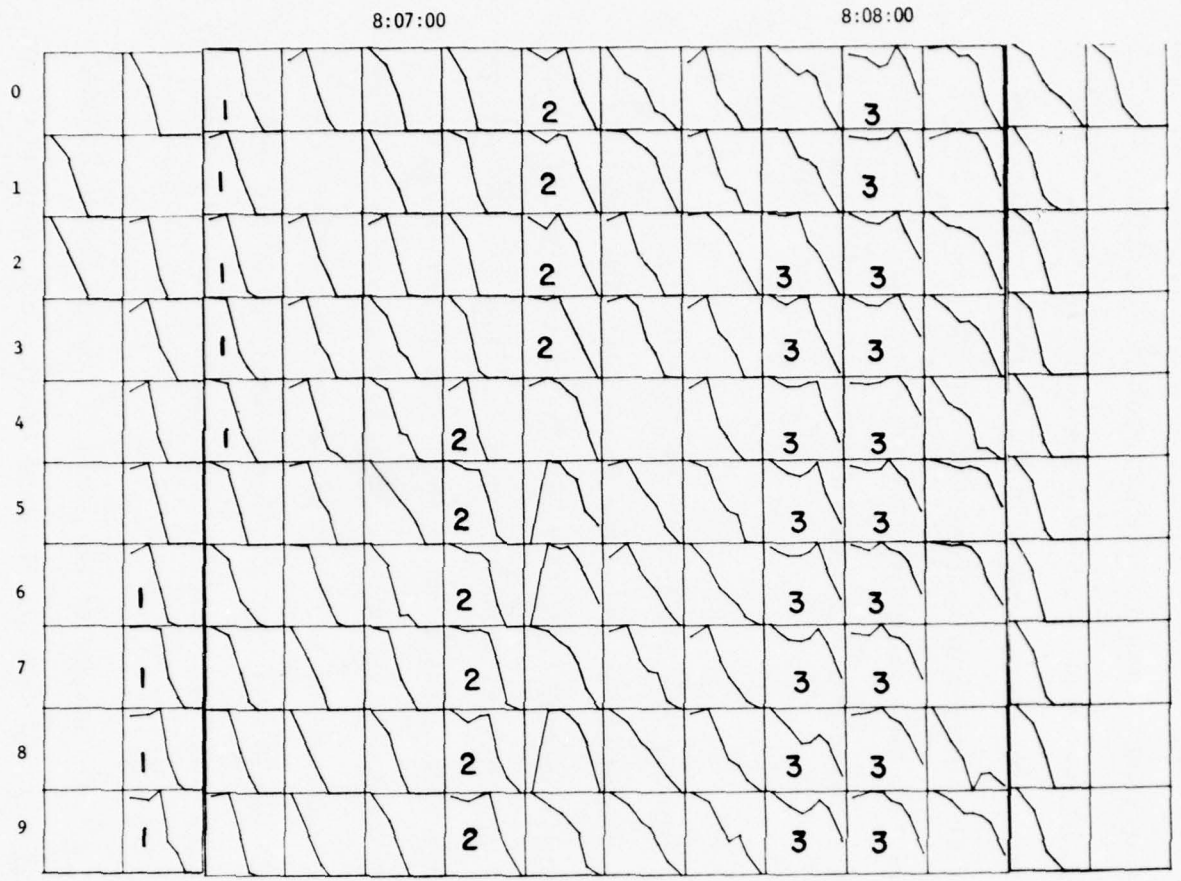

Figure 12

Seven point electron energy spectra associated with each of the one second data points of Figure 11. Time progresses horizontally from left to right in columns of 10 second intervals; each column progresses in time vertically from top to bottom in one second intervals. Spectra associated with the numbered peaks in the flux profiles in Figure 11 are indicated by the appropriate number. Note the well-defined extremum associated with peaks 2 and 3 which seem to grow out of maxwellian and exponential like "background" spectra.

extremum shifts towards higher energies are most evident in the peak 3 spectra which are plotted in Figure 13 for illustration. Again, the large change in both the total energy flux and average energy attributed to this type of spectral change is very apparent in Figure 12. Also from Figure 12, the peak 1 spectra show a spectral development similar to what was observed for peaks 2 and 3 in the March 16 precipitation. The development of a low-energy extremum and the increase in the differential number flux over the entire energy spectrum is illustrated in Figure 14 where selected peak 1 and adjacent background spectra are plotted.

2.3.3 Correlation.

On April 7 between 8:06 and 8:09 UT (22:20 MLT), the satellite passed nearly overhead at Fort Yukon and Ester Dome. The satellite's 110 km field line intercept trajectory relative to the field of view of the Alaskan all-sky chain is shown in Figure 1. Figure 15 shows a set of all-sky camera photographs taken at one-minute intervals by the Inuvik and Fort Yukon all-sky cameras. From this set of all-sky photographs, it is clear that the satellite passed over one auroral arc. With the aid of a movie projector, another auroral arc or arc segment can be seen moving equatorward and is indicated in Figure 14. These two arcs are labeled A and B.

Arc A is just on the edge of the field of view of the Fort Yukon photograph, and thus, is only visible from Inuvik. The position of arc A relative to satellite time is determined from the 8:07 Inuvik photograph. The position of arc B relative to satellite time can be determined from both the Fort Yukon and Inuvik 8:08 photographs. However, the 8:09 Fort Yukon photograph gives much better results. Assuming the Fort Yukon camera is out of synchronization by one minute, the 8:09 Fort

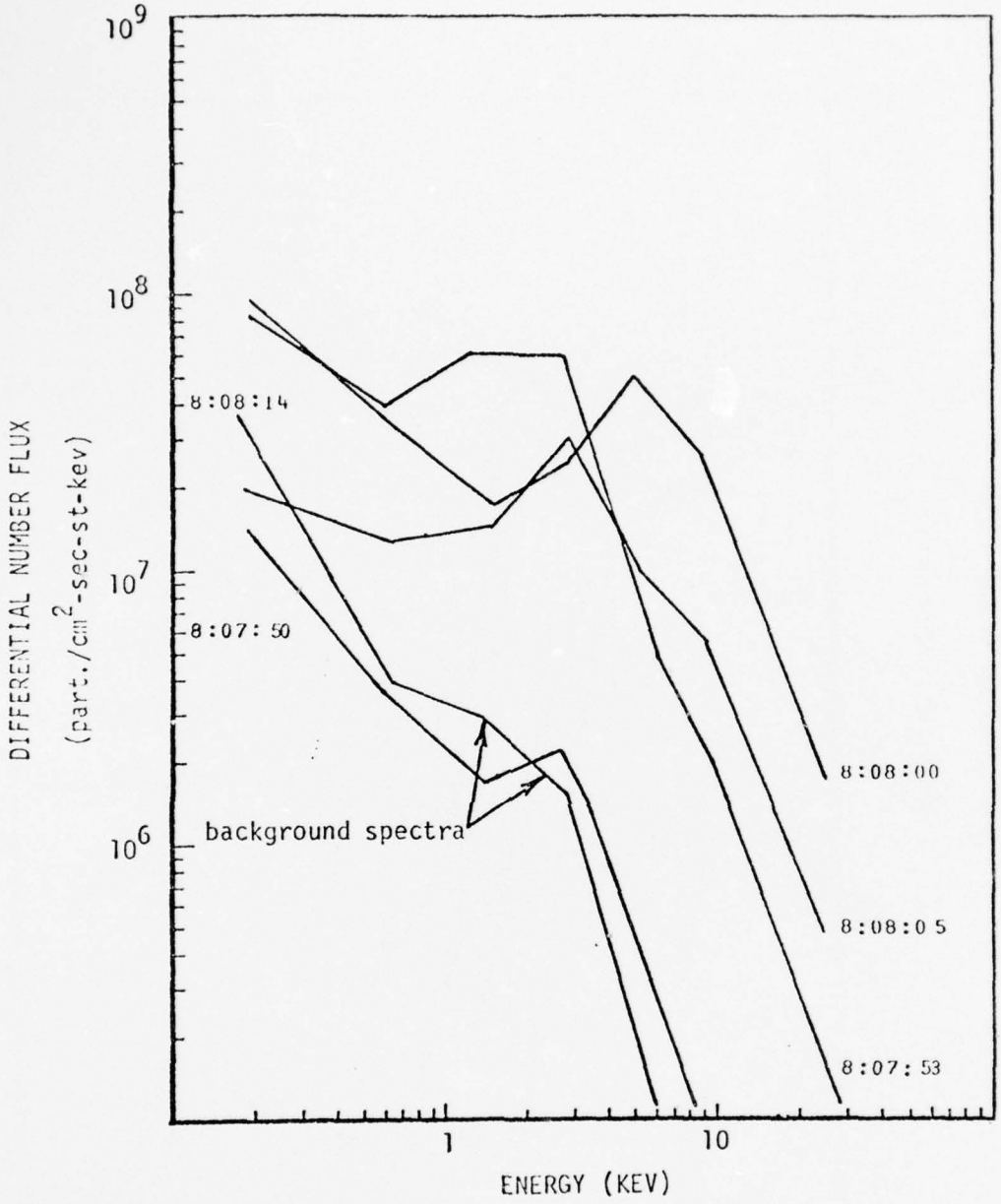

Figure 13

April 7 selected peak 3 and adjacent background spectra. These spectra illustrate the development of a spectral extremum with an increase in the differential number flux on the high energy side of the extremum as the extremum shifts towards higher energies. A large increase in both the total energy flux and average energy profiles is attributed to this type of spectral change.

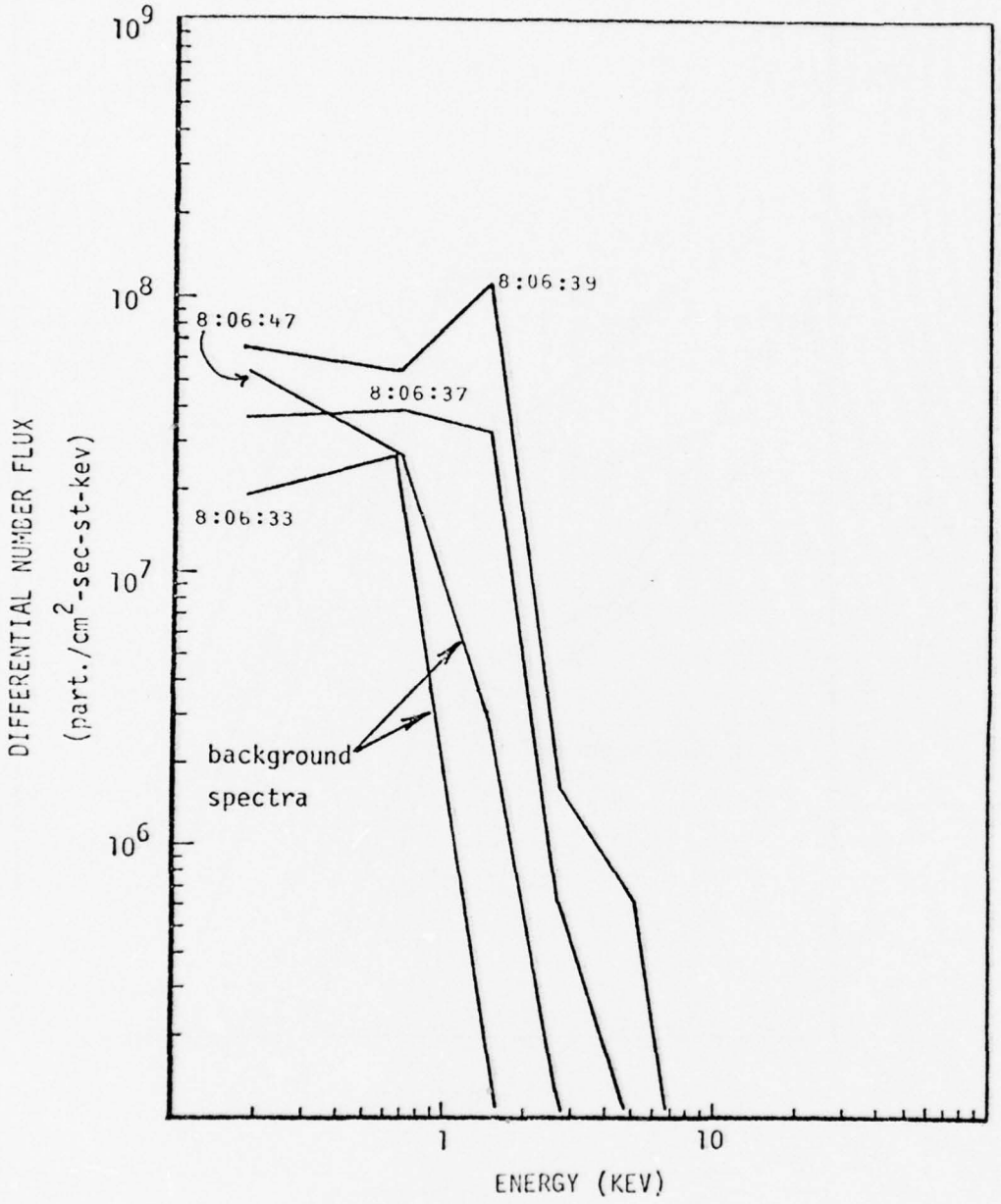

Figure 14

April 7 selected peak 1 and adjacent background spectra. These spectra illustrate the development of a spectral extremum with an increase in the differential number flux over most of the energy spectrum. A moderate to large increase in the total energy flux and a small increase in the average energy are attributed to this type of spectral change.

APRIL 7, 1972

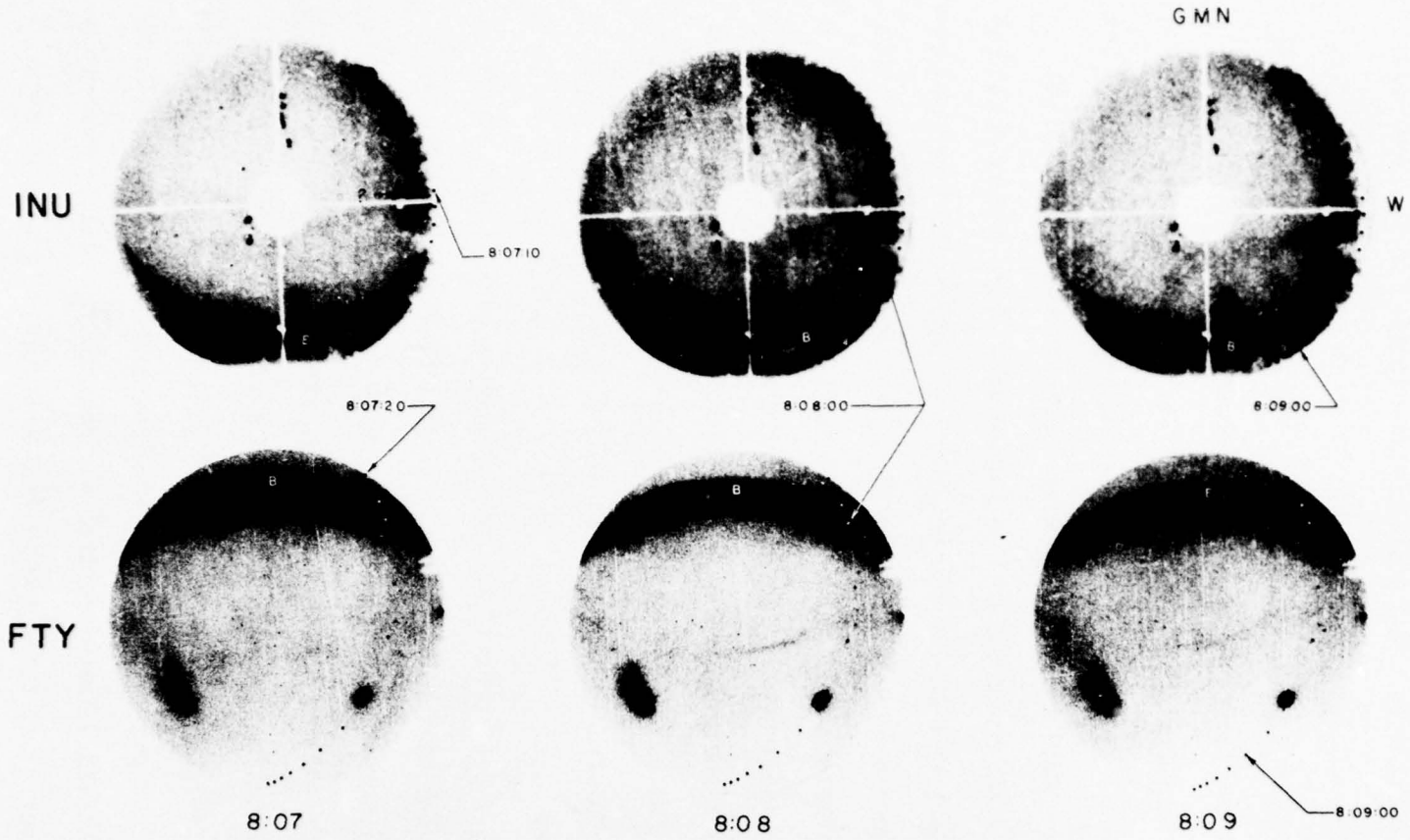

Figure 15

Inuvik and Fort Yukon all-sky camera coverage of the April 7 pass. Auroral arcs A and B were traversed by the satellite whose 110 km trajectory is represented by the sequence of dots. The trajectory point which corresponds closest in time to the all-sky photographs is indicated.

Yukon photograph is used. The position of both arcs in the precipitation profiles as determined from each of the appropriate photographs is indicated by the arrows in Figure 11. The arc positions determined from both stations correspond remarkably close and even in relative intensity to the two peaks in the energy flux profiles, thus establishing that peaks 2 and 3 are responsible for producing the auroral arcs A and B respectively. Note that several minor peaks in the precipitation between peaks 1 and 3 are evident in Figure 11. It is likely that they are the subvisual remnants of the several weak intermittent arcs observed poleward of the stable bright arc (peak 3) just prior to the satellite pass. The luminosity produced by the combined effects of the proton and electron precipitation equatorward of peak 3 is subvisible as well as the luminosity associated with the precipitation between peaks 2 and 3 and 1 and 2. The luminosity produced by all these precipitation subregions are certainly observable with more sensitive optical devices.

2.3.4. Summary

The April 7 pass crossed the late evening Alaskan auroral zone approximately one half hour before an auroral breakup. In both the electron total number and energy flux profiles, three prominent peaks, two of which correlated with auroral arcs, were observed on a flat background precipitation which was confined within a 7.6°Λ latitudinal region with a well-defined equatorward boundary at 66.3°Λ. Two significant and different changes in the energy spectrum associated with the three peaks were observed. These spectral changes, their relative effects on the total number flux, total energy flux and average energy profiles, and the type of auroral luminosity produced are listed in Table 6. The

proton precipitation comprised of a broad uniform peak which was located just at the equatorward edge of the electron precipitation region and extending 1.2° equatorward. The total energy flux of both the proton precipitation and the equatorward background electron precipitation were comparable.

2.4 THE MARCH 14 PASS

2.4.1 General magnetic and auroral observations.

Figure 16 shows the March 14 H-component magnetic records from the indicated Alaskan and Canadian stations. Because of the low K_p values which prevailed on March 14, this day was classified as one of the five quietest days of the month. The low K_p values indicate that the substorms which occurred on March 14 did so along a contracted oval. The listed Dst values show that several hours before and after the satellite pass no world-wide geomagnetic activity was in progress, although the first few Dst values reveal the final recovery of a geomagnetic storm which began seven days earlier.

Prior to the satellite pass, there occurred two polar geomagnetic substorms. Both the Fort Churchill and Great Whale River stations show that the first onset time occurred no later than 6:00 UT. As shown by the Barrow and College stations, there was virtually no early evening magnetic disturbance recorded by these two Alaskan stations. After dusk and until 6:50 UT, no aurora was observed in Alaska. Between 6:50 and 8:09 UT, a weak arc was observed just north of Fort Yukon. This arc brightened by 8:10 UT, and a westward traveling surge passed along the arc two minutes later. The sudden commencement of a weak negative bay recorded just after 8:00 UT by the Barrow station together with the

Change in Energy Spectrum	Index No. of Peak	Effects on the Precipitation Latitudinal Profiles						Observed Auroral Form	Comment
		Total no. flux el./(cm^2-sec-st)		Total eng. flux ergs/(cm^2-sec-st)		Average eng. (kev)			
		rel.* change	greatest† value	rel.* change	greatest value	rel.* change	greatest value		
development of a pronounced spectral extremum and a substantial increase in the differential number flux on the high energy side of the extremum as the higher energies	2	+1.2	6.4E8	+1.8	2.0	+0.8	1.9	homogeneous arc	this type of spectral change is observed in all but the March 7 precipitation; the latitudinal extent and the changes in the total energy flux and average energy arc larger than for other types of changes in the energy spectrum
	3	+1.8	6.3E8	+1.7	5.5	+0.7	5.5		
with the development of a pronounced spectral extremum, the differential number flux over the entire energy spectrum increases	1	+0.9	1.4E8	+1.2	0.3	+0.3	1.2	no visible *luminosity*	spectral changes similar to this type observed in all the precipitation data; associated with moderate to large increases in the total energy flux and small to moderate increases in the average energy

*relative change is given as the orders of magnitude difference between the background and the peak value, e.g. rel. change 1.5 implies $x=10^{1.5}y$

†values given in computer exponential notation, e.g. 8.0E9 implies 8.0×10^{9}

TAFLE 6

Summary of the Electron Energy Spectral Changes and Associated Auroral Luminosity for April 7.

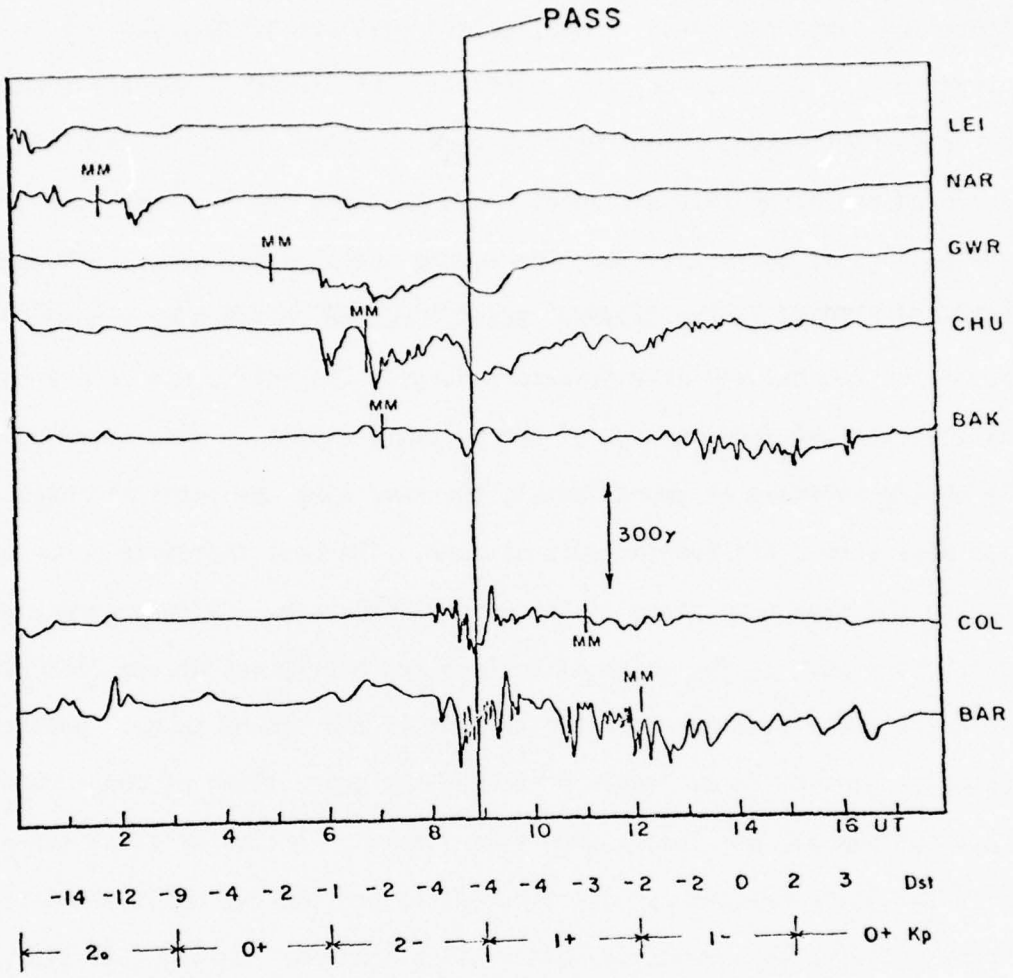

Figure 16

March 14 H-component magnetic records from stations located at various local magnetic times around the night side auroral zone. The M's mark local magnetic midnight at each station, and the vertical line (pass) indicates the time at which the satellite crossed Alaska. These records show that the pass occurred during the expansive phase of a magnetic substorm.

indented bay recorded at College, marks the passage of this westward traveling surge far north of College and south of Barrow, and the occurrence of a third very weak substorm. At 8:20 UT a new arc formed north of Fort Yukon, brightened and then a second westward traveling surge passed along this arc about 1 minute later and 15 minutes prior to the passage of the satellite. The second indented bay observed between 8:24 and 8:30 UT in the College magnetic record followed by a negative bay marks the passage of this second surge. The active discrete arcs delineating the leading edge of the poleward expansion were observed to be moving poleward at approximately the same time the satellite began its pass across the evening auroral zone. The pass therefore occurred during the expansive phase of the auroral substorm. Diffuse aurora was observed almost as far south as College and nearly out of the Fort Yukon northern field of view after the passage of the second surge. Unfortunately, ground fog at Inuvik prevented the observation of the northern limit of the diffuse aurora from this station. Active discrete aurora with two intensifications was observed through the fog until 12:00 UT after which no aurora was visible at this station. During this time, the poleward edge of the diffuse aurora eroded all the way back to the College northern horizon. After 10:00 UT no other aurora was visible either from Fort Yukon or Ester Dome. Finally, a fifth weak substorm began at 12:00 UT. After recovery, quiet conditions prevailed for the remainder of the period.

In summary, the Lockheed instrumented satellite crossed the Alaskan auroral oval during the expansive phase of an auroral substorm. The satellite passed through particle precipitation responsible for the production of both discrete aurora and a broad region of diffuse aurora.

2.4.2 Precipitation

Figure 17 shows the particle precipitation profiles observed on March 14. As shown, two very intense and energetic peaks in both the electron total number and energy flux profiles are discernible on the very poleward end of a broad and flat background precipitation 10.2° in latitudinal extent with well-defined boundaries at 74.0°Λ and 63.8°Λ. The two peaks labeled 1 and 2 and a subjectively drawn background precipitation are indicated in Figure 17. Peaks 1 and 2 exceeded the 10^9 part/(cm^2-sec-st) computer plotting threshold and their maximum total number flux intensities are 1.1×10^{10} and 1.5×10^9 electron/(cm^2-sec-st) respectively. The total energy flux associated with peaks 1 and 2 also exceeded the 10 ergs/(cm^2-sec-st) printout threshold and their maximum values are 33.5 and 51.9 ergs/(cm^2-sec-st) respectively. Compared to 1, peak 2 is more energetic, broader in latitudinal extent, and of a particularly larger average energy--an unusually high 22 kev. However, peak 1 is almost an order of magnitude more intenss in number flux.

Of particular interest is the uniformity of the background precipitation equatorward of peaks 1 and 2 and the latitudinal extent to which it is void of prominent peaks. In Figure 17, the total number and energy flux and average energy of the background precipitation is shown to increase to approximately 10^8 el./(cm^2-sec-st), 1 erg/(cm^2-sec-st), and 8 kev respectively and remain virtually unchanged at these values for a latitudinal extent of 5° before decreasing to threshold. Also note that the total energy flux of the background precipitation exceeds by more than an order of magnitude that which was observed prior to a

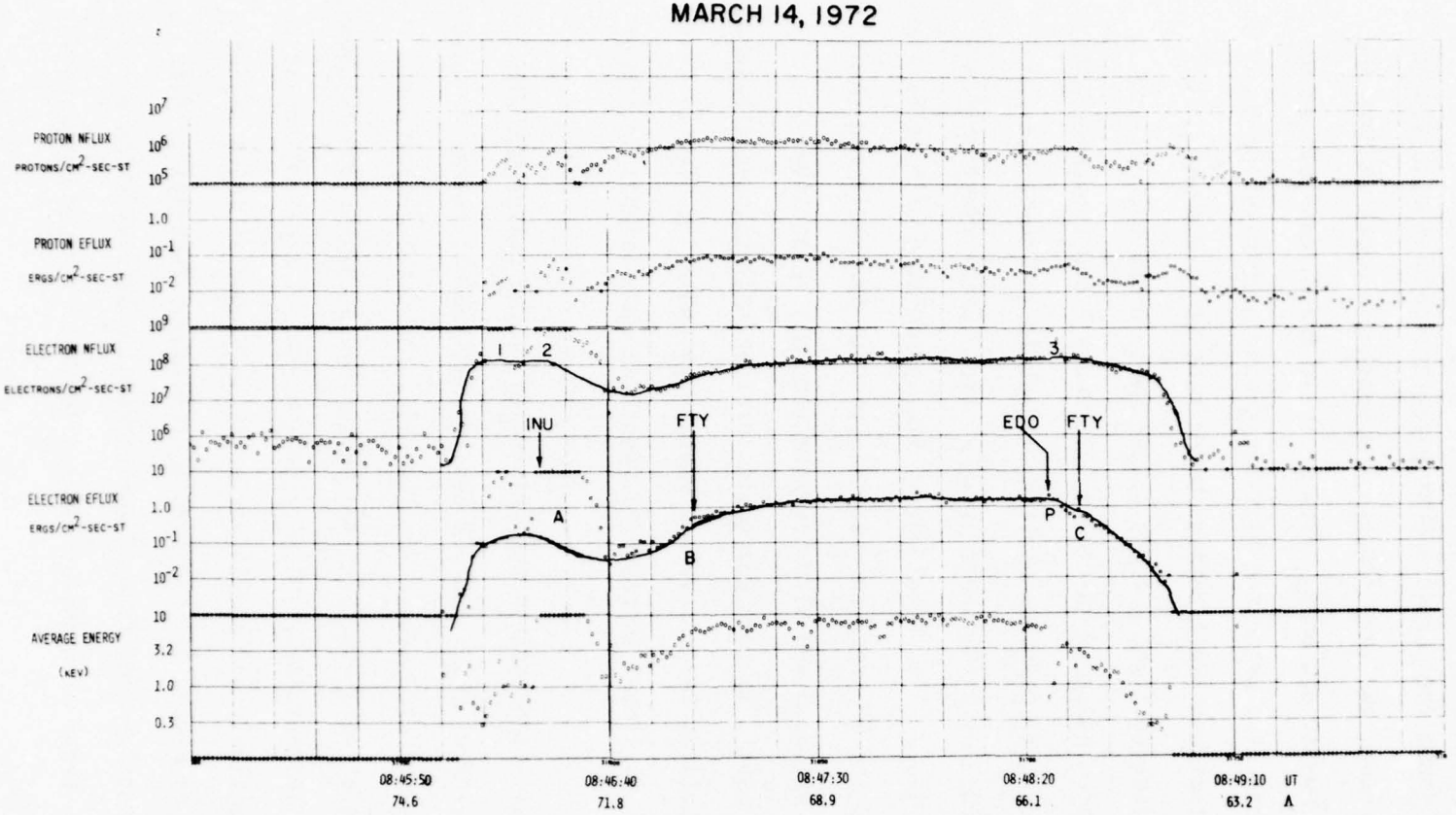

Figure 17

March 14 particle precipitation profiles showing peaks 1 through 3 and subjectively drawn background precipitation. The letters A, B, C, and P refer to the auroral arc, the edges of the diffuse aurora and the one patch shown in Figure 23. The arrows indicate the actual position of these auroral forms as determined from the indicated all-sky camera stations.

substorm on March 16 and April 7. At the equatorward end of the background precipitation, there sets a single narrow and very intense peak in the total number flux but with a much less prominent corresponding peak in the total energy flux profile. This peak is labeled 3 in Figure 17. It also exceeded the total number flux printout threshold and its maximum is 1.9×10^9 electron/(cm^2-sec-st). Peak 3 as well as some of the lesser peaks in the uniform region correspond to decreases in the average energy, which as we have seen in the March 16 profiles indicates a differential number flux heavily weighted towards low energies (<1 kev).

The proton precipitation is spread throughout the electron precipitation and is uniform and flat over most of its latitudinal extent. Note that the proton precipitation is approximately an order of magnitude less intense and energetic than of the proton peaks observed prior to an auroral breakup.

The sequence of spectra associated with peaks 1, 2, and 3 and the broad uniform precipitation equatorward are shown in Figure 18. Of all the spectra, only the spectra associated with peak 2 exhibit an extremum. In Figure 19, selected peak 2 spectra are plotted to show the same spectral development associated with very large changes in both the total energy flux and the average energy as observed on March 16 and April 7. Spectra associated with peak 1 are plotted in Figure 20. The large enhancement of the differential number flux over the entire energy spectrum (somewhat biased in favor of the 1 to 10 kev energy interval) results in a relatively large increase in the total energy flux in comparison to the average energy. Peak 3 and the adjacent spectra are

MARCH 14, 1972

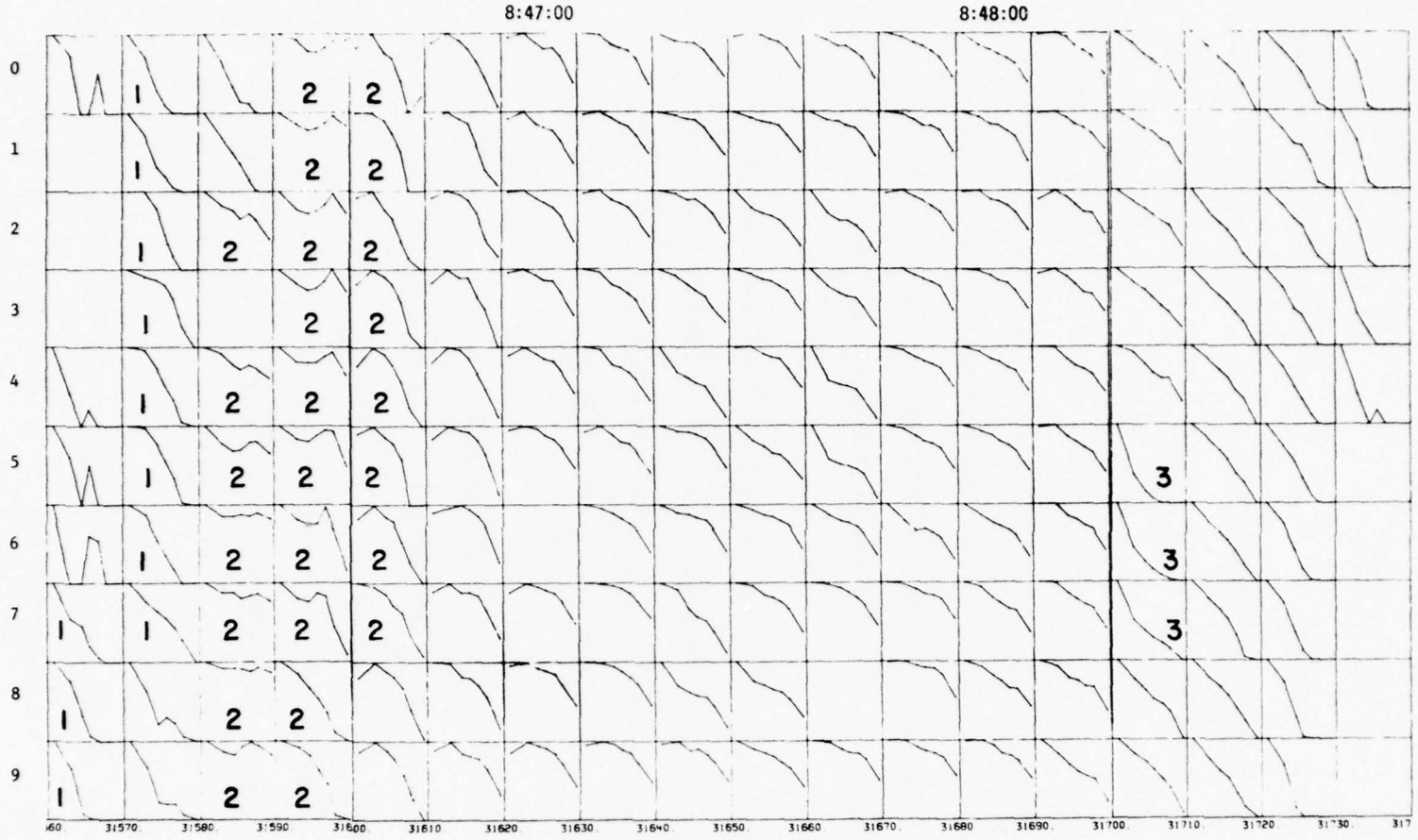

Figure 18

Seven point electron energy spectra associated with each of the one second data points in Figure 17. Time progresses horizontally from left to right in columns of 10 seconds; each column progresses in time vertically from top to bottom in one second intervals. Spectra associated with the numbered peaks in the flux profiles in Figure 17 are indicated by the appropriate number. Note the well-defined extremum associated with peak 2 which seem to grow out of maxwellian and exponential-like "background" spectra.

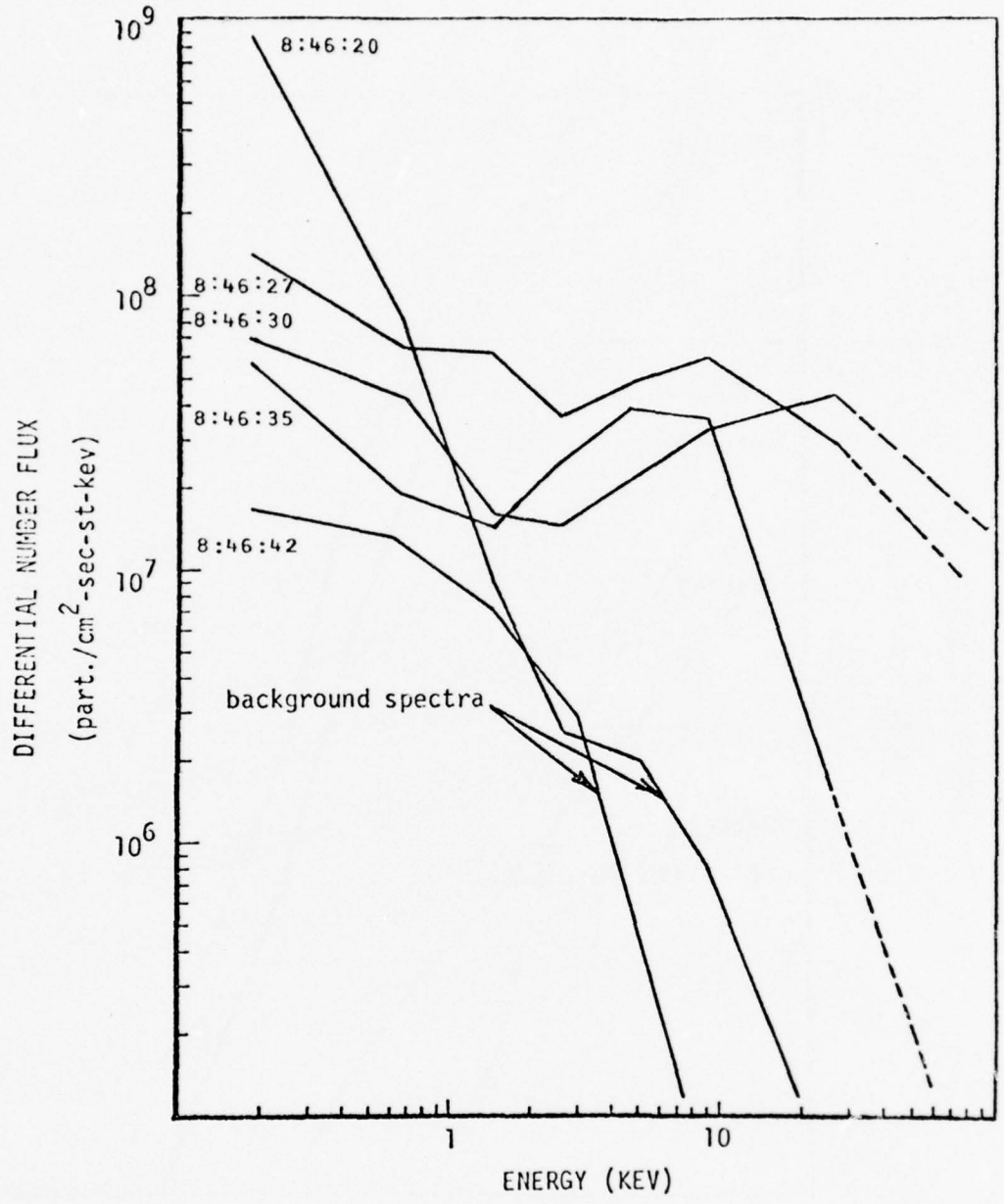

Figure 19

March 14 selected peak 2 and adjacent background spectra. These spectra illustrate the development of a spectral extremum with an increase in the differential number flux on the high energy side of the extremum as the extremum shifts towards higher energies. A large increase in both the total energy flux and average energy is attributed to this type of spectral change.

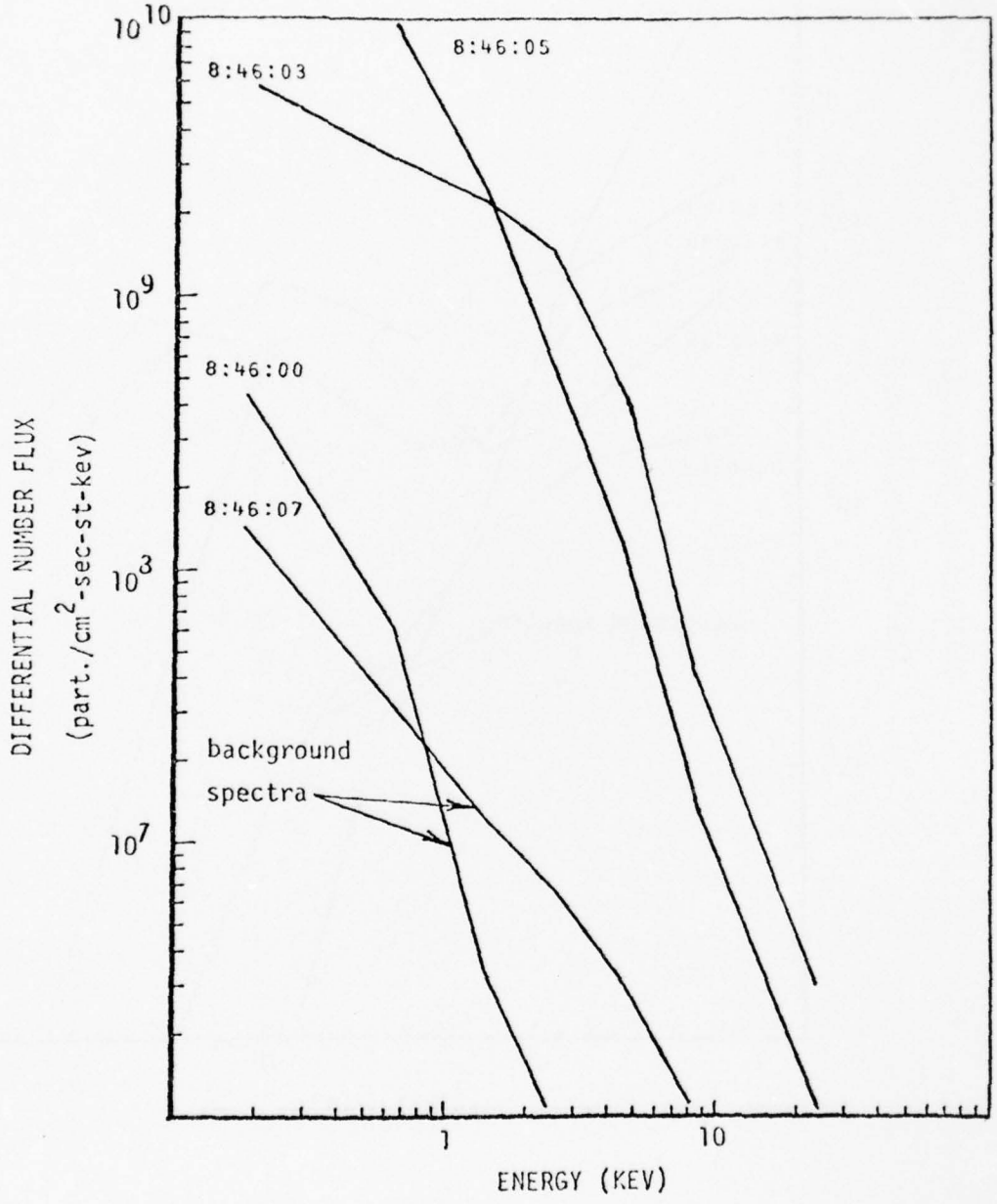

Figure 20

March 14 selected peak 1 and adjacent background spectra. These spectra illustrate the increase in the differential number flux over the entire energy spectrum. A moderate to large increase in the total energy flux and a small increase in the average energy are attributed to this type of spectral change.

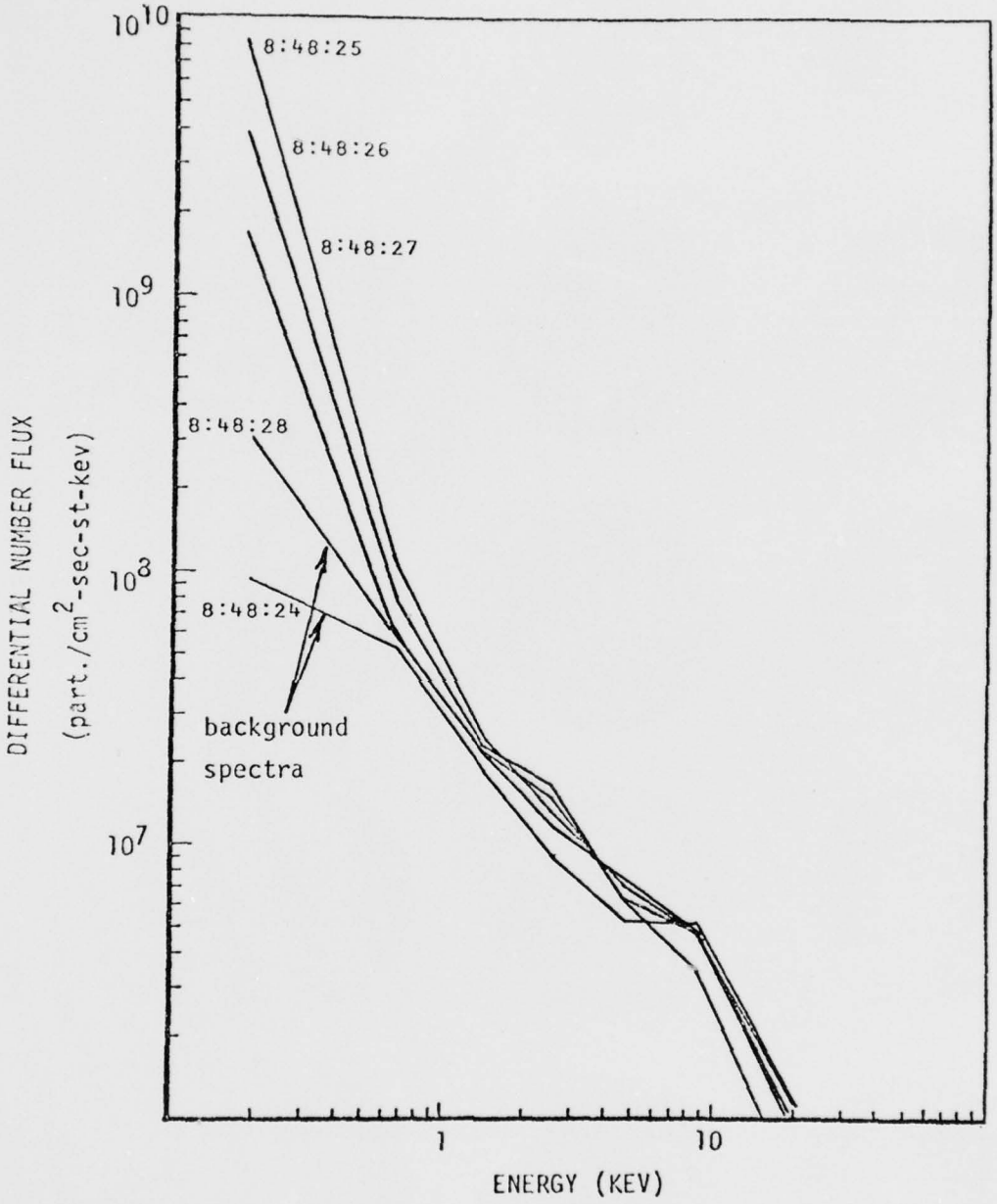

Figure 21

March 14 peak 3 and adjacent background spectra. These spectra show the large increase in the <1 kev differential number flux while the higher energy differential number flux changes little. A small to moderate increase in the total energy flux and moderate to large decrease in the average energy are attributed to this type of spectral change.

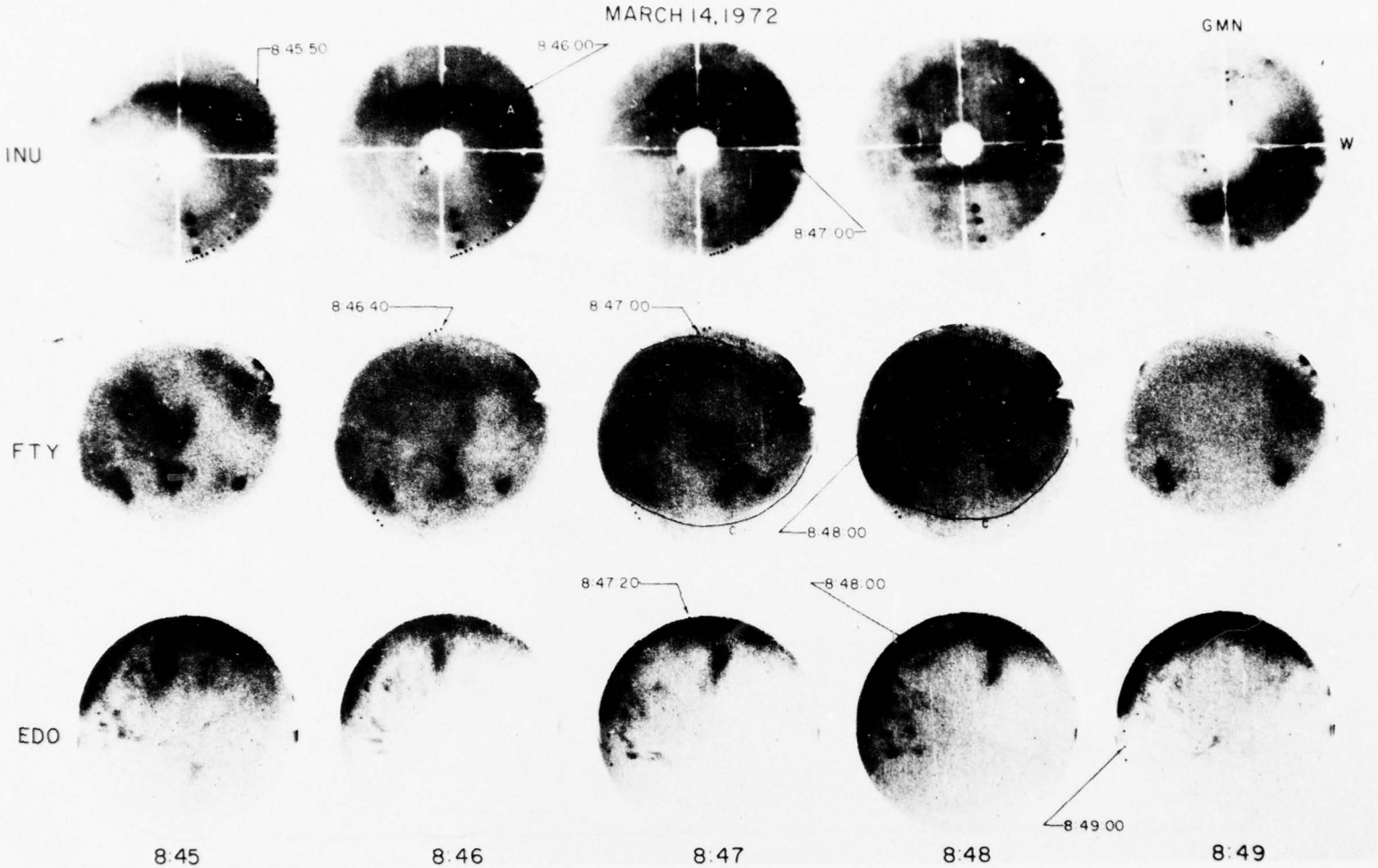

Figure 22

Inuvik, Fort Yukon, and Ester Dome all-sky camera coverage of the March 14 pass. Auroral arc A and the edges of the broad region of diffuse aurora B and C were traversed by the satellite whose 110 km trajectory is represented by the sequence of dots. The trajectory point which corresponds closest in time to the all-sky photograph is indicated.

plotted in Figure 21. It is clear from this figure that these spectra are all nearly identical except for the enhanced low energy differential number flux of the peak 3 spectra which contributes significantly to the total number flux, but little to the energy flux and substantially decreases the average energy as shown in Figure 17.

2.4.3 Correlation

On March 14, the satellite passed east of the Alaska all-sky camera chain between the times 8:46 to 8:49 UT (∿21:30 MLT). Figure 1 shows the satellite's 110 km field line intercept trajectory relative to the field of view of the all-sky camera stations. Intermittent ground fog at Inuvik obscured the aurora during the satellite pass, but a quantitative correlation with the satellite precipitation data can be made. Figure 22 is a set of all-sky camera photographs taken at one-minute intervals by the Inuvik, Fort Yukon, and Ester Dome stations.

One auroral arc is visible on the 8:46 Inuvik photograph and labeled A. A latitudinally broad uniform diffuse luminosity is visible in the Fort Yukon photographs. Note that both the poleward and equatorward edges of the diffuse aurora are barely visible and labeled B and C on these photographs. If it were not for ground fog at Inuvik, a gap in the luminosity between the poleward edge of the diffuse aurorae and auroral arc A could be seen from this station. The equatorward edge of the diffuse aurora and several discrete patches or rayed auroral forms are clearly seen on the Ester Dome photographs. The satellite's 110 km trajectory passes in the near vicinity of one of these patches labeled P on the 8:48 EDO photograph. The position of arc A is determined from the 8:46 Inuvik photograph, the boundaries of the diffuse aurora B and C

are determined form the 8:47 and 8:48 Fort Yukon photographs respectively, and the equatorward boundary of the diffuse auroral region and the 110 km trajectory point closest to patch P are determined from the 8:48 Ester Dome photograph. These positions are marked by the arrows in Figure 17. Peaks 1 and 2 correspond nicely with auroral arc A. If it were not for ground fog at Inuvik, arc A would probably be seen as two arcs corresponding to peaks 1 and 2. The edges of the broad visible diffuse region correspond to where the total energy flux begins to decrease below the 1 erg/(cm^2-sec-st) level. It will be established in Chapter 3 that a total energy flux approximately equal to or greater than 0.3 or 0.4 erg/(cm^2-sec-st) produces luminosity detectable by the 35mm all-sky cameras used along the Alaskan chain. The trajectory's closest approach to the patch labeled P corresponds nicely with peak 3 in the precipitation profiles. It is likely that the satellite traversed the very outside edge of the precipitation which caused this visible patch.

2.4.4 Summary

The March 14 satellite pass crossed the late evening Alaskan auroral zone during the expansive phase of an auroral substorm. Two intense and energetic peaks which correlated with at least one auroral arc were observed on the poleward end of a background precipitation 10.2° in latitudinal extent with well-defined boundaries at 66.3°Λ and 78.7°Λ. Equatorward of the two energetic peaks, the background precipitation extended for a considerable distance void of any prominent peaks and produced a broad region of visible diffuse aurora. A third intense but

Change in Energy Spectrum	Index No. of Peak	Effects on the Precipitation Latitudinal Profiles						Observed Auroral Form	Comment
		Total no. flux el./(cm^2-sec-st)		Total eng. flux ergs/(cm^2-sec-st)		Average eng. (kev)			
		rel.* change	greatest† value	rel.* change	greatest value	rel.* change	greatest value		
development of a pronounced spectral extremum and a substantial increase in the differential number flux the high energy side of the extremum as the extremum shifts towards higher energies	2	+2.2	1.5E9	+2.7	51.9	+1.3	21.2	active arc	this type of spectral change is observed in all but the March 7 precipitation; the latitudinal extent and the changes in the total energy flux and average energy are larger than for other types of changes in the energy spectrum
diff. no. flux over the entire energy spectrum increases	1	+3.6	1.1E10	+2.5	33.5	+0.4	2.3	not observed	spectral changes similar to this type observed in all the precipitation data; associated with moderate to large increases in the total energy flux and small to moderate increases in the average energy
differential number flux at the low end of the spectral energy range (<1 kev) greatly increases while for higher energies, the diff. no. flux changes little	3	+1.1	1.9E9	+0.2	2.0	-1.0	0.7	auroral patch in the diffuse aurora	found equatorward of the prominent electron peaks; associated with decreases in the average energy and small to moderate increases in the total energy flux

*relative change is given as the orders of magnitude difference between the background and the peak value, e.g. rel. change 1.5 implies $x=10^{1.5}y$

†values given in computer exponential notation, e.g. 8.0E9 implies 8.0×10^9

TABLE 7

Summary of the Energy Spectral Changes and Associated Auroral Luminosity for March 14.

weakly energetic peak on the equatorward end of the background precipitation was also observed and correlated with an auroral patch in the diffuse aurora. Three significant and different spectral changes were observed associated with the three peaks in the electron precipitation. These spectral changes, their relative effects on the total number flux, total energy flux, and average energy profiles, and the type of auroral luminosity produced are listed in Table 7. Equatorward of two peaks in the electron total energy flux profile there exist a uniform and broad region of precipitation approximately 600 km in latitudinal extent. The proton precipitation extended the full length of the electron precipitation and remained uniform over most of this region. Over most of the electron precipitation region, the total proton energy flux was approximately an order of magnitude less than the total electron energy flux.

2.5 THE MARCH 9 PASS

2.5.1 General magnetic and auroral observations.

Figure 23 shows the March 9 H-component magnetic records from the indicated stations. The Dst values show that this day began with the main phase decrease of a weak geomagnetic storm. From the Fort Churchill and Great Whale River magnetograms, at least one substorm occurred prior to the satellite pass, beginning no later than 5:30 UT and recovering by 7:00 UT. There was no early-evening magnetic disturbance observed by the Alaskan stations. During this quiet period, auroral arcs at or north of Inuvik were observed. After 7:00 UT, the arcs became very active, probably due to the substorm seen at Fort Churchill and Great Whale River between 6 and 7 UT. By 8:40 UT, an auroral substorm began;

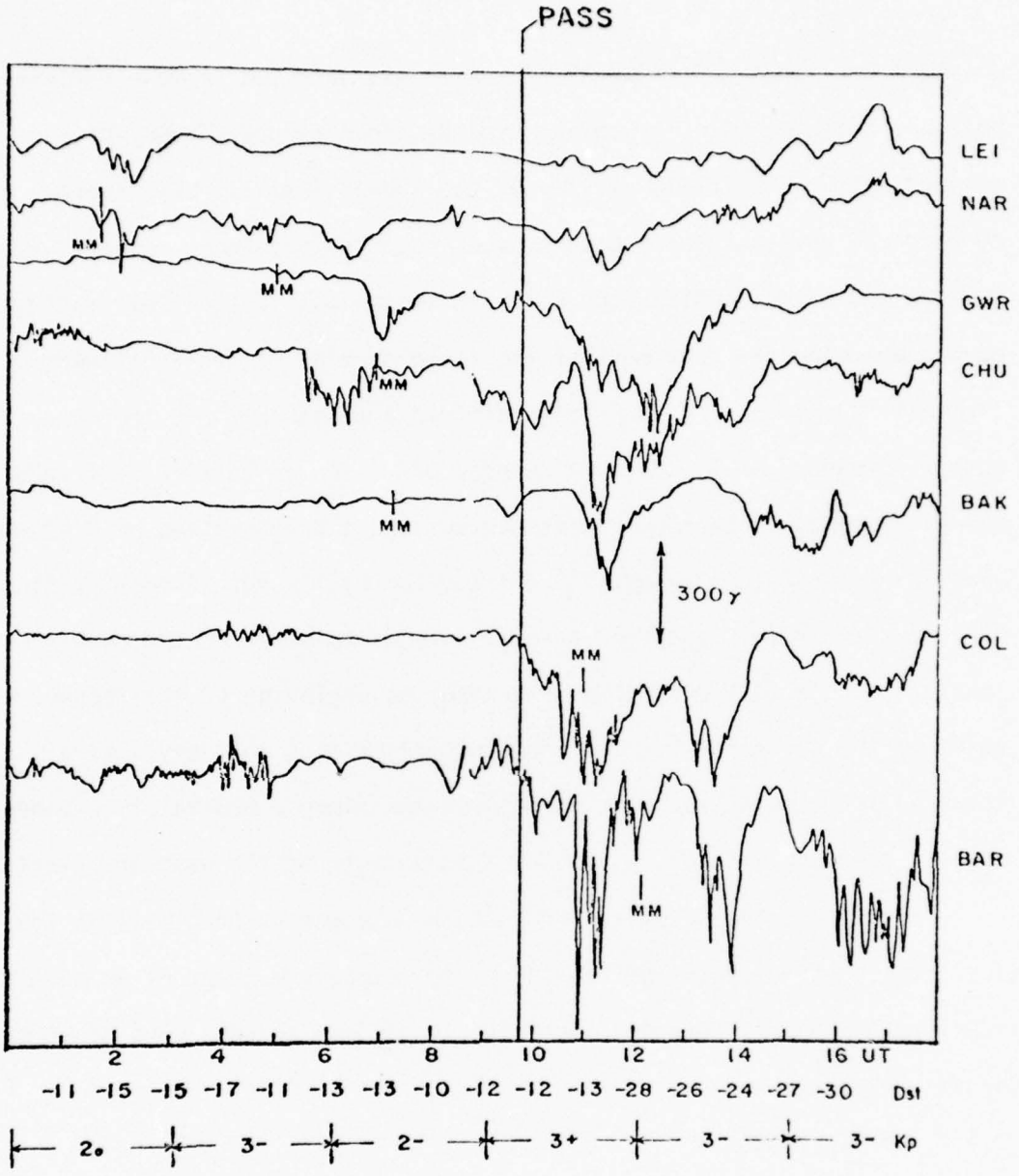

Figure 23

March 9 H-component magnetic records from stations located at various magnetic local times around the night side auroral zone. The M's mark local magnetic midnight at each station, and the vertical line (pass) indicates the time at which the satellite crossed Alaska. The broad negative bay at Churchill and the very narrow and weak negative bay at college show that the satellite pass occurred just at the end of the expansive phase and the beginning of more intense magnetic substorm.

a bright arc about 100 km south of Inuvik was observed to move rapidly poleward bringing with it breakup type discrete auroral forms which covered most of the field of view of the Inuvik 16mm all-sky camera. In response to this auroral substorm, weak negative bays were recorded at College and Barrow. After the poleward expansion, just visible diffuse aurora was observed over most of the field of view of the Fort Yukon 35mm all-sky camera. A very faint diffuse arc, taken to be the equatorward boundary of the diffuse aurora, was observed between Fort Yukon and Ester Dome. Both the discrete aurora and a broad region of diffuse aurora persisted long enough to be traversed by the satellite at 9:41 UT. Just after this passage, auroral arcs which were located over Inuvik began to move equatorward marking the beginning of the recovery phase of the auroral substorm. Not long after this recovery, there occurred at least three additional substorms along a moderately expanded oval further complicated by several enhancements of the westward electrojet.

In summary, the satellite crossed the Alaskan auroral oval in the late evening time sector of the end of the expansive phase of an auroral substorm. Both discrete and just visible diffuse auroras were traversed by the satellite.

2.5.2 Precipitation

Figure 24 shows the particle precipitation observed by the satellite on March 9. The morphology of the electron precipitation is similar to the March 14 precipitation in that: (1) two prominent peaks in both the total number and energy flux profiles set at the poleward end of a broad flat background precipitation and (2) equatorward of the two energetic peaks, the background precipitation extends over a considerable distance void of any prominent peaks. The two peaks labeled 1 and 2 and a

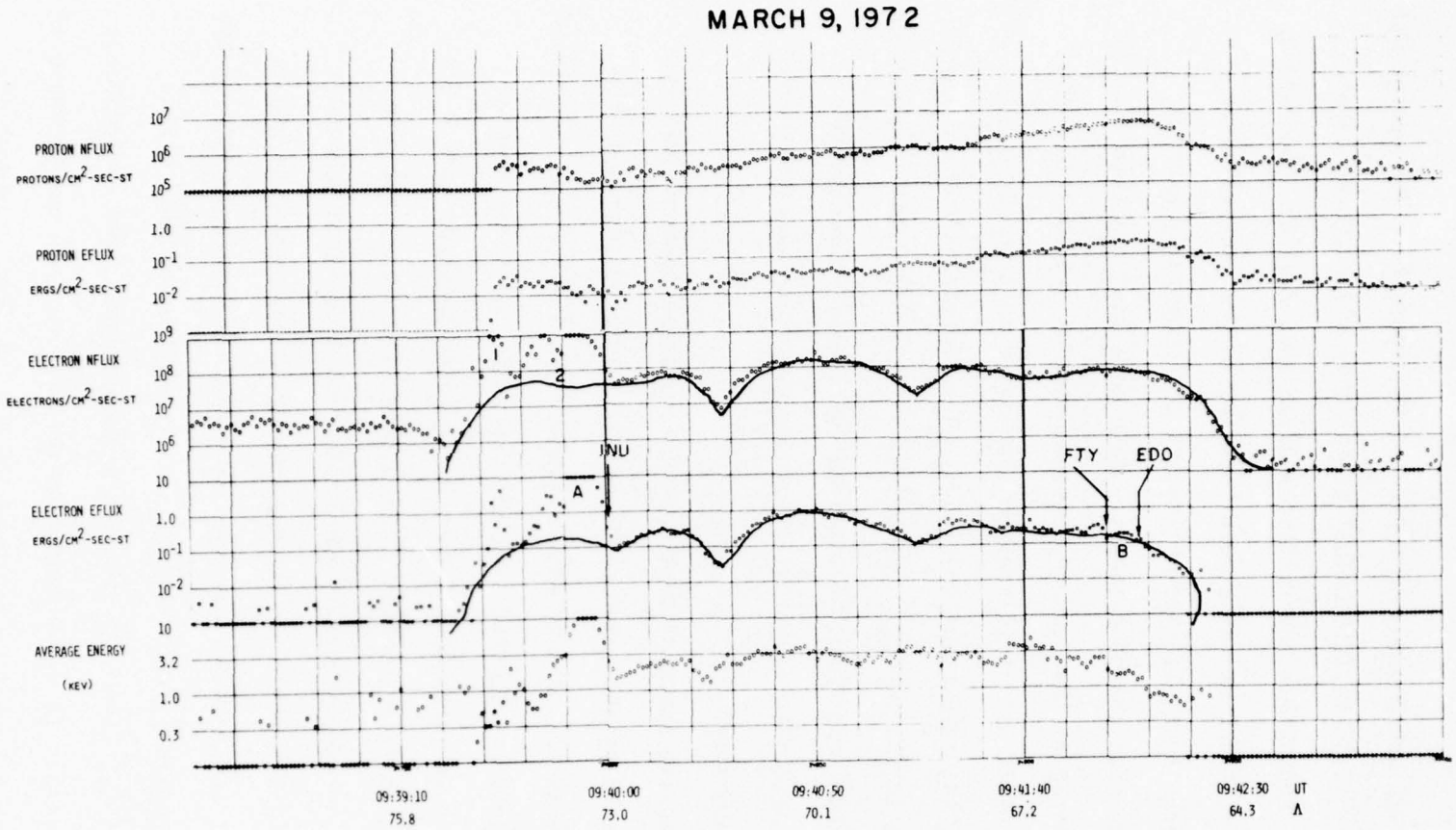

Figure 24

March 9 particle precipitation profiles showing peaks 1 and 2 and the subjectively drawn background precipitation. The letters A and B refer to the auroral arc and edge of the diffuse aurora shown in Figure 29. The arrows indicate the actual positions of these auroral forms as determined from indicated all-sky camera stations.

subjectively drawn background are indicated in Figure 24. The background precipitation is 10.5° in latitudinal extent with well defined boundaries at 74.8°Λ and 64.3°Λ and is less regular than what was observed on March 14. Again, there exists a peak (peak 2) in the precipitation whose total energy flux, latitudinal extent and especially average energy is larger than the other peaks. Also note that the total energy flux average energy of the background precipitation are less than that observed on March 14 but still greater than prior to a substorm.

Like March 14, the proton precipitation is spread throughout the electron precipitation region. The proton total energy flux is about an order of magnitude less than the total energy flux of the electron background precipitation except at the equatorward end where both are comparable in magnitude.

The progressive spectral development across the auroral oval is shown in Figure 25 by the seven point energy spectra associated with each of the one-second data points in Figure 24. The spectra associated with peaks 1 and 2 are labeled. Of the two peaks, only the peak 2 spectra exhibits an extremum. Figure 26 compares selected peak 2 and two adjacent background spectra. This figure illustrates the same spectral changes associated with the production of a large change in both the total energy flux and average energy as has been observed in the profiles of the previous passes. Note that in Figure 25 some of the spectra in the uniform precipitation also exhibit a spectral change similar to peak 2. Figure 27 compares selected peak 1 and two adjacent background spectra. It is evident from this figure that the increase in total number and energy flux is a result of a substantial and nearly

MARCH 9, 1972

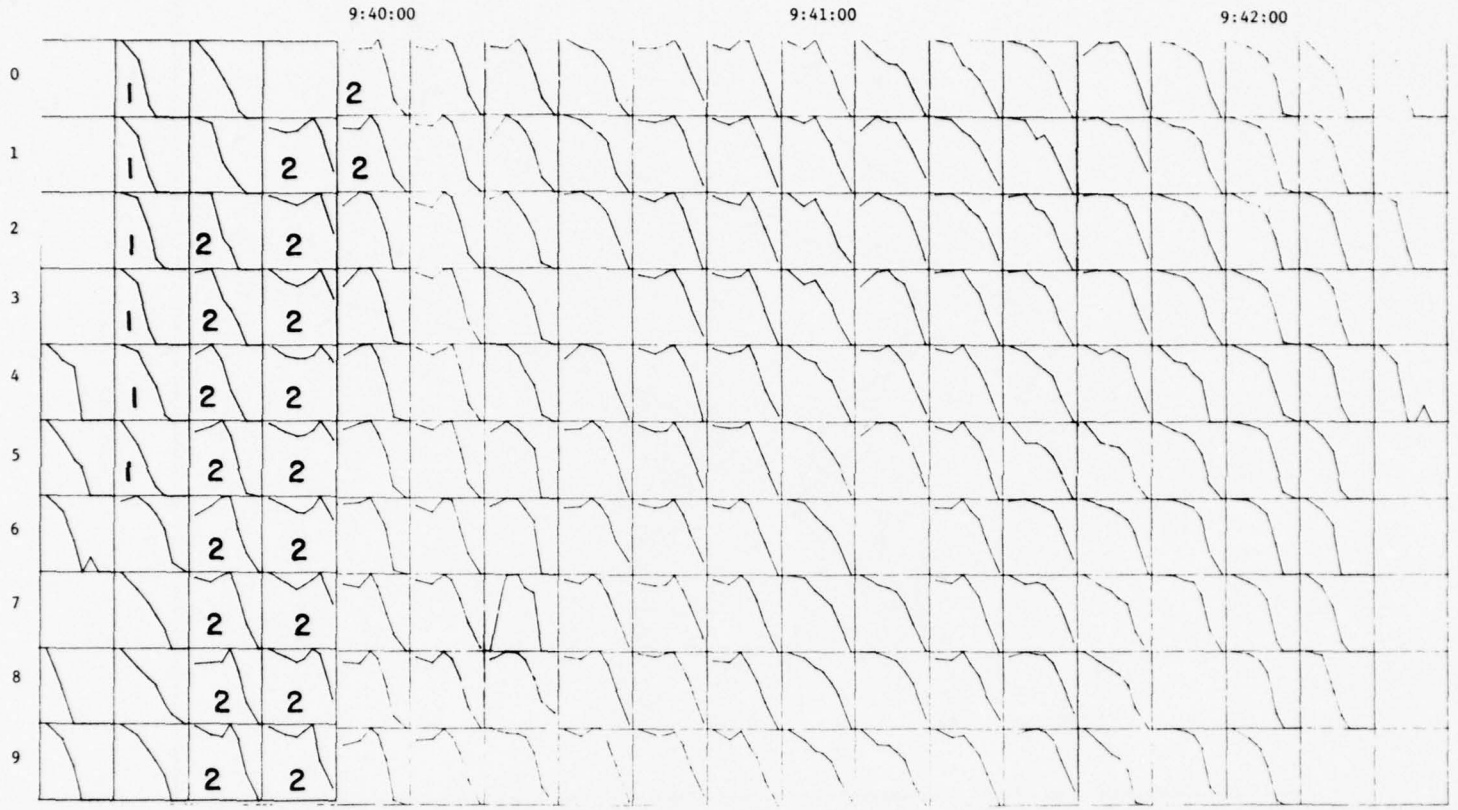

Figure 25

Seven point electron energy spectra associated with each of the one second data points in Figure 25. Time progresses horizontally from left to right in columns of 10 seconds intervals; each column progresses in time vertically from top to bottom in one second intervals. Spectra associated with the numbered peaks in the flux profiles in Figure 26 are indicated by the appropriate number. Note the well-defined extremum associated with peak 2 and even some of the spectra in the uniform precipitation region equatorward.

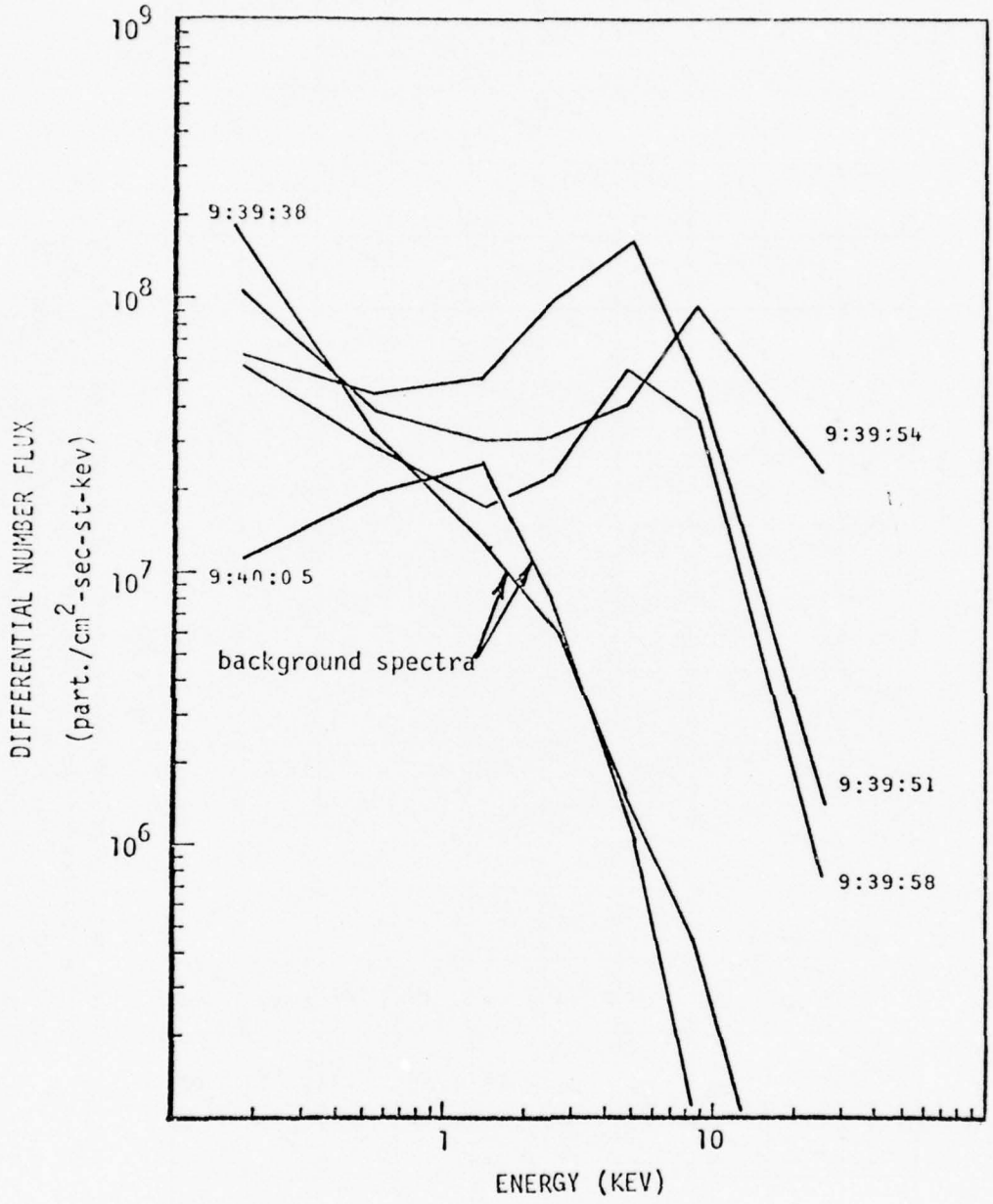

Figure 26

March 9 selected peak 2 and adjacent background spectra. These spectra illustrate the development of a spectral extremum with an increase in the differential number flux on the high energy side of the extremum as the extremum shifts toward higher energies. A large increase in both the total energy flux and average energy profiles is attributed to this type of spectral change.

symmetric increase in the differential number flux over the entire energy spectrum. The symmetric increase explains the lack of a significant increase in the average energy.

2.5.3 Correlation

On March 9 the satellite passed west of the Alaskan all-sky camera chain between the times 9:40 and 9:43 UT (∿22:00 MLT). Figure 28 shows a set of all-sky camera photographs taken at one-minute intervals by the Inuvik, Fort Yukon, and Ester Dome stations. As shown, the auroral forms observed at Inuvik are patches of luminosity which suddenly appear and disappear from one frame to the next. This is the result of viewing auroral arcs and arc segments through a moving patchy cloud layer. From the 9:39 Inuvik photograph, it is clear that an intense active rayed arc labeled A is traversed by the satellite in the 9:40 photograph. The faint diffuse "arc" (labeled B) seen south of Fort Yukon zenith is the equatorward limit of the diffuse aurora. The position of the arc A is determined from the 9:40 Inuvik photograph and the equatorward boundary of the diffuse aurora (B) is determined from the 9:42 Ester Dome and Fort Yukon photographs. These positions are marked by arrows in Figure 24. The difference in the position of the equatorward edge of the diffuse aurora as determined by the Fort Yukon and Ester Dome photographs can be attributed to the subjective location of this edge on the Ester Dome photograph where no clear sharp boundary is evident. Auroral arc A corresponds closely to peak 2. Because the satellite's 110 km trajectory is on the edge of the Inuvik photograph, not enough auroral detail can be seen to explain the existence of peak 1.

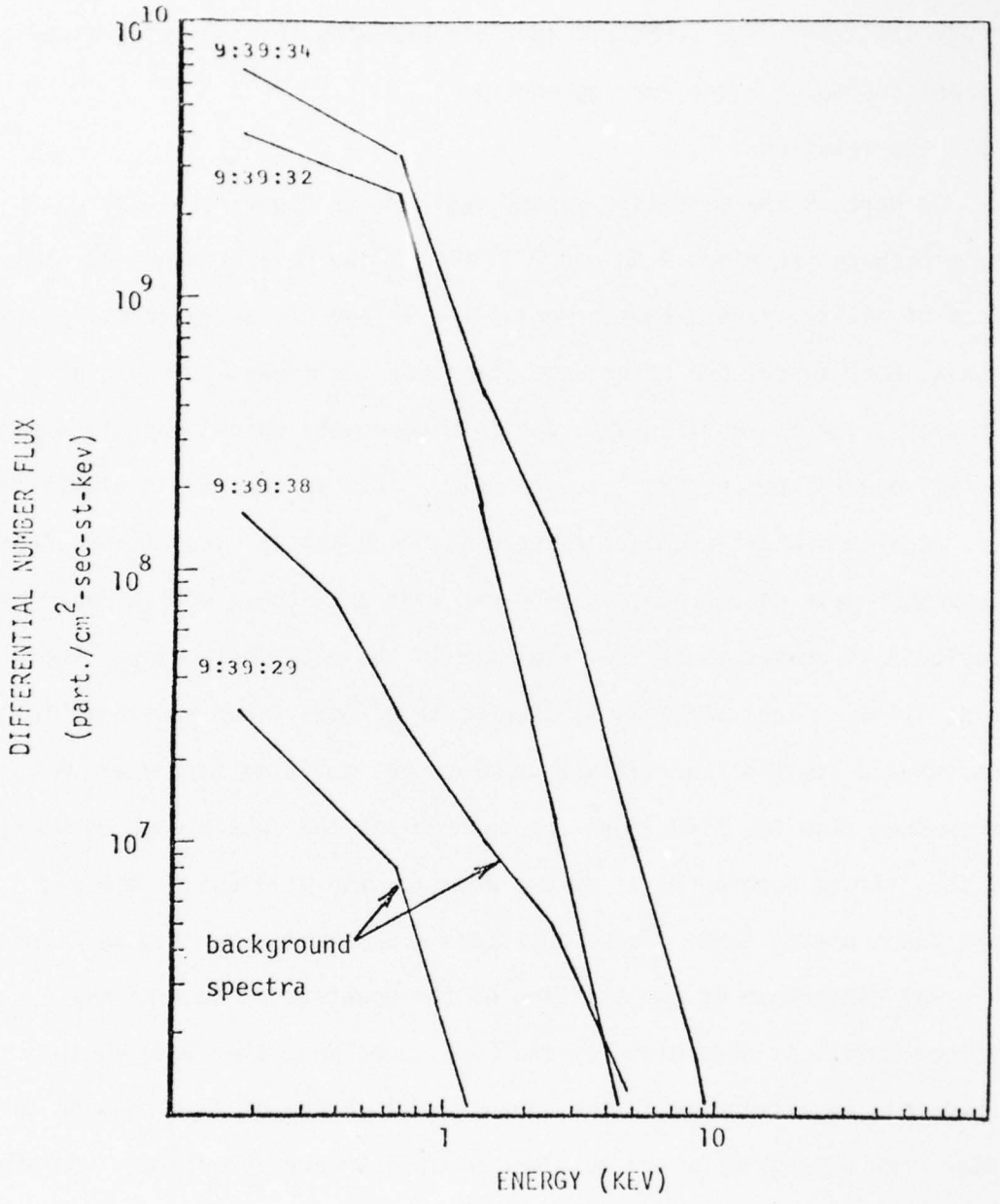

Figure 27

March 9 selected peak 1 and adjacent background spectra. These spectra illustrate the increase in the differential number flux over most of the energy spectrum. A moderate to large increase in the total energy flux and a small to moderate increase in the average energy are attributed to this type of spectral change.

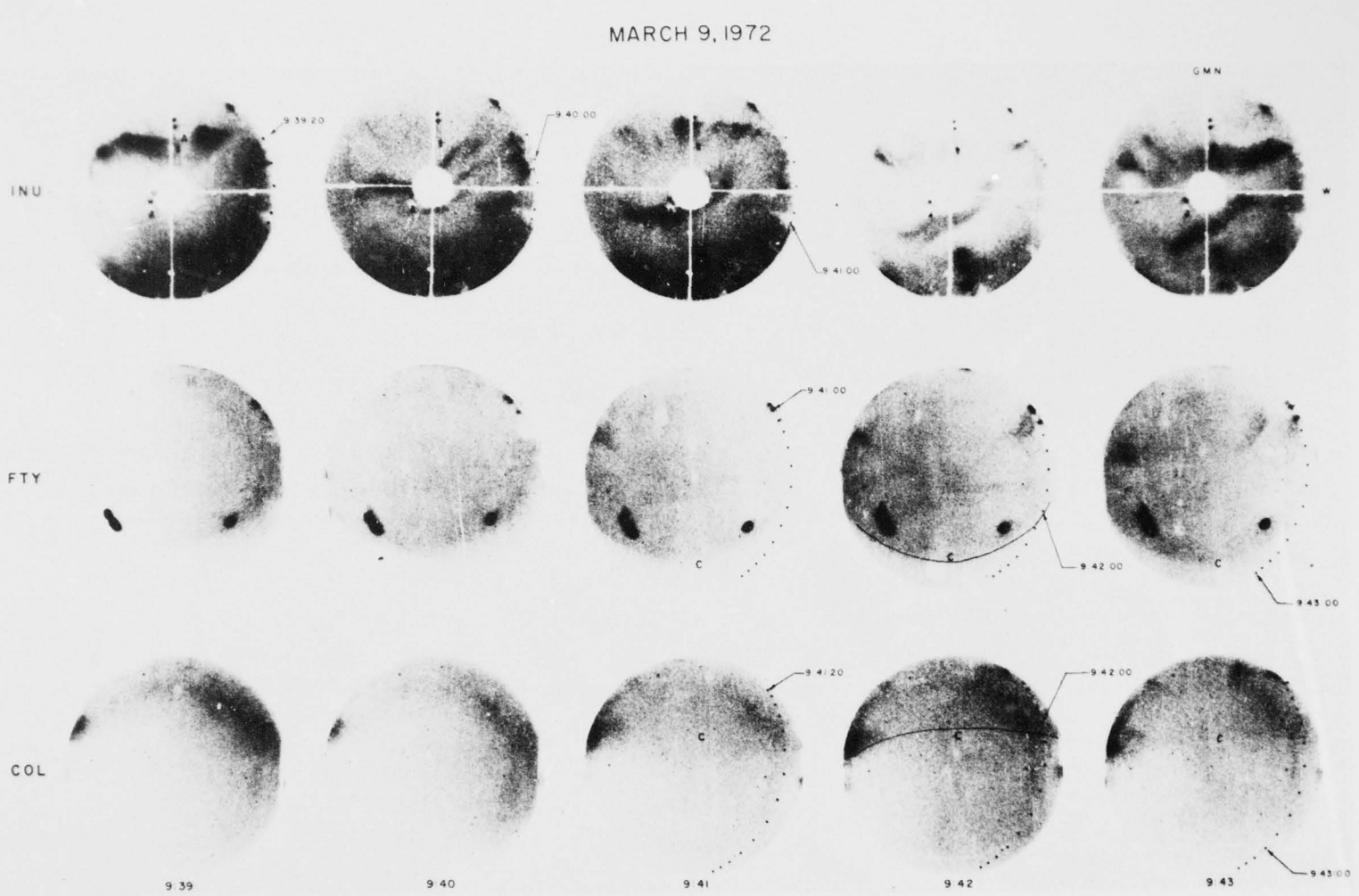

Figure 28

Inuvik, Fort Yukon, and Ester Dome all-sky camera coverage of the March 9 pass. Auroral arc A and equatorward edge of broad region of diffuse aurora B were traversed by the satellite whose 110 km trajectory is represented by the sequence of dots. The poleward edge of diffuse aurora not visible due to clouds. The trajectory point which corresponds closest in time to the all-sky photographs is indicated.

Change in Energy Spectrum	Index No. of Peak	Effects on the Precipitation Latitudinal Profiles						Observed Auroral Form	Comment
		Total no. flux el./(cm^2-sec-st)		Total eng. flux ergs/(cm^2-sec-st)		Average eng. (kev)			
		rel.* change	greatest† value	rel.* change	greatest value	rel.* change	greatest value		
development of a pronounced spectral extremum and a substantial increase in the differential number flux on the high energy side of the extremum as the extremum shifts towards higher energies	2	+1.2	1.4E9	+2.5	34.3	+0.9	15.5	active rayed arc	this type of spectral change is observed in all but the March 7 precipitation; the latitudinal extent and the changes in the total energy flux and average energy are larger than for other types of changes in the energy spectrum
diff. no. flux over the entire energy spectrum increases	1	+1.6	3.9E9	+1.7	4.5	0	.71	assumed to produce an auroral arc but not observed	spectral changes similar to this type observed in all the precipitation data; associated with moderate to large increases in the total energy flux and small to moderate increases in the average energy

*relative change is given as the orders of magnitude difference between the background and the peak value, e.g. rel. change 1.5 implies $x=10^{1.5}y$

†values given in computer exponential notation, e.g. 8.0E9 implies 8.0×10^9

TABLE 8

Summary of the Energy Spectral Changes and Associated Auroral Luminosity for March 9.

2.5.4 Summary

The morphology of this precipitation was similar to the March 14 precipitation in that two intense and energetic peaks which correlated with at least one auroral arc were observed on the poleward end of a background precipitation 10.5° in latitudinal extent with well-defined boundaries at 64.3°Λ and 70.5°Λ. Equatorward of the two energetic peaks, the background precipitation extended over a considerable distance void of any prominent peaks and producing a broad region of visible diffuse aurora.

The background precipitation was less energetic and regular than that observed on March 14 but more energetic than prior to a substorm. Two significant and different changes in the energy spectrum were observed associated with the two peaks in the profiles. These spectral changes, their relative effects on the total number flux, total energy flux and average energy, and the type of auroral luminosity produced are listed in Table 8. Like March 14, the proton precipitation extended the full length of the electron precipitation and remained uniform over most of this region. The total proton energy flux was approximately an order of magnitude less than the total electron energy flux over most of the electron precipitation region.

2.6 THE MARCH 7 PASS

2.6.1 General magnetic and auroral observations.

Figure 29 shows the March 7 H-component magnetic records from the indicated stations. The Dst values show that a moderate geomagnetic storm was in progress during March 7, and the very large K_p values indicate an unusually high degree of auroral storminess during most of

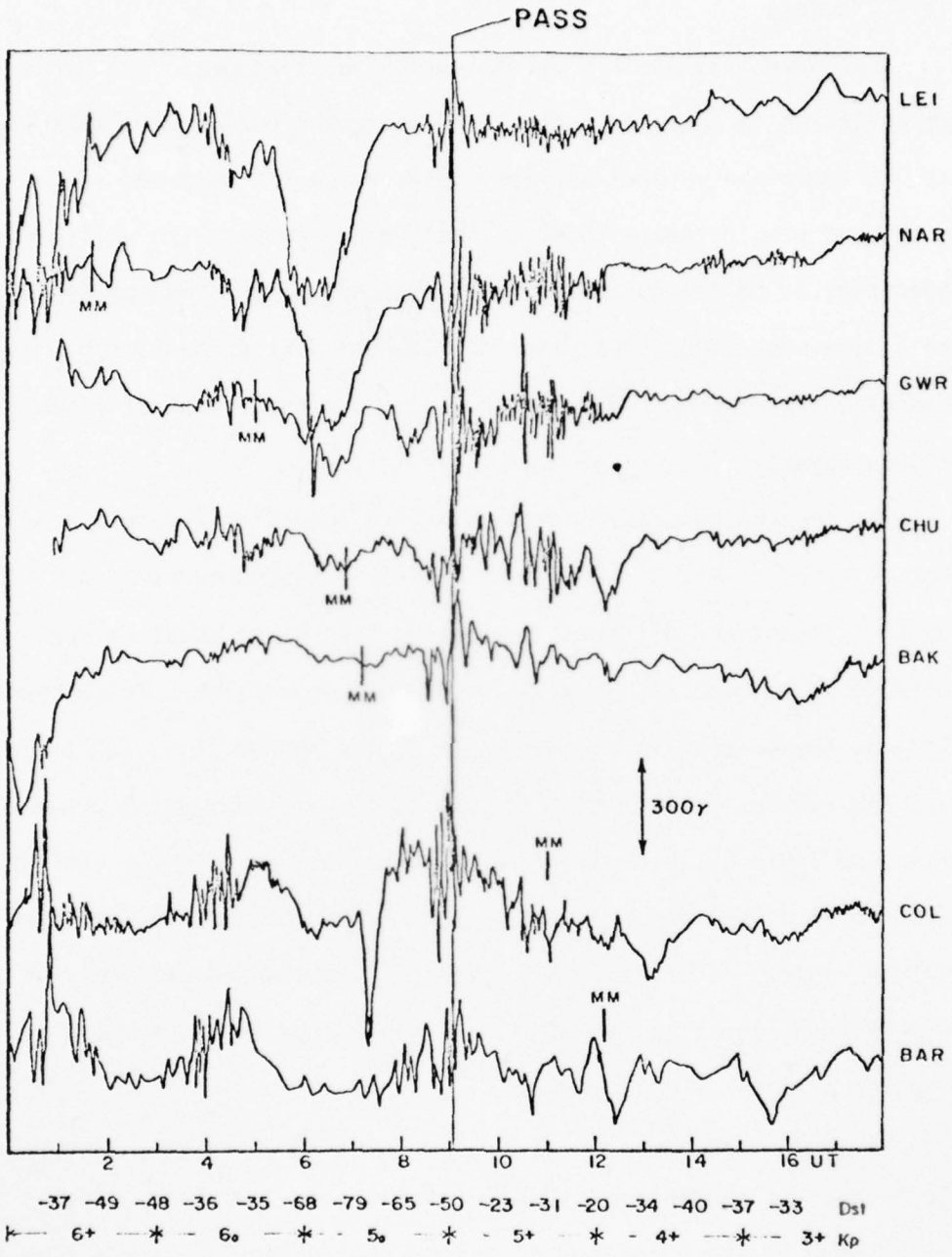

Figure 29

March 7 H-component magnetic records from stations located at various local magnetic times around the night side auroral zone. The M's mark local magnetic midnight at each station, and the vertical line (pass) indicates the time at which the satellite crossed Alaska. These records show that the pass occurred after a magnetic substorm during a complicated magnetic period.

this day. In spite of the very complicated magnetic activity, it is clear from the Great Whale River, Narssarssuaq and Leirvoger records that a very intense magnetic substorm, centered around Narssarssuaq in the early morning sector, began no later than 5:45 UT. About this time, College was recovering from a positive bay, and moderately active rayed arcs had just developed south of Ester Dome. These arcs then slowly drifted 200 km further south where they remained until 7:15 UT, at which time the arcs greatly intensified. One minute later, the arcs began to expand rapidly poleward, and a very intense well-developed westward traveling surge passed overhead at Ester Dome. After the passage of this surge, intense diffuse aurora was observed as far north as Fort Yukon and beyond the southern field of view of the Ester Dome all-sky camera. With the passage of the surge, the usual H-component negative bays were observed by the Alaskan stations. These negative bays were short in duration, and by 8:00 UT, positive bays were once again in progress in College. After the recovery of the negative bay, the intensity of the diffuse aurora had decreased significantly, being brightest overhead and south of Ester Dome. The leading arcs of the poleward expansion reached Inuvik at 8:30 UT after pausing over Fort Yukon for some time. As shown in Figure 29, the satellite crossed the Alaskan auroral oval well into the recovery phase of the intense 5:45 UT substorm and during a time of rapid magnetic oscillations observed at College and later at Barrow. During this period of magnetic oscillation, the intensity of the diffuse aurora over Ester Dome was greatly enhanced. Just before and after the pass two discrete arcs embedded in this diffuse aurora over Ester Dome were observed. Also, a very active discrete arc

and arc segments were also observed over Inuvik. After the passage of the satellite, the active discrete aurora over Inuvik and the diffuse aurora, which was observed as far south as the southern horizon at Ester Dome persisted until dawn. The magnetic activity at all stations after 12 UT remained relatively quiet for the duration of March 7.

In summary, the satellite crossed the late evening Alaskan auroral oval after the recovery phase of a magnetic substorm, and during a complicated auroral and magnetic period. Both discrete and diffuse auroral forms were traversed by the satellite.

2.6.2 Precipitation

Figure 30 shows the particle precipitation profiles observed by the satellite on March 7. In both the total number and energy flux profiles, nine prominent peaks were observed on a background precipitation whose latitudinal extent is 15.5°Λ. The nine peaks and a subjectively drawn background is indicated in Figure 30. Peaks 1, 2, 7, and 8 exceeded the 10^9 el/(cm^2-sec-st) computer plot threshold and their values are 2.5×10^9, 9.4×10^9, 1.7×10^9, and 1.4×10^9 el/(cm^2-sec-st) respectively. The total energy flux of peak 2 also exceeded its 10 ergs/(cm^2-sec-st) plot threshold and its value is 20.7 erg/(cm^2-sec-st). In the total number flux profile, the equatorward boundary of the background precipitation, unlike all the other passes, exhibits a gradual decrease to threshold extending some 400 km to 58.0°Λ. Although not completely shown, the poleward boundary of the background precipitation is well defined at 73.5°Λ. The total energy flux and average energy of the background precipitation slowly increases to a maximum value of approximately of 2 ergs/(cm^2-sec-st) and 7 kev respectively at 64°Λ before slowly decreasing

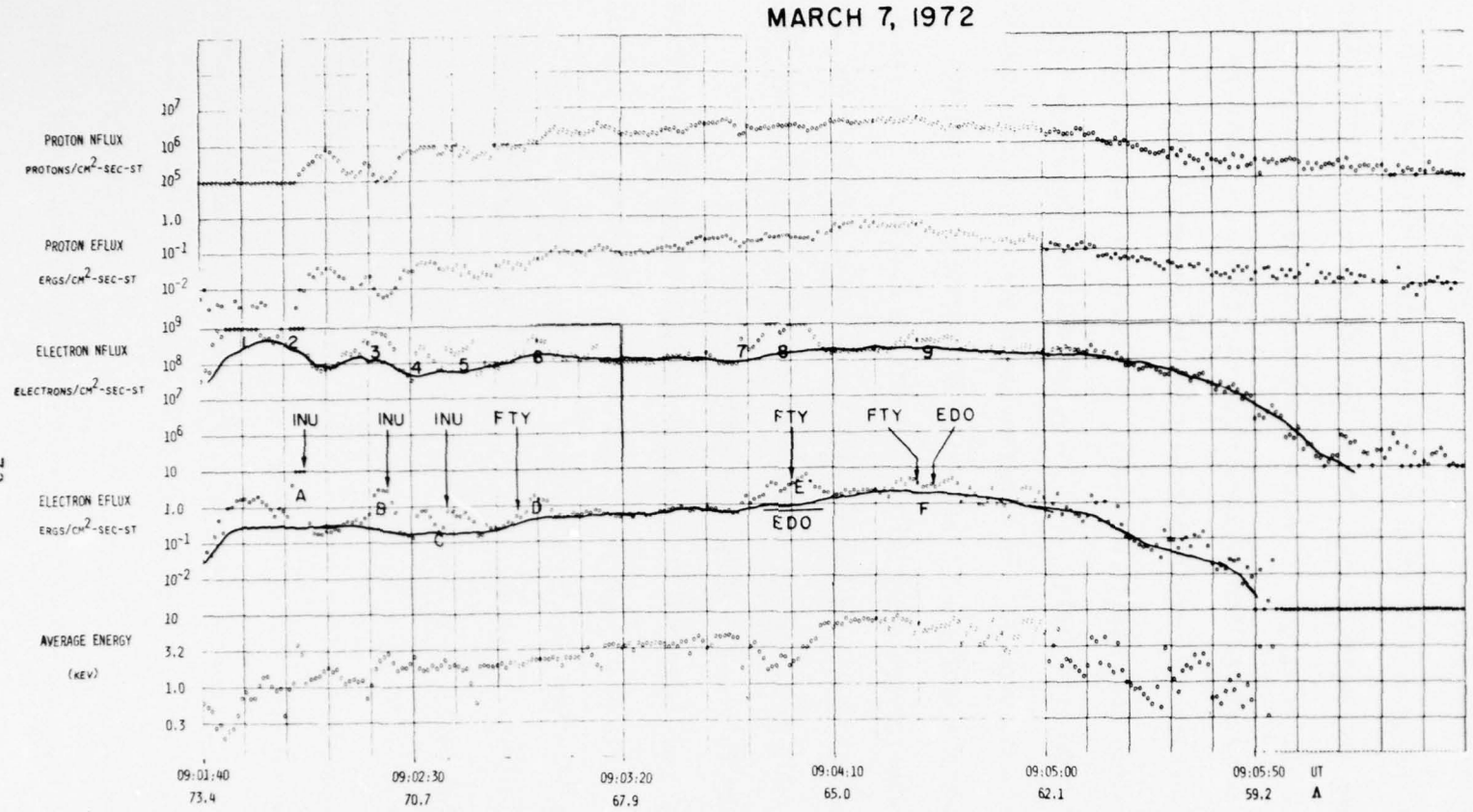

Figure 30

March 7 particle precipitation profiles showing peaks 1 through 9 and the subjectively drawn background precipitation. The letters A through F refer to the auroral arcs in Figure 34 and the arrows indicate the actual positions of these auroral arcs as determined form the indicated all-sky camera stations. 73

to threshold farther equatorward. Most of the nine peaks are well separated, and unlike all the other passes presented, there does not exist an intense and energetic peak whose average energy and latitudinal extent is particularly large. Like the two previous passes which occurred after a substorm, the background precipitation is shown to extend a considerable distance equatorward of the energetic peaks, but unlike the previous post substorm passes, the background precipitation is not void of prominent peaks. Also note the distinction between peaks 1 through 3 and 4 through 9. The three poleward peaks have corresponding peaks in the average energy profile, while in contrast, the average energy of the equatorward peaks either exhibit no change or a decrease. Recall that such decreases in the average energy were a feature observed in the background precipitation equatorward of the energetic peaks in the March 14 and 16 electron precipitation profiles.

The proton precipitation is spread throughout the region of electron precipitation. This was shown to be the case for the other two passes which occurred after an auroral breakup. The total energy flux is greater than that which was observed on March 14 and 9 and comparable to the broad proton peaks observed prior to a breakup.

Figure 31 shows the sequence of energy spectra associated with each of the one-second data points in Figure 31. The spectra associated with peaks 1, 2, 3, and some of the spectra equatorward of peak 9 exhibit a rather degenerate extremum. Certainly, extrema as pronounced as those observed in the other four passes are not evident among the spectra in Figure 31. The spectra associated with peaks 1, 2, and 3 compared to their adjacent background spectra show an enhanced differential number

MARCH 7, 1972

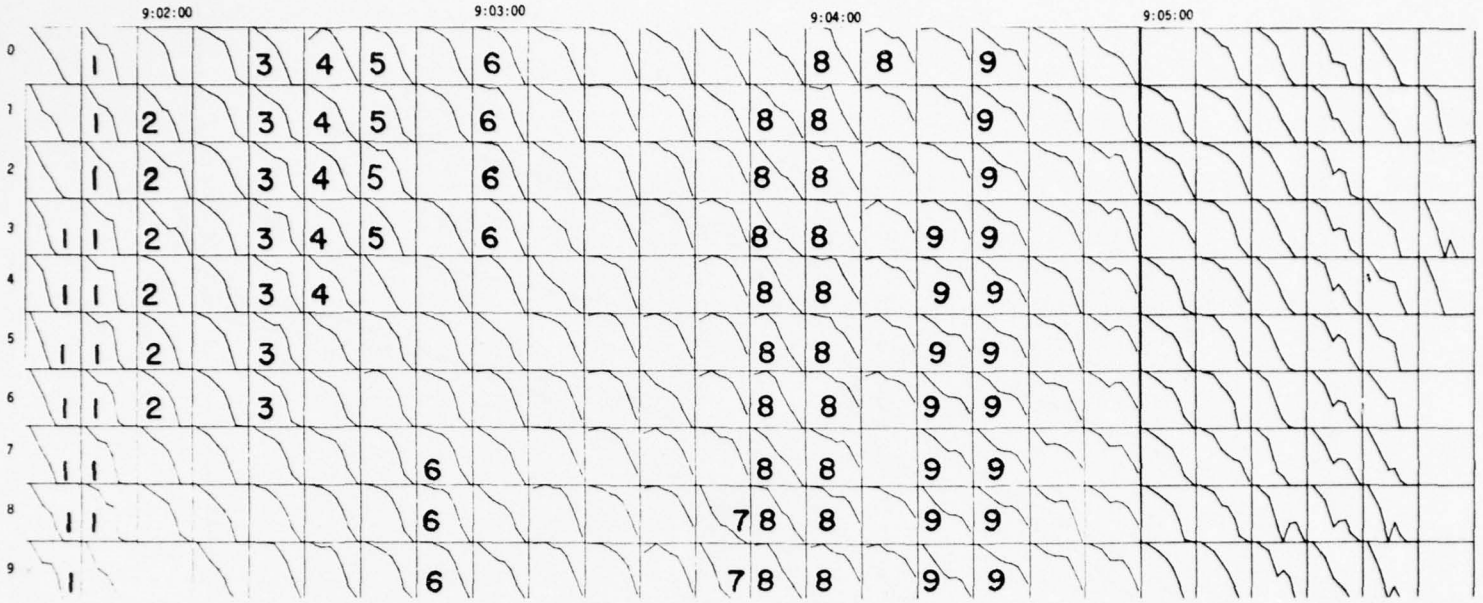

Figure 31

Seven point electron energy spectra associated with each of the one second data points in Figure 30. Time progresses horizontally from left to right in columns of 10 seconds intervals; each column progresses in time vertically from top to bottom in one second intervals. Spectra associated with the number peaks in the flux profiles in Figure 30 are indicated by the appropriate number. Note that there does not exist any spectra exhibiting a well-defined extremum as has been seen in previous four passes.

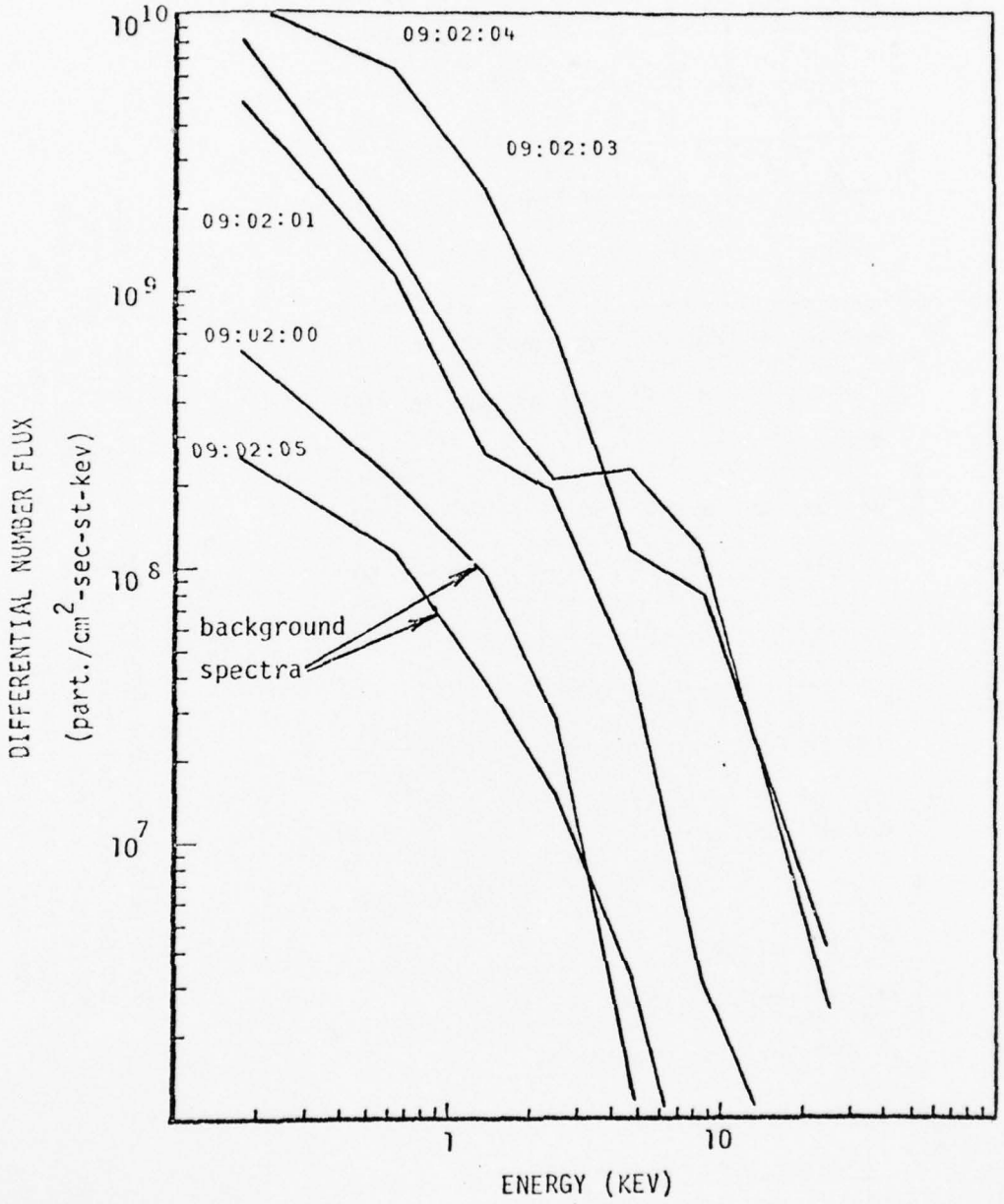

Figure 32

March 7 selected peak 2 and adjacent background spectra. These spectra illustrate the increase in the differential number flux over the entire energy spectrum. A moderate to large increase in the total energy flux and a small to moderate increase in the average energy are attributed to this type of spectral change.

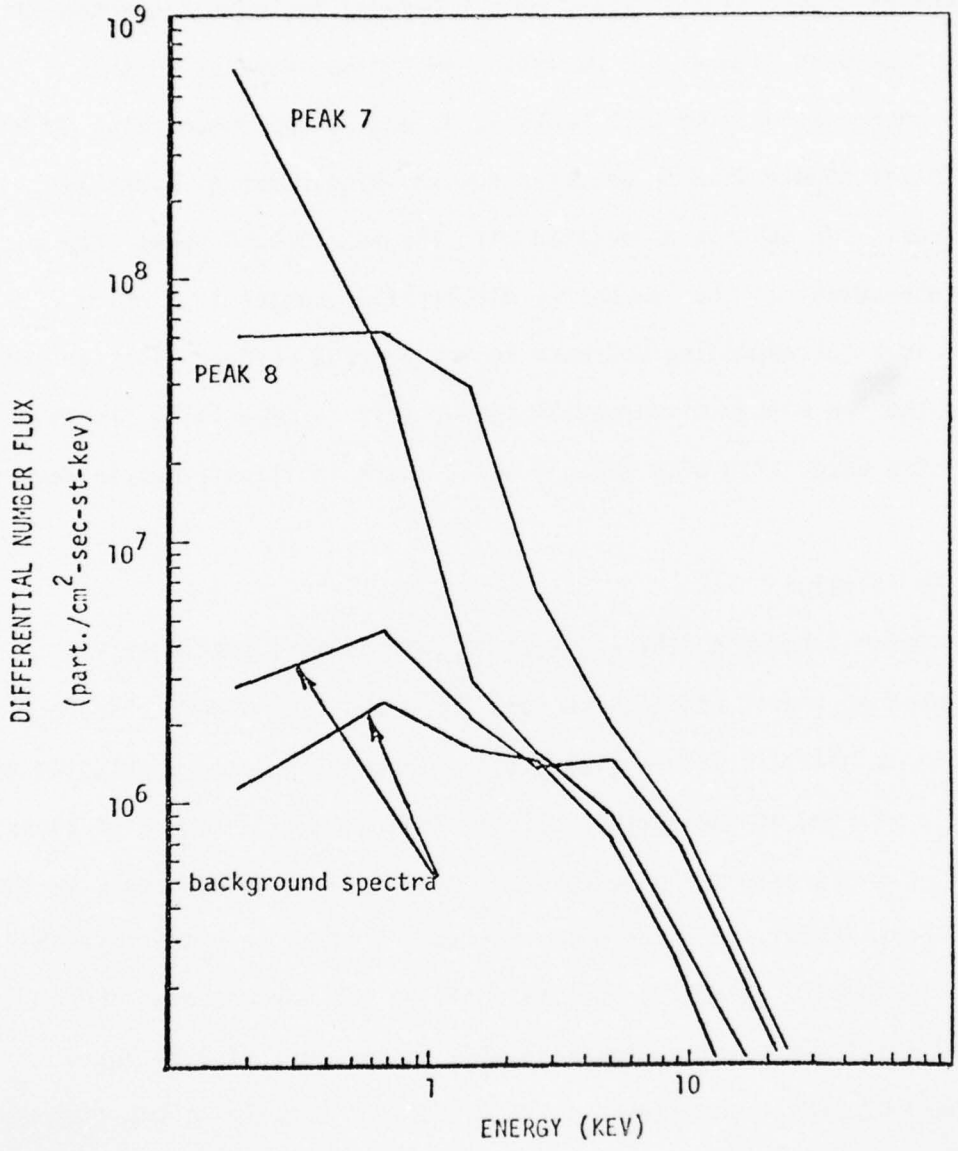

Figure 33

March 7 peak 7, 8, and adjacent background spectra. These spectra illustrate the large increase in the low energy differential number flux while the higher energy differential number flux increased only slightly.

flux over the entire energy spectral range. This overall enhanced differential number flux is especially prominent for peak 2 spectra and is illustrated in Figure 32. As indicated by the increase in the average energy associated with peaks 1, 2, and 3, the enhancement in the differential number flux is weighted towards higher energy particles. In contrast, the spectra associated with the equatorward peaks show a large enhancement in the low energy differential number flux which results in a corresponding decrease in the average energy. This enhancement in the low energy differential number flux is especially dramatic for spectra associated with peaks 7 and 8 which is illustrated in Figure 33.

2.6.3 Correlation.

On March 7 between 9:01 and 9:04 UT (∿22:20 MLT) the satellite passed west of Inuvik and east of Fort Yukon and Ester Dome. Figure 1 shows the satellite's 110 km field line intercept trajectory relative to the field of view of the Alaskan all-sky camera chain. Figure 34 shows a set of all-sky camera photographs taken at one-minute intervals by the Inuvik, Fort Yukon, and Ester Dome cameras. A light leak destroyed the western field of view of the Fort Yukon film, but fortunately, these data are still usable since the satellite passed east of Fort Yukon.

The 9:02 Inuvik photograph corresponds most closely to the time at which the satellite was in the vicinity of Inuvik, thus the 9:02 photograph is used in the correlation. In this photograph, the discrete aurora over Inuvik along the satellite trajectory is composed of one distorted rayed arc and two less intense homogeneous arc segments equatorward. The rayed arc and the two arc segments are labeled A, B,

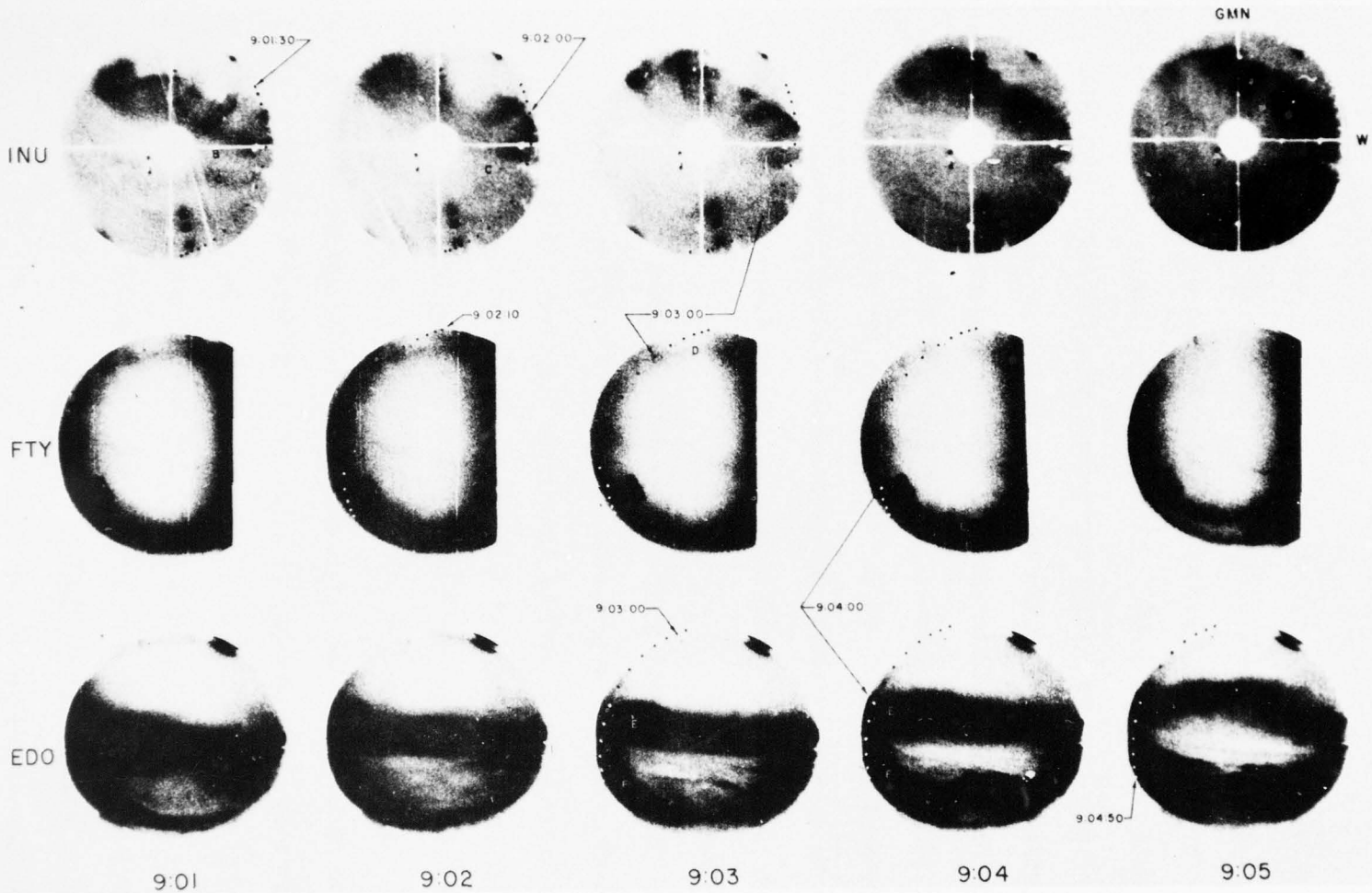

Figure 34

Inuvik, Fort Yukon, and Ester Dome all-sky camera coverage of the March 7 pass. Auroral arcs A, B, C, D, E, and F were traversed by the satellite whose 110 km trajectory is represented by the sequence of dots on the photographs. The trajectory point which corresponds closest in time to the all-sky photograph is indicated.

and C in Figure 34. Their positions relative to the precipitation are indicated by the (INU) arrows in Figure 30. The correspondence is remarkably close. However, there is no luminosity poleward of arc A to correspond with the peak 1 precipitation. A careful look at the satellite's trajectory relative to the auroral arc A shows that the peak 1 precipitation is probably a result of the satellite passing parallel to the outside edge of a large fold, clearly seen in the arc, before actually crossing it to recording the peak 2 precipitation. The arc segment C is no doubt produced by peaks 4 and 5. Because these arc segments lie near the zenith, we have a relatively good measure of their latitudinal extent which is indicated by the horizontal line in Figure 30 and falls nicely over peaks 4 and 5.

In the Fort Yukon photographs mostly diffuse aurora is visible. The luminosity along the eastern edge of the field of view indicates that a relatively uniform layer of luminosity did cover the sky during the satellite pass. Notice that the poleward extent of the diffuse aurora appears to terminate sharply in an arc (labeled D). This was found to be the case on March 9 and 14. The position of this poleward arc relative to the precipitation is marked by an (FTY) arrow in Figure 30. The position correlates poorly with peak 6 compared to previous correlations. At any rate, the poleward arc observed on the 9:03 Fort Yukon all-sky photograph is not entirely due to the limit of the diffuse aurora. It should be mentioned that the field of view of the Fort Yukon all-sky camera encompasses the peak 3, 4, and 5 precipitation which has shown to produce auroral luminosity observed by the Inuvik all-sky camera. However, this luminosity is not seen from Fort Yukon due to

AD-A032 730 ALASKA UNIV COLLEGE GEOPHYSICAL INST F/G 4/1
A CORRELATION OF DISCRETE AND DIFFUSE AURORA WITH PARTICLE PREC--ETC(U)
AUG 75 R S CAVERLY, G J ROMICK F19628-74-C-0188
UNCLASSIFIED SCIENTIFIC-4 AFCRL-TR-75-0508 NL

2 OF 2
ADA032730

END

DATE
FILMED
2 - 77

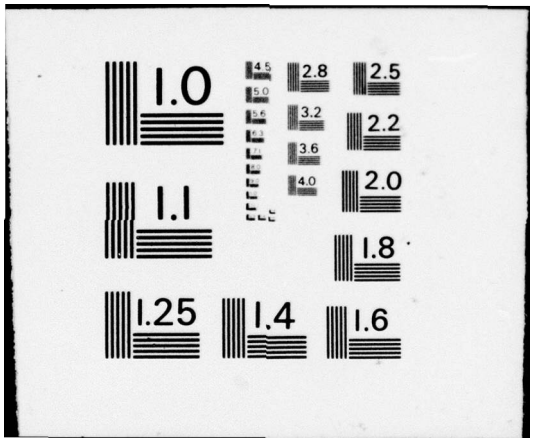
1.0
1.1
1.25
1.4
1.6
1.8
2.0
2.2
2.5
2.8
3.2
3.6
4.0
4.5
5.0
5.6

clouds on the Fort Yukon horizon. On the equatorward edge of the 9:04 Fort Yukon photograph two auroral arcs are visible. The luminosity of these arcs is produced by the two arcs E and F seen over Ester Dome. The lower border of arc F is just on the edge of the Fort Yukon all-sky photograph. The position of arcs E and F relative to the precipitation is marked by the two (FTY) arrows in Figure 31. The correspondence is fairly good.

From the 9:04 Ester Dome photograph, the latitudinal extent of the bright arc (E) is indicated by the horizontal line below the (EDO) arrow in Figure 30. The position and latitudinal extent of arc E corresponds well with peak 8. After passing through arc E, the satellite once again entered a region of diffuse aurora which, as expected from Figure 31, is visible and more intense than the diffuse aurora poleward of arc E. Continuing farther south, the satellite encountered another arc F. Because arc F is very broad and the trajectory is on the extreme edge of the Ester Dome photograph where auroral detail is limited, a well-defined lower border does not exist to position arc F. However, the satellite does enter a region of enhanced luminosity between the times 9:03 and 9:04. An arrow (EDO) at 9:03:30 in Figure 30 shows an approximate location of arc F, and it clearly falls within the peak 9 precipitation.

2.6.4 Summary

The March 7 satellite pass crossed the late evening Alaskan auroral zone during a complicated auroral and magnetic period after the recovery of a magnetic substorm. Nine peaks on a background precipitation 15.5° in latitudinal extent with boundaries at 58.G°Λ and 73.5°Λ were observed. Except for the most poleward peak, the other peaks correlated with auroral arcs. The background precipitation was energetic enough over a

large portion of its extent to produce visible diffuse aurora in which at least three auroral arcs were observed. Two significant and different changes in the energy spectrum were associated with the 9 peaks in the electron precipitation. These spectral changes, their relative effects on the total number flux, total energy flux and average energy profiles, and the type of auroral luminosity produced are listed in Table 9. Like March 9 and 14, the proton precipitation extended the full length of the electron precipitation and remained uniform over most of this region. The total proton energy flux was approximately an order of magnitude less than the total electron energy flux.

2.7 CHAPTER SUMMARY

The particle precipitation observed on five satellite passes across the late evening auroral zone during different phases of the auroral substorm have been presented and correlated with auroral observations along the Alaskan meridian chain of all-sky cameras. The electron precipitation data is of primary interest in this study but proton data was examined only to establish where the proton precipitation is located in relation to the electron precipitation and to what extent the protons contribute to the total luminosity.

Seven point energy spectra given each second as a function of latitude were displayed for each of the five passes. These spectral displays revealed the repeated occurrence of three major types of changes in the energy spectrum called here for later reference types 1, 2 and 3. Each type has a particular effect on the total energy flux and average energy. These effects and the changes in the energy spectrum are described and depicted below:

Change in Energy Spectrum	Index No. of Peak	Effects on the Precipitation Latitudinal Profiles						Observed Auroral Form	Comment
		Total no. flux el./(cm^2-sec-st)		Total eng. flux ergs/(cm^2-sec-st)		Average eng. (kev)			
		rel.* change	greatest† value	rel.* change	greatest value	rel.* change	greatest value		
diff. no. flux over the entire energy spectrum	1	+1.6	2.5E9	+0.9	2.0	+0.2	1.4	?	spectral changes similar to this type observed in all the
	2	+2.1	9.4E9	+2.0	20.7	+0.6	3.8	active rayed arc	
increases	3	+1.1	7.8E8	+1.2	3.0	+0.5	2.9	homogeneous arc	precipitation data; associated with moderate to large increases in the total energy flux and small to moderate increases in the average energy
differential number flux at the low end of the spectral energy range	4	+0.9	2.8E8	+0.8	0.8	0	1.8	homogeneous arc	found equatorward of the prominent electron peaks; associated with decreases in the average energy
	5	+0.6	4.0E8	+0.3	0.4	-0.5	0.6		
	6	+0.7	5.3E8	+0.6	1.9	0	2.3	homogeneous arc	
(<1 kev) greatly increases while for higher energies, the diff. no. changes little	7	+1.2	1.7E9	+0.2	1.7	-0.8	0.6	homogeneous arc	and small to moderate increases in the total energy flux
	8	+1.2	1.4E9	+0.8	6.8	-0.5	1.6		
	9	+0.5	6.0E8	+0.3	4.8	-0.2	5.0	homogeneous arc	

*relative change is given as the orders of magnitude difference between the background and the peak value, e.g. rel. change 1.5 implies $x=10^{1.5}y$

†values given in computer exponential notation, e. g. 8.0E9 implies 8.0×10^9

TABLE 9

Summary of the Electron Energy Spectral Changes and Associated Auroral Luminosity for March 7.

Type 1. With the initial increase in the differential number flux over the entire energy spectrum, begins the development of a pronounced spectral extremum and a substantial increase in the differential number flux on the high-energy side of the extremum as the extremum shifts towards higher energies. Large changes in both the total energy flux and average energy are attributed to this spectral change.

Type 2. The differential number flux increases over the entire energy spectrum (18 ev to 25.5 kev). Considerable variations in this spectral change do occur. The differential number flux has been observed to increase almost symmetrically, thus causing almost no change in the average energy. The increase has also been observed to develop pronounced extremum and be weighted toward spectral energies above 1 kev, thus causing moderate increases in the average energy. In all cases moderate to large increases in the total energy flux are attributed to this type of spectral change.

Type 3. Differential number flux at the low end of the spectral energy range (<1 kev) greatly increases while for higher energies, the differential number flux changes little. Small to moderate increases in the total energy flux and usually small to moderate decreases in the average energy are attributed to this type of spectral change.

Latitudinal profiles of the total number flux, total energy flux and average energy were presented. Besides affording a cursory examination of the energy spectral changes as a function of latitude, they also provide the morphological interpretation that the electron precipitation is composed of a background precipitation on which set prominent peaks associated with the spectral changes summarized above. Table 10 lists the latitudinal positions of the poleward and equatorward boundaries and extend of the electron precipitation (i.e., the background precipitation) together with the magnitudes of the total number flux, total energy flux, average energy, the type of observed auroral form, the type of spectral change associated with the peaks as referenced above, and a rough estimation of the total number and energy flux and average energy of a representative portion of the background precipitation. It is clear from this table that after an auroral substorm, the background precipitation was observed to be much broader in latitudinal extent, of a greater total energy flux and average energy than prior to a substorm. Also a sizable portion of the background precipitation equatoward of the energetic peaks was observed to be energetic enough to produce a broad region of diffuse auroral luminosity. Prior to a substorm, no visible diffuse luminosity associated with the background precipitation was observed. The peaks associated with the type 1 and 2 spectral change in those passes which occurred after a substorm were of a higher total energy flux and average energy than the type 1 and 2 peaks observed before a substorm. Note that the total number flux of the background precipitation and the type of spectral change seem to be independent of substorm time. Finally, the peaks in Table 10 for each pass are listed in the order in which they were encountered by

pass	magnetic indices and substorm phase	electron precipitation			significant precipitation features					type of spectral change
		poleward boundary °Λ	equatorward boundary °Λ	latitudinal extent °Λ	total no. flux el/(cm^2-sec-st)	total eng. flux ergs/(cm^2-sec-st)	average eng. kev	type of feature	type of aurora	
Mar. 16	1 hr. before Dst=-38 K_p=3$^-$	68.9	63.7	5.2	9.5×10^8	8.6	5.6	peak 1	arc	1
					9.7×10^8	2.4	1.7	peak 2	arc	2
					5.8×10^8	1.7	1.8	peak 3	arc	2
					2.6×10^8	0.4	1.0	peak 4	no lum.	3
					1.2×10^9	0.5	0.3	peak 5	no lum.	3
					1.1×10^8	0.06	0.3	peak 6	no lum.	3
					10^7-10^8	0.01-0.6	∿1.5	backgr. precip.	no lum.	-
Apr. 7	1/2 hr. before Dst=-16 K_p=3$^-$	73.8	66.3	7.5	1.4×10^8	0.3	1.2	peak 1	no lum.	2
					6.4×10^8	2.0	1.9	peak 2	arc	1
					6.3×10^8	5.5	5.5	peak 3	arc	1
					10^7-10^8	0.01-0.1	0.6-1.0	backgr. precip.	no lum.	-
Mar. 14	expansive phase Dst=-4 K_p=2$^-$	74.0	63.8	10.2°	1.1×10^{10}	33.5	2.3	peak 1	not obs.	2
					1.5×10^9	51.9	21.2	peak 2	arc	1
					1.9×10^9	2.0	0.7	peak 3	patch	3
					10^7-10^8	0.1-2.0	3-8	backgr. precip.	broad region of diffuse aurora	-
Mar. 9	end of expans. phase Dst=-12 K_p=2$^-$	74.8	64.3	10.5	3.9×10^9	4.5	.7	peak 1	not obs.	2
					1.4×10^9	34.3	15.5	peak 2	arc	1
					10^7-10^8	0.1-1.0	∿3	backgr. precip.	not vis. broad region of diffuse aurora	-
Mar. 7	recovery Dst=-50 K_p=5$^+$	73.5	58.0	15.5	2.5×10^9	2.0	1.4	peak 1	?	2
					9.4×10^8	20.7	3.8	peak 2	arc	2
					9.8×10^8	3.0	2.9	peak 3	arc	2
					2.8×10^8	0.8	1.8	peak 4	arc	2
					4.0×10^8	0.4	0.6	peak 5	arc	2
					5.3×10^9	1.9	2.3	peak 6	arc	3
					1.7×10^9	1.7	0.6	peak 7	not obs.	3
					1.4×10^9	6.8	1.6	peak 8	arc	3
					6.0×10^8	4.8	5.0	peak 9	arc	3
					∿10^8	∿1.0	3-8	backgr. precip.	diff. aurora	-

TABLE 10

A Summary of the Latitudinal Extent and Significant Features of the Electron Precipitation Observed by the Lockheed Instrumented Satellite.

the satellite as it moved from pole to equator. In the last column, note that there is a clear latitudinal distinction between the types 1 and 2 and type 3 spectral change with the type 3 spectral change equatorward of types 1 and 2 in all cases.

In the two passes which occurred prior to a substorm, the proton precipitation was observed to comprise a broad uniform peak almost 1 erg/(cm^2-sec-st) in total energy flux at the equatoward edge of the electron precipitation and to extend approximately 1° beyond the electron precipitation. In the three passes which occurred after a substorm, the protons were again observed to be uniform and spread throughout most of the electrons but not extending beyond the equatoward edge of the electron precipitation. Although the proton total energy flux was observed to be larger over most of the extent of the electron precipitation in the passes which occurred after a substorm, the total proton energy flux at the equatoward end of the electron precipitation was observed to be a factor of 10 less than in the two passes which occurred before a substorm.

SECTION 3.

3.1 Introduction

In this chapter, the data presented in Chapter 2 will be compared to the low-energy auroral zone particle precipitation data observed by Frank and Ackerson (1971). A substorm morphology will be outlined and a discussion of the particle morphology proposed by Winningham et al. (1975) will be given. Finally, diffuse aurora as observed by Lui and Anger will be discussed in terms of the particle observations presented in Chapter 2 and the established total particle energy flux threshold needed to produce visible auroral luminosity seen by an all-sky camera.

3.2 PRECIPITATION MORPHOLOGY

3.2.1 A comparison with Frank and Ackerson's Injun 5 data.

In their auroral zone particle precipitation survey, Frank and Ackerson (1971) used color-coded, energy-time spectrograms to effectively display the detector response for 117 electron energy band-passes between 50 ev and 50 kev. In most cases, the detector response can be assumed to be differential number flux intensity. In reference to late evening precipitation, their study showed that during periods of magnetic quiescence (K_p of 0 to 2), two or more distinct regions or bands of precipitation were observed across the auroral zone (see plates 1b, 2a, and 2b Frank and Ackerson, 1971). In these bands, the differential number flux over the whole energy spectrum increased but electrons of energy <300 ev contributed most to the total number flux. With increased magnetic activity (K_p of 3 to 4+), the bands became less well defined, and the band differential number flux became more intense for all energies. Often in these well-defined bands, the maximum differential number flux was observed to rise with time from low energies to higher

energies (∿1 kev) and then decrease back to lower energies thereby tracing out a red, arch-shaped substructure in the E-t spectrogram. Such arch-shaped substructures are called inverted 'V' events (see plates 1a and 3b Frank and Ackerson, 1971). The energy spectra associated with such precipitation would have to have exhibited at least an extremum in the differential number flux for energies around 1 kev in order that an arch-shaped structure be present in the E-t spectrogram. Such an extremum is evident in the sequence of spectra associated with plate 1a (Figure 2 their paper). Frank and Ackerson (1971) study also showed that occasionally, during magnetically disturbed periods, a relatively structureless broad precipitation region, extending several degrees in latitude, is observed equatorward of the inverted 'V' events. It is not uncommon for a weakly energetic red band (i.e., a band of intense low energy <1 kev precipitation) to be wedged into this broad structureless precipitation region.

To illustrate these morphological features described above and their effects on the total energy, number flux, and average energy of the precipitation, Frank and Ackerson (1971) compared an E-t spectrogram (their plate 5a) with its associated total number flux, total energy flux and average energy profiles (their Figure 9). The E-t spectrogram displayed simultaneously a band exhibiting an inverted 'V' substructure between 2333 and 2334 UT and a broad structureless precipitation region equatorward in which an intense but weakly energetic band is embedded between 2335 and 2336 UT. It should be pointed out that this inverted 'V' event is the most energetic ever observed by Frank and Ackerson, and due to the red color-coded threshold of the E-t spectrogram, the arch or

inverted 'V' pattern is not as evident as would have been for more typical inverted 'V' events. As shown in their Figure 9, this inverted 'V' event caused a marked increase in the total number flux, total energy flux as well as in the average energy. The band precipitation wedged in the structureless precipitation caused a substantial increase in the total number flux, but in response to a heavily weighted low energy (<1 kev) differential number flux, the total energy flux is increased only slightly while the average energy is decreased remarkably, a feature which we have seen in Chapter 2 to be a common occurrence in the broad background precipitation equatorward of the energetic peaks observed after the onset of an auroral substorm. It should not be assumed that all band precipitation region which do not exhibit the inverted 'V' substructure produce a decrease in the average energy profile. Band precipitation is usually a result of an increase in the differential number flux, over the entire energy range of the spectrum (50 ev to 50 kev). If the increase in the differential number flux were symmetric over the energy range of the spectrum, then the average energy would not increase, but this is not likely to happen. Rather the increase is asymmetric. If the asymmetry is weighted or favors the low energies particles (<2 kev), the average energy is likely to decrease in the band. If the asymmetry favors higher energies, the average energy will probably increase. The increase in the average energy associated with bands which do not exhibit an inverted 'V' substructure is not as great as that for bands which do exhibit an inverted 'V' substructure because differential number flux at the high end of the spectrum are not usually as intense as in bands exhibiting the inverted 'V' substructure.

It is now clear from the above discussion that the bands with and without the inverted 'V' substructure, the broad structureless equatorward precipitation and the weakly energetic bands embedded in the structureless precipitation are all typical features observed in precipitation data presented in Chapter 2. The energetic peaks which are particularly broader in latitudinal extent, of a higher average energy and shown to produce intense active auroral arcs are certainly bands exhibiting an inverted 'V' substructure. The remaining less energetic peaks such as the March 16 peaks 2 and 3 and the March 7 peak 2 which were shown to also produce auroral arcs which do not exhibit the inverted 'V' substructure. The broad background precipitation void of prominent peaks observed in the March 9 and 14 precipitation and shown to produce a broad region of visible diffuse aurora is synonymous with Frank and Ackerson's structureless precipitation. The March 14 peak shown to be at least associated with a discrete patch in the diffuse aurora is a good example of a weakly energetic band embedded in the structureless precipitation similar to the weakly energetic band shown in Frank and Ackerson's plate 5a. As a final comment the total number and energy flux and average energy observed in both the proton and electron profiles presented by Frank and Ackerson (1971) in their Figure 9 and the March 7, 9, and 14 profiles presented in Chapter 2 are comparable. Therefore, it has been shown that the precipitation data presented by Frank and Ackerson and in this study agree in magnitude and in all morphological aspects.

3.2.2 A Proposed Substorm Related Precipitation Morphology.

As previously mentioned, Frank and Ackerson observed that occasionally during magnetically disturbed periods ($K_p>3$), a broad structureless

precipitation occurred after the onset of a substorm and the passes which occurred before a substorm exhibit no such borad precipitation region. Thus, there is a need to relate precipitation morphology to substorm phase, and thereby further order a complex subject.

On the basis of the particle precipitation data presented in this study and by Frank and Ackerson (1971), the following outline is a proposed late evening auroral zone particle precipitation morphology:

I. BEFORE SUBSTORM

A. Electron Precipitation

1. Several prominent peaks on a background precipitation are evident in the total number and energy flux profiles.
2. Background precipitation confined to a relatively narrow 5° to 7° in latitudinal extent with well-defined boundaries.
3. Usually there exists at least one peak whose latitudinal extent, total energy flux, and average energy are larger than the accompanying peaks.
4. Prominent peaks are energetic enough to produce visible auroral arcs.
5. Background precipitation is not usually energetic enough to produce visible diffuse aurora except possible at the equatoward end where it is aided by the proton precipitation.

B. Proton Precipitation

1. Composed of a single broad peak whose center is located just at the equatoward edge of the electron precipitation.
2. Total energy flux of both the proton peak and the equatorward end of the background electron precipitation are comparable.

II. AFTER SUBSTORM

A. Electron Precipitation

1. Intense and energetic peaks usually on the poleward half of the background precipitation.
2. Background precipitation confined to a broad region 10° and 15° in latitudinal extent with well-defined boundaries.
3. Number and energy flux of peaks and background precipitation much greater than before substorm.
4. A considerable portion of the background precipitation equatorward of the energetic peaks is void of prominent peaks.
5. Usually there exists at least one peak whose latitudinal extent, total energy flux, and average energy is much greater than the other accompanying peaks.
6. Poleward energetic peaks produce active auroral arcs and a large portion of the background precipitation equatorward of the peaks produces visible diffuse aurora.

B. Proton Precipitation

1. Uniformly spread across most of the electron precipitation region.
2. About an order of magnitude less in total energy flux than the electron background precipitation.

3.2.3. Comments on the substorm-related electron precipitation morphology proposed by Winningham.

The substorm-dependent precipitation morphology just proposed differs significantly from the precipitation morphology Winingham

et al. (1975) interpreted from the 10 ev to 10 kev Isis particle data. Their morphology accounts for substorm phase and tries to incorporate the magnetospheric plasma sources of auroral electrons. In the local time sector between 21 and 03 MLT, they showed the simultaneous existence of two regions of precipitation, namely, the BPL and the equatoward CPL regions so named because of their connection with the boundary plasma layer (BPL) or region of the last closed field line and central plasma layer (CPL) as particle sources.

As a function of substorm time, the BPL and CPL regions behave very differently. The precipitation in the BPL region exhibits the most variations during a substorm. This is the precipitation region in which inverted 'V' events are found and whose precipitation when energized produces discrete auroras. During the substorm's expansive phase, there occurs a considerable increase in the total number flux and average energy of the BPL precipitation and a dramatic poleward motion of the front of the BPL region resulting in the expansion of that entire region. The poleward expansion of the BPL is presumably due to the successive reconnection of field lines in the tail. Some time during the expansion, there occurs a collapse of the BPL characterized by a decrease of the average energy and energy flux. The collapse begins in the middle of the BPL region and expands outwards. In the recovery phase this collapse becomes nonuniform, and together with the development of an extremely anistropic pitch angle distribution, destroys the spatial continuity of the BPL as depicted in their E-t spectrograms. The CPL region is always present even in the absence of discrete auroras. It is relatively stable during substorms; that is, there is no dramatic latitudinal change in the width and in the position of the equatorward

boundary. The average energy and total energy flux of the CPL precipitation increases during the expansive phase and as depicted on the E-t spectrogram, is isotropic, diffuse and "softens" with decreasing latitude. This region is associated with diffuse aurora and the structureless precipitation seen by Frank and Ackerson.

To illustrate the division of the auroral zone precipitation into the BPL and CPL regions, the five electron precipitation profiles presented in Chapter 2 are again displayed in Figure 35 (a-e). The BPL and CPL regions as described by Winningham et al. are indicated in these profiles. The collapse of the middle of the BPL after the onset of the poleward expansion is clearly evident in the March 14 profile. The collapse is not as obvious in the March 9 profile and does not exist in the March 7 profile. The CPL and BPL region before a substorm are clearly distinguishable. However, according to Winningham et al., after a substorm, the boundary between the BPL and CPL cannot be distinguished since there is no way of knowing with a polar orbiting satellite where the most equatorward auroral arc producing region of precipitation (peak) was just before the poleward expansion. Thus, in the March 7, 9, and 14 profiles of Figure 35 (c-e), the boundary between the two regions is indicated by a '?'. Before a substorm the precipitation is divided between the same two regions first suggested by Frank and Ackerson (1971), namely, a discrete precipitation region (BPL) poleward of a uniform or diffuse precipitation region (CPL). However, after a substorm, the discrete precipitation (BPL) by definition takes in a considerable portion of the Frank and Ackerson structureless precipitation. The poleward edge of the late evening auroral bulge is delineated by 1 or 2

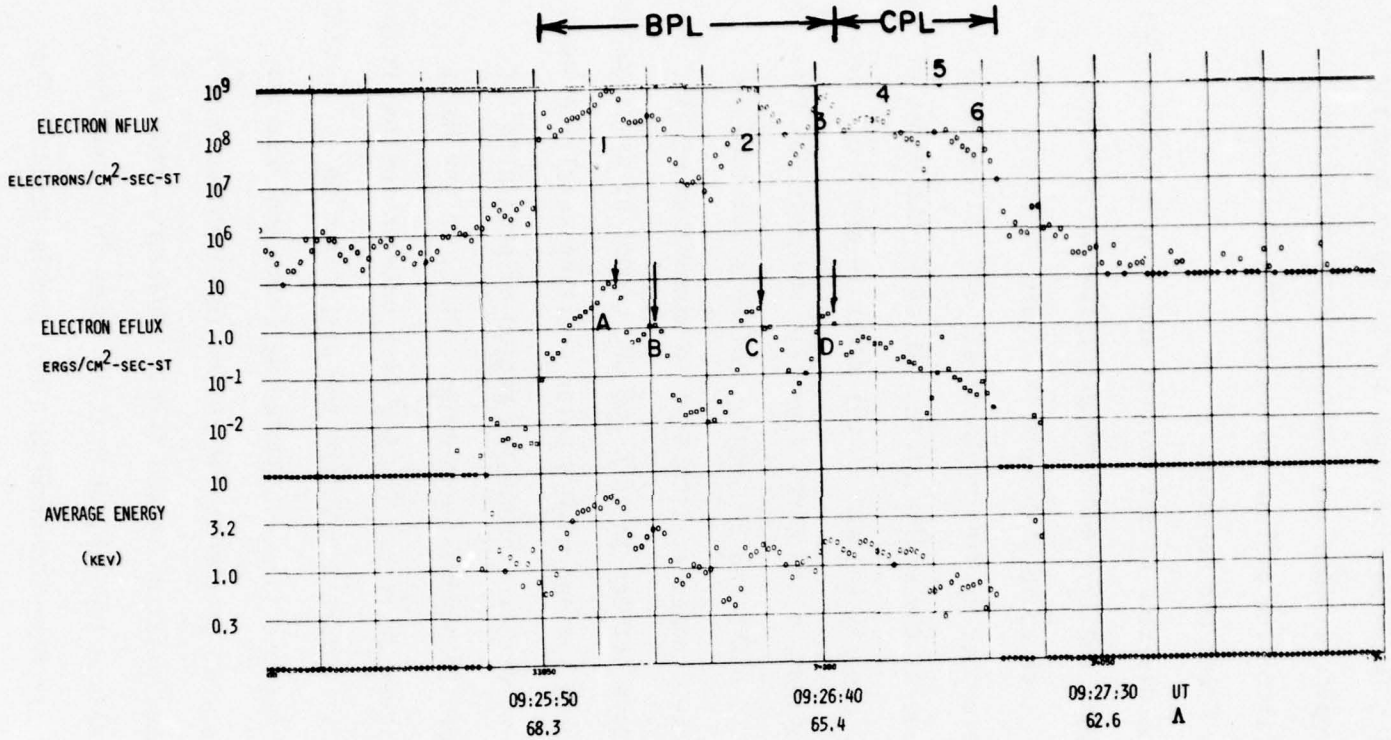

Figure 35a

March 16 electron precipitation profiles showing the CPL and BPL regions according to Winningham et al. (1975).

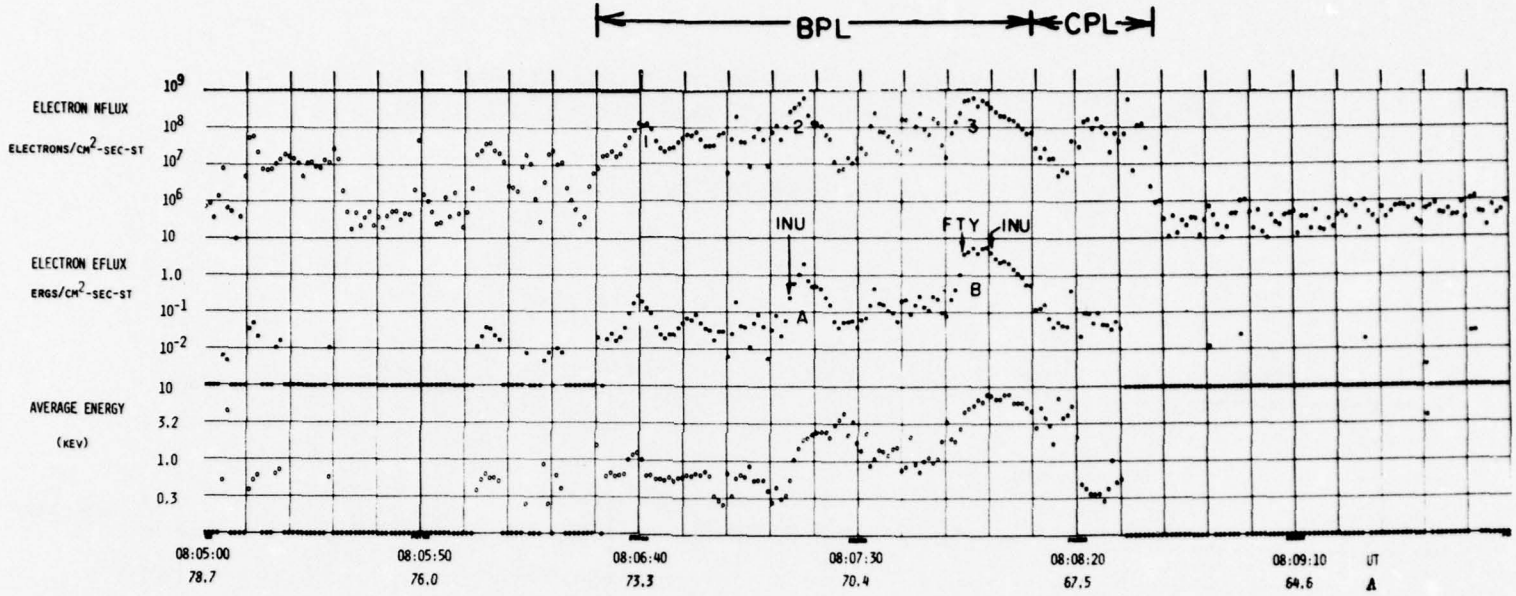

Figure 35b

April 7 electron precipitation profiles showing the CPL and BPL regions according to Winningham et al. (1975).

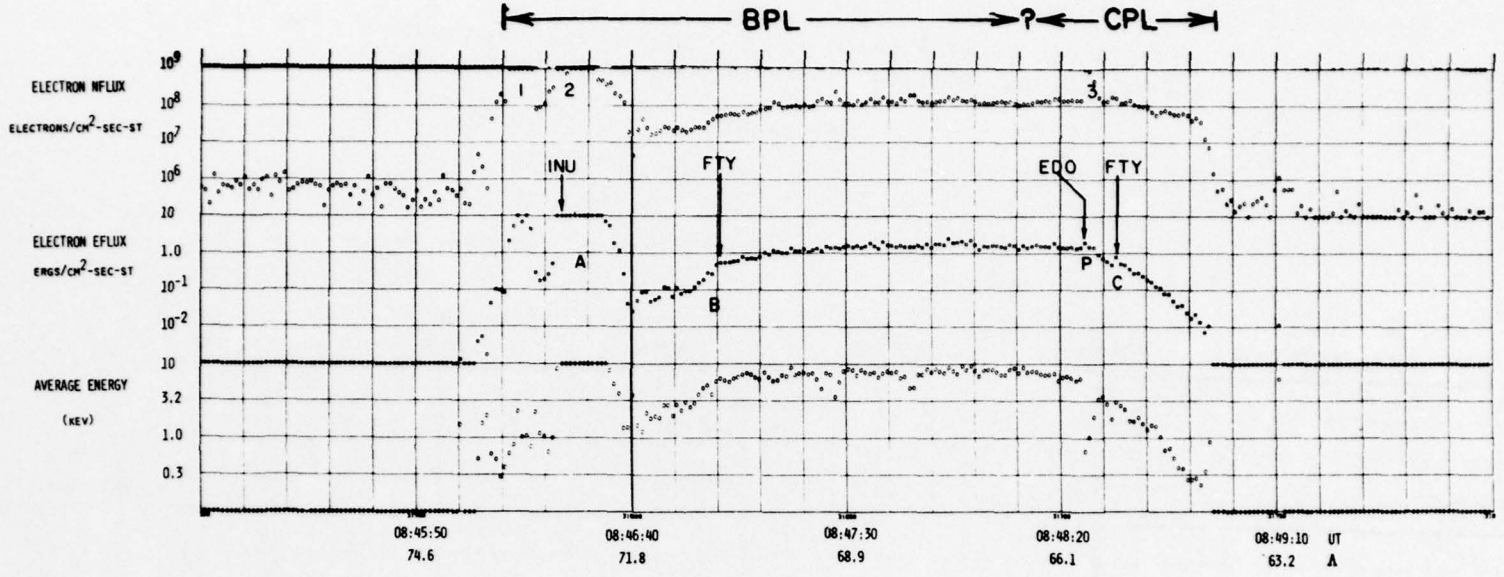

Figure 35c

March 14 electron precipitation profiles showing the CPL and BPL regions according to Winningham et al. (1975).

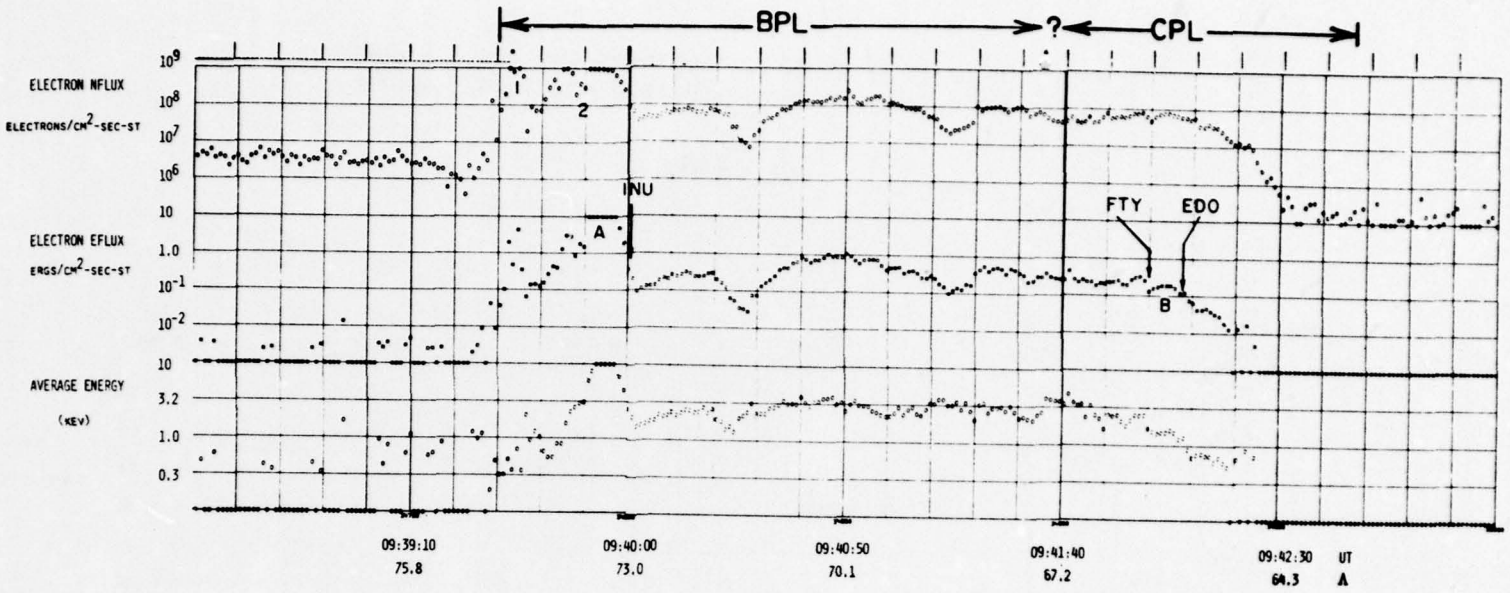

Figure 35d

March 9 electron precipitation profiles showing the CPL and BPL regions according to Winningham et al. (1975).

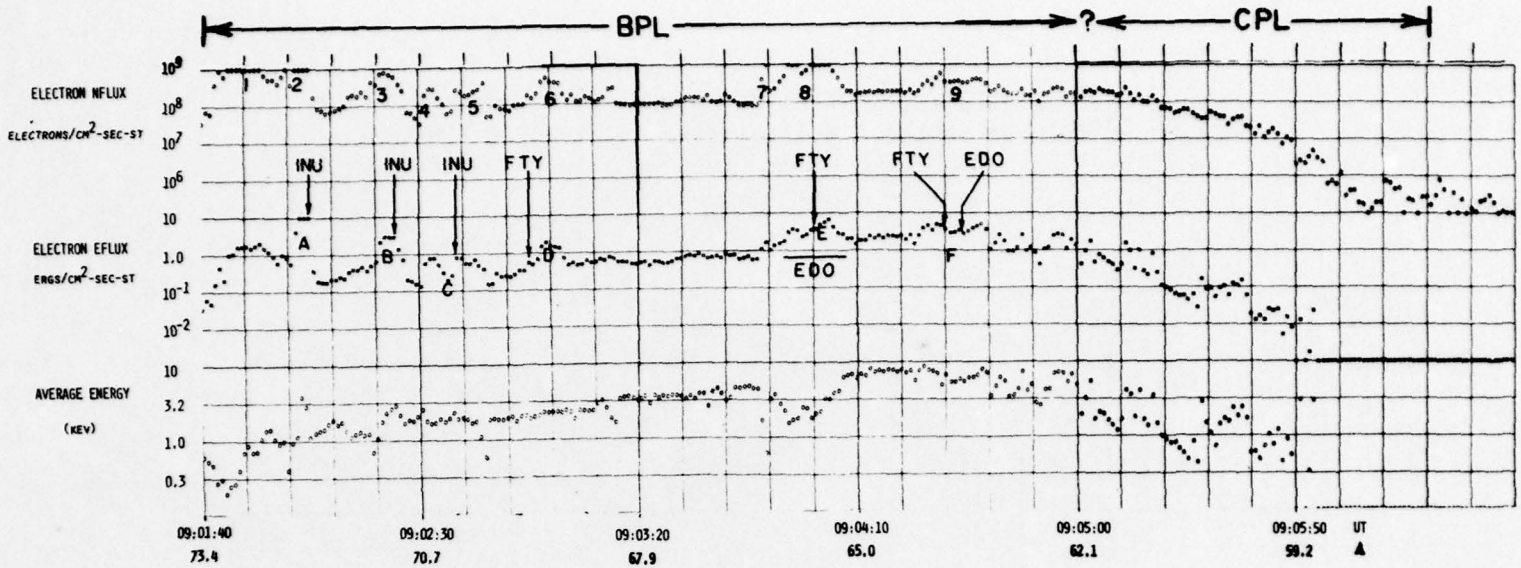

Figure 35e

March 7 electron precipitation profiles showing the CPL and BPL regions according to Winningham et al. (1975).

intense discrete arcs. The data presented in this study and by Frank and Ackerson support this observation, and it has been shown that these arcs are produced by intense energetic band precipitation often exhibiting inverted 'V' substructures. The bulge itself is filled with visible diffuse aurora in which are embedded discrete auroral forms such as arcs and patches. Such forms are usually present during the expansive phase of the auroral substorm. At least three embedded arcs were observed during the March 7 pass. They were shown to be spectrally very much different than the arcs delineating the poleward edge of the bulge and differing significantly from their background spectra only at the low end of the energy spectrum. For these reasons, it is suggested that during the expansive phase of an auroral substorm, the BPL region moves poleward but without increasing its latitudinal width. On the other hand, the CPL region fills in behind. Thus, it is the CPL region whose latitudinal extent increases during the expansive phase of an auroral substorm. As for the collapse in the BPL, this can be easily interpreted as the equatorward erosion of the poleward edge of the CPL. This erosion is consistent with auroral observations made after the March 14 pass (see section 2.4.2).

In conclusion, it is proposed that a third region in the electron precipitation called the "transient plasma layer" or TPL be included in the Winningham et al. precipitation morphology. This region corresponds to the region of the newly connected field lines in the tail. The TPL does not exist before a substorm and slowly contracts back to the CPL's poleward boundary after recovery and, for this reason, it is called the transient plasma layer. The TPL is indicated in Figure 36 (a-c) where

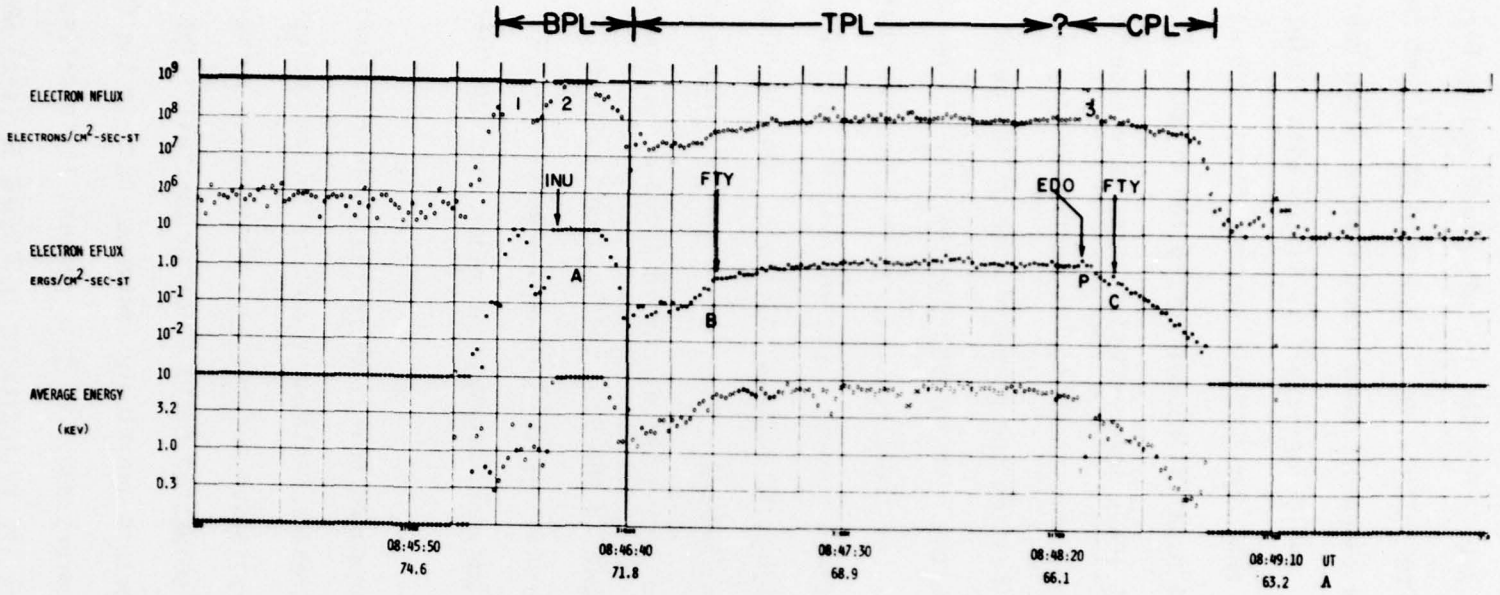

Figure 36a

March 14 electron precipitation profiles showing the TPL region proposed in the text.

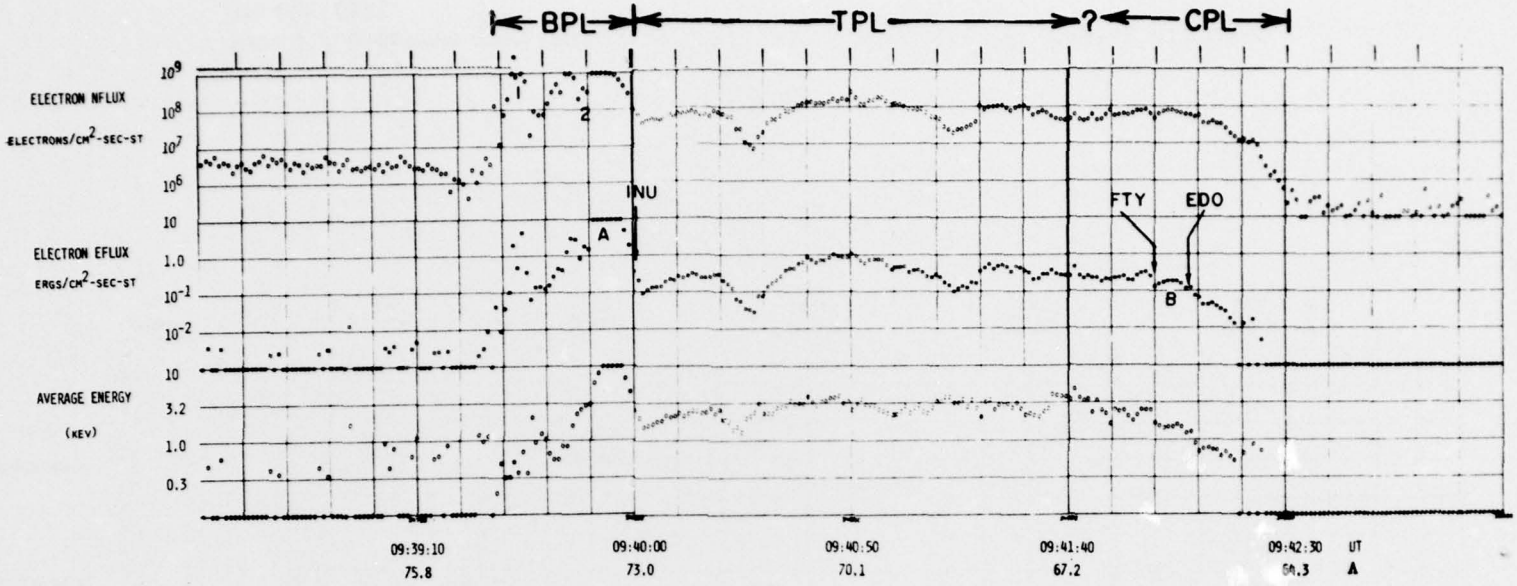

Figure 36b

March 9 electron precipitation profiles showing the TPL region proposed in the text.

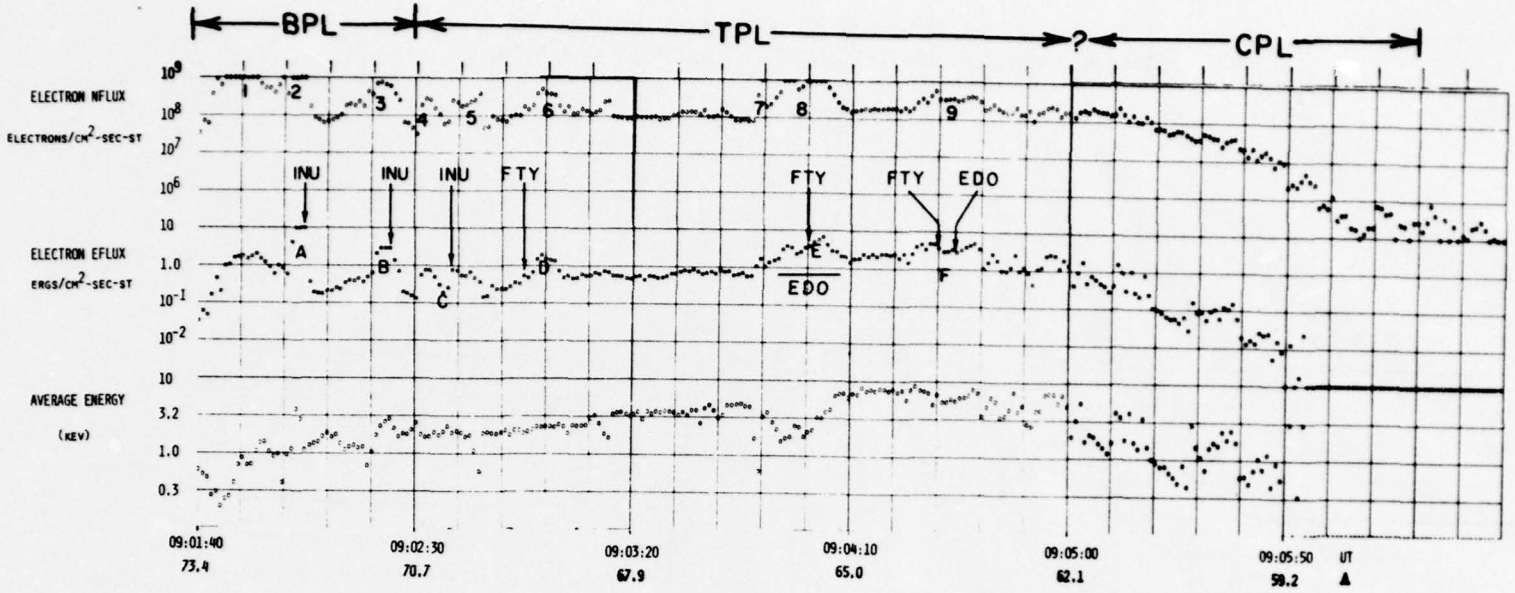

Figure 36c

March 7 electron precipitation profiles showing the TPL region proposed in the text.

the post breakup precipitation profiles are shown. Because there is no way of knowing prior to the onset of a substorm where the boundary between the BPL and CPL is located, the boundary between the TPL and CPL is not known and is indicated by a ? in Figure 36 (a-c). It is speculated that the TPL contains the weakly energetic peaks of spectral type 3 responsible for the production of patches and arcs in the diffuse aurora seen after breakup.

3.3 TOTAL ENERGY FLUX THRESHOLD

The total energy flux threshold can be determined by comparing just visible or threshold luminosity observed directly up the magnetic field lines with the total energy flux precipitating down the field lines. In practice this is virtually impossible to do because it requires a satellite to cross at least in the near vicinity of the magnetic zenith of an all-sky camera station with threshold auroral luminosity appearing in that region of the sky. None of the five passes to be presented conform to this strict requirement. However, the March 9 pass (Figure 29) occurred over just visible diffuse aurora whose intensity, when Van Rhijn, effects are accounted for, appears fairly uniform across the field of view of the Fort Yukon camera. The uniformity is also evident in the March 9 electron total energy flux profile in Figure 25. Because the luminosity is uniform across the field of view of the Fort Yukon all-sky camera, it is reasonable to assume that the total particle energy flux in the Fort Yukon magnetic zenith is similar to that which was observed along the satellite's trajectory at an invariant latitude equivalent to the Fort Yukon magnetic zenith. The L-shell extension of the Fort Yukon magnetic zenith to the satellite's trajectory is indicated on the energy flux profile in Figure 25. In the near vicinity of this

position, the total electron energy flux and average energy is approximately 0.25 ergs/(cm^2-sec-st) and 4 kev respectively, and the total proton energy flux is approximately 0.1 ergs/(cm^2-sec-st). These values are taken to be the same for the precipitation which produced the luminosity seen in the Fort Yukon magentic zenith.

According to Rees and Luckey's theoretical calculations (1974), an electron total energy flux of 0.25 ergs/(cm^2-sec-st) with an average energy of 4 kev (or equivalently a downward electron flux (assuming isotropy) of 0.78 ergs/cm^2-sec at an e-folding energy of 2 kev) would produce 140 rayleighs of 4278 N_2^+ emission. Romick (private communication) has experimentally shown that equal electron and proton total energy fluxes produce nearly equal amounts of 4278. He determined an emission rate per unit proton energy flux of about 150 Rayleighs of 4278/erg-cm^{-2}-sec^{-1} which is comparable to the 120-200 Rayleighs of 4278/erg-cm^{-2}-sec^{-1} theoretically determined for electrons by Rees and Luckey (1974). Thus, assuming isotropy, the 0.1 ergs/(cm^2-sec-st) of proton total energy flux observed at the satellite's trajectory on March 9 would produce an additional 45 Rayleighs of 4278. This together with the electron contribution gives a total of 180 Rayleighs of 4278 N_2^+ emission due to a particle total energy flux of 0.35 ergs/(cm^2-sec-st). From the Fort Yukon meridian scanning photometer data, 270 Rayleighs of 4278 (uncorrected for extinction, scattering and night sky background) was observed in the Fort Yukon mangetic zenith. Considering that the total particle flux in the Fort Yukon zenith and at the satellite's trajectory are not precisely the same, the experimentally observed and theoretically calculated 4278 intensities seem to agree. Also, about 2000 Rayleighs of 5577 were observed in the Fort Yukon zenith. This is about 2 times as

bright as in IBC-I aurora which is just below the minimum detectable threshold of the 35mm all-sky camera used in this study. Thus, the 0.35 ergs/ (cm^2-sec-st) or more conveniently 1 erg/(cm^2-sec) of downward total particle energy flux is a good rule of thumb total energy flux threshold for the production of the minimum luminosity detectable by the 35mm all-sky camera used along the Alaskan all-sky camera chain.

3.4 DIFFUSE AND DISCRETE AURORA

Using the Isis-2 photometric data, Lui and Anger (1973) observed an oval shaped belt of uniform auroral luminosity centered around the magnetic pole. They called this belt of luminosity the diffuse aurora and showed it persisted even under the most quiet magentic conditions. Also discrete auroral forms were usually seen within the diffuse aurora towards the poleward end of the belt. From these observations, it is proposed here that diffuse aurora be defined as a background luminosity in which are found discrete auroral forms defined as narrow (relative to the latitudinal extent of the diffuse auroral region) enhancements in the background luminosity. These working definitions of diffuse and discrete aurorae are consistant with the interpretation of the electron precipitation data given in Chapter 2; there, the electron precipitation was described as discrete peaks on a background precipitation, and the association of Lui and Anger's diffuse aurora belt with this background electron precipitation is readily made.

From a cursory examination of the Isis-2 particle data, Lui and Anger claimed that, in the midnight sector, the diffuse aurora corresponded to a region of electron and proton precipitation. The data presented in Chapter 2 certainly substantiates this claim, and further shows that the

total energy flux of the proton precipitation is comparable or considerably larger than some portions of the electron background precipitation usually towards the equatorward end. In the previous section, it was shown that the total luminosity produced by electron and proton precipitation of equal energy flux were comparable. Therefore, it can be concluded that towards the equatorward end of the diffuse aurora the proton precipitation is comparable if not the sole contributor to the total luminosity of the diffuse aurora. Over the regions where the electron precipitation is the major contributor to the diffuse luminosity, the proton contribution is small but still a factor which should be accounted for in any optical measurements even of some auroral arcs.

The background electron precipitation seems to exhibit the same physical characteristics that the diffuse aurora was shown to exhibit by Lui and Anger, namely, a sharp equatorward edge whose latitudinal position is independent of substorm time, contains discrete or sharply peaked precipitation, total energy flux increases after a substorm and the precipitation region is continuous over a wide range of latitudes and longitudes (Frank and Ackerson, 1972). Lui and Anger suggested that during magnetic quiet times, the diffuse auroral belt may define the auroral oval. In light of this suggestion and the above similarities, it is proposed that an electron precipitation oval be defined as the longitudinal and latitudinal extent of the background electron precipitation during all levels of magnetic activity. From the correlations made in Chapter 2, it is clear that the auroral oval is contained within the electron precipitation oval. Because the auroral oval has the additional dependence on the total particle energy flux, the extent

and dynamics of the precipitation oval is a better indicator of the extent and dynamics of the source region (presumably the plasma sheet). Therefore, the position and latitudinal extent of the electron precipitation oval should give a stronger correlation with Dst, B_Z etc. than that which is given by the auroral oval.

As a final comment, it was shown in Chapter 2 that after a substorm a large portion of the background electron precipitation equatorward of the energetic peaks produced a latitudinally broad region of visible diffuse aurora. Informally, this luminosity acquired the name "diffuse aurora" rather than the "visible portion of Lui and Anger's diffuse aurora." As a result, the idea of "diffuse aurora" equatorward of discrete aurora became a morphological fact. From the discussion given in this section and the particle and all-sky data correlated in Chapter 2, it is hoped that the morphological concept of discrete auroral forms in diffuse aurora even visible diffuse aurora be understood.

REFERENCES

Ackerson, K. L. and L. A. Frank, Correlated Satellite Measurements of Low-Energy Electron Precipitation and Ground-Based Observations of a Visible Auroral Arc, J. Geophys. Res., 77, 1128, 1972.

Bhattacharya, B. K., A Study of Auroral Motions from All-Sky Camera Records, Com. J. Phys., 38, 1279, 1960.

Frank, L. A., K. L. Ackerson, Local-Time Survey of Plasma at Low Altitudes over the Auroral Zones, J. Geophys. Res., 77, 4116, 1972.

Greenwald, R. A., W. L. Ecklund, and B. B. Balsley, Auroral Currents, Irregularities, and Luminosity, J. Geophys. Res. 78, 8193, 1973.

Johnson, R. G., J. B. Reagon, and R. D. Sharp, Satellite Experiments for D-Region Simulation studies of High-Altitude Nuclear Weapons Effects, Lockheed Missiles and Space Company, Final Technical Report, Control 3398(00), 1969.

Lui, A. T. Y. and C. D. Anger, A Uniform Belt of Diffuse Auroral Emission seen by the ISIS-2 Scanning Photometer, Planet. Space Sci., 21, 799, 1973.

Pazich, Philip M., Rocket-Based Measurements of Auroral Particle Fluxes associated with Field-Aligned Currents, Ph.D. dissertation, Rice Univ., Houston, 1972.

Rees, M. H. and D. Luckey, Auroral Electron Energy Derived from Ratio of Spectroscopic Emissions 1. Model Computations, J. Geophys. Res., 79, 5181, 1974.

Störmer, Carl, The Polar Aurora, Oxford University Press, Amer. House, London, 1955.

Winningham, J. D., S.-I. Akasofu, F. Yasuhara, and W. J. Heikkila, Simultaneous Observations of Auroras from the South Pole Station and of Precipitation Electrons by ISIS-1, J. Geophys. Res, 78, 6579, 1973.

Winningham, J. D., F. Yasuhara, S.-I. Akasofu, and W. J. Heikkila, the Latitudinal Morphology of 10 ev to 10 kev Electron Flux is during Magnetically Quiet and Disturbed Times in the 21-03 MLT Sector, in print J. Geophys. Res., 1975.

DNA Report Distribution List

Contract F19628-74-C-0188

Dr. Douglas Archer
Mission Research Corp
735 State Street
Santa Barbara, Calif 93101

Dr. Doran Baker
Dr. Kay Baker
Utah State University
Space Science Lab
Logan, Utah 84321

Dr. Murray Baron
Stanford Research Institute
333 Ravenswood Ave.
Menlo Park, Calif 94025

Dr. Darrel Strobel
Naval Research Laboratory
Washington, D.C. 20375

Dr. Neil Brown
University of Alaska
Fairbanks, Alaska 99701

Mr. Herb Mitchell
R&D Associates
1815 North Ft Myer Drive, Suite 1100
Arlington, Virginia 22209

Dr. Jack Carpenter
Dr. William Reidy
Visidyne Corp
19 Third Ave NW Industrial Park
Burlington, MA 01803

Dr. Irving Kofsky
Photometrics Inc.
Marrett Road
Lexington, MA 02173

Dr. Jack Kumer
Lockheed Palo Alto Res Lab
3251 Hanover Street
Palo Alto, Calif 94304

Dr. Roland Meyerott
27100 Elena Road
Los Altos Hills, Calif 94022

Dr. Charles Blank
LCDR Christopher Thomas
Defense Nuclear Agency
Attn: RAAE
Washington, DC 20305